DRAFT, Id: ms.tex,v 1.44 2005/10/17 19:59:32 mjuric Exp , compiled on Friday 3RD February, 2006 09:28
Preprint typeset using LaTeX style emulateapj v. 6/22/04

THE MILKY WAY TOMOGRAPHY WITH SDSS

Mario Jurić[1], Željko Ivezić[2], Alyson Brooks[2], Robert H. Lupton[1], David Schlegel[1], Douglas Finkbeiner[1], Nikhil Padmanabhan[3], Nicholas Bond[1], Constance M. Rockosi[2], Gillian R. Knapp[1], James E. Gunn[1], Takahiro Sumi[1], Donald Schneider[4], J.C. Barentine[5], Howard J. Brewington[5], J. Brinkmann[5], Masataka Fukugita[6], Michael Harvanek[5], S.J. Kleinman[5], Jurek Krzesinski[5,7], Dan Long[5], Eric H. Neilsen, Jr.[8], Atsuko Nitta[5], Stephanie A. Snedden[5], Donald G. York[9]

DRAFT, Id: ms.tex,v 1.44 2005/10/17 19:59:32 mjuric Exp , compiled on Friday 3rd February, 2006 09:28

ABSTRACT

Using the photometric parallax method, we estimate the distances to ∼48 million stars detected by the Sloan Digital Sky Survey (SDSS), and map their three-dimensional number density distribution in the Galaxy. The currently available data sample the distance range from 100 pc to 15 kpc and cover 6,500 deg^2 of sky, mostly at high galactic latitudes ($|b| > 25$). These stellar number density maps allow an investigation of the Galactic structure without any a priori assumptions about its components. The data show strong evidence for a Galaxy consisting of an oblate halo, disk components, and a number of localized overdensities. The number density distribution of stars in the Solar neighborhood ($D < 1.5$kpc) favors a model having a "thin" and a "thick" exponential disk, with scale heights and lengths of $H_1 \sim 280$pc and $L_1 \sim 2400$pc, and $H_2 \sim 1200$pc and $L_2 \sim 3500$pc, respectively, and local thick-to-thin disk normalization $\rho_{thick}(R_\odot)/\rho_{thin}(R_\odot) = 4\%$. Fits applied to the entire dataset are significantly more uncertain due to the presence of clumps and overdensities. The halo power law index is very poorly constrained, but we find an oblate halo with $c/a \sim 0.5$ to be strongly preferred. While roughly consistent with this simple model, the measured density distribution shows a number of statistically significant deviations from the model predictions. In addition to known features, such as the Monoceros stream, a remarkable density enhancement covering over a thousand square degrees of sky is detected towards the constellation of Virgo, at distances of ∼5-15 kpc. Compared to counts in a region symmetric with respect to the $l = 0$ line and with the same Galactic latitude, it is responsible for a factor of 2 number density excess, and may be a nearby tidal stream or a low-surface brightness dwarf galaxy merging with the Milky Way. The $u - g$ color distribution of these stars implies metallicities lower than those of the thick disk, and consistent with the halo metallicity distribution.

Subject headings:

1. INTRODUCTION

The formation of galaxies like the Milky Way was long thought to be a steady process that created smooth distributions of stars, with the standard view of the Milky Way's main components exemplified by models of Bahcall & Soneira (1980) and Gilmore, Wyse & Kuijken (1989), and described in detail by Majewski (1993). But for some time, starting with the pioneering work of Searle & Zinn (1978) and most recently with the data from modern large-scale sky surveys (such as the Sloan Digital Sky Survey (SDSS, York et al. 2000, see the next section), The Two Micron All Sky Survey (2MASS, Majewski et al. 2002), and QUEST (Vivas et al. 2001), to name but a few), evidence has been mounting for a more complicated picture of the Galaxy. Unlike the smooth models that involve simple components described by analytic expressions, new data argues for much more irregular substructure, such as the Sgr dwarf tidal stream in the halo (Ivezić et al. 2000, Yanny et al. 2000, Vivas et al. 2001, Majewski et al. 2002), and the Monoceros stream closer to the Galactic plane (Newberg et al. 2002, Rocha-Pinto et al. 2003).

A common feature to most recent studies of the Milky Way structure is selection of tracers for which reasonably accurate distance estimates are possible (e.g. RR Lyrae stars, A-type stars, M giants). However, these tracers represent only a tiny fraction of stars on the sky because the vast majority of faint ($V \lesssim 21 - 22$) stars are on the main sequence. While the distance to main sequence stars can be determined from a photometric parallax relation, the lack of large-area optical[10] surveys with sufficiently accurate photometry (see Section 2.2) has prevented an efficient use of this method to constrain the Milky Way structure. The largest Galactic structure oriented data set to date to use accurate optical CCD photometry (Siegel et al. 2002) covered only ∼ 15 deg^2 large area, with ∼ 10^5 stars. All of the above limitations (selection of tracers, small area and limited photometric accuracy) lead to a small number of observed stars,

[1] Princeton University Observatory, Princeton, NJ 08544
[2] University of Washington, Dept. of Astronomy, Box 351580, Seattle, WA 98195
[3] Princeton University, Dept. of Physics, Princeton, NJ 08544
[4] Department of Astronomy and Astrophysics, Pennsylvania State University, University Park, PA 16802
[5] Apache Point Observatory, P.O. Box 59, Sunspot, NM 88349, U.S.A.
[6] University of Tokyo, Institute for Cosmic Ray Research
[7] Mt. Suhora Observatory, Cracow Pedagogical University, ul. Podchorazych 2, 30-084 Cracow, Poland
[8] Fermi National Accelerator Laboratory, P.O. Box 500, Batavia, IL 60510, U.S.A.
[9] Department of Astronomy and Astrophysics, The University of Chicago, Chicago, IL 60037 USA

[10] For example, near-IR colors measured by the all-sky 2MASS survey are not well suited for this purpose, because they only probe the Rayleigh-Jeans tail of the stellar spectral energy distribution and thus are not very sensitive to the effective temperature.

making it impossible to directly measure stellar number density. Instead, to recover the Galactic density field, studies have ordinarily had to resort to model fitting, where the model was usually given by theoretical considerations (e.g., Spitzer 1942) or empirical comparison with external galaxies (e.g., Bahcall & Soneira 1980).

The large area covered by the SDSS, with accurate photometric measurements and faint flux limits ($r < 22$), allow for a novel approach to study of the Galaxy: using a photometric parallax relation appropriate for main sequence stars, it is possible to estimate distances for the large majority of observed stars, and thus directly map the Galactic stellar number density. Here we describe such a study based on ∼48 million stars detected by the SDSS in ~ 6500 deg^2 of sky. A particular advantage of this method is that the number density of stars as a function of position in the Galaxy can be measured without any model assumptions (e.g. luminosity function and functional forms that describe the density laws for disks and halo). Rather, the computed number density directly constrains the required Galaxy components and their properties.

We describe the SDSS data and photometric parallax relation used in this work, and the construction of the stellar number density maps in the following Section. Analysis of these maps is described in Section 3, and in Section 4 we discuss in detail a remarkably large overdensity of stars discovered in these maps. Our main results are discussed and summarized in Section 5.

2. DATA AND METHODOLOGY

In this Section we list the basic characteristics of the SDSS imaging survey, discuss the adopted photometric parallax relation used to estimate the distance to each star, and describe a method for determining three-dimensional number density distribution as a function of Galactic coordinates.

2.1. *The Basic Characteristics of the SDSS Imaging Survey*

The SDSS is a digital photometric and spectroscopic survey which will cover up to one quarter of the Celestial Sphere in the North Galactic cap, and produce a smaller area (~ 225 deg^2) but much deeper survey in the Southern Galactic hemisphere[11] (York et al. 2000, Stoughton et al. 2002, Abazajian et al. 2003, Gunn et al. 2005, Tucker et al. 2005). The flux densities of detected objects are measured almost simultaneously in five bands (u, g, r, i, and z) with effective wavelengths of 3540 Å, 4760 Å, 6280 Å, 7690 Å, and 9250 Å (Fukugita et al. 1996, Gunn et al. 1998, Smith et al. 2002, Hogg et al. 2002). The completeness of SDSS catalogs for point sources is ∼99.3% at the bright end ($r \sim 14$, where the SDSS CCDs saturate, (Ivezić et al. 2001), and drops to 95% at magnitudes[12] of 22.1, 22.4, 22.1, 21.2, and 20.3 in u, g, r, i and z, respectively. All magnitudes are given on the AB$_\nu$ system (Oke & Gunn 1983, for additional discussion regarding the SDSS photometric system see Fukugita et al. 1996, and Fan 1999). The final survey sky coverage of about 8,000 deg^2 will result in photometric measurements to the above detection limits for about 80 million stars and a similar number of galaxies. Astrometric positions are accurate to about 0.1 arcsec per coordinate for sources brighter than $r \sim 20.5^m$ (Pier et al. 2003), and the morphological information from the images allows robust point source-galaxy separation to $r \sim 21.5^m$ (Lupton et al. 2002). The SDSS photometric accuracy is 0.02 mag (root-mean-square, at the bright end), with well controlled tails of the error distribution (Ivezić et al. 2003a). The absolute zero point calibration of the SDSS photometry is accurate to within ~ 0.02 mag (Ivezić et al. 2004). A compendium of technical details about SDSS can be found in Stoughton et al. (2002), and on the SDSS web site (http://www.sdss.org).

2.2. *The Photometric Parallax Method*

SDSS is superior to previous optical sky surveys because of its high catalog completeness and accurate multi-band photometry to faint flux limits over a large sky area. The majority of stars detected by SDSS are main-sequence stars (∼98%, Finlator et al. 2000), which have a fairly well-defined color-luminosity relation[13]. Thus, accurate SDSS colors can be used to estimate luminosity, and hence, distance, for each individual star. While these estimates are incorrect for a small fraction of stars such as multiple systems and non-main sequence stars, the overall contamination is small.

There are a number of proposed photometric parallax relations in the literature. They differ in the methodology used to derive them (e.g. geometric parallax measurements, fits to globular cluster color-magnitude sequences), photometric systems, and the absolute magnitude and metallicity range for which they are applicable. Not all of them are mutually consistent, and all exhibit significant intrinsic scatters of order a half a magnitude or more.

In Fig. 1 we compare several recent photometric parallax relations found in the literature. They are all based on geometric parallax measurements, but the stellar colors are measured in different photometric systems. In order to facilitate comparison, we use photometric transformations from Fukugita et al. (1996) and fits to the stellar locus in SDSS color-color diagrams (Ivezić et al. 2004). As evident, different photometric parallax relations are discrepant at the level of several tenths to a magnitude. Furthermore, the relation proposed by Williams et al. (2002) is a piece-wise fit to restricted color ranges, and results in a discontinuous relation. An analysis of Kurucz model atmospheres suggests that these discontinuities are probably unphysical (Ivezić et al., in prep).

We constructed a fit that attempts to reconcile the differences between these relations. We require a low-order polynomial fit that is roughly consistent with the two relations at the red end, and properly reproduces the SDSS observations of the position of the turn-off ($M_r = 5$ at $r-i = 0.10$) for globular cluster M13 (using a distance

[11] See also http://www.astro.princeton.edu/PBOOK/welcome.htm

[12] These values are determined by comparing multiple scans of the same area obtained during the commissioning year. Typical seeing in these observations was 1.5±0.1 arcsec.

[13] The uniqueness of color-luminosity relation breaks down for stars at main sequence turn-off ($r - i \sim 0.11$ mag for disk, and $r - i \sim 0.06$ for halo stars, Chen et al. 2001). Those are outside of all but the bluest bin of the $r - i$ range studied here.

of 7.1 kpc, Harris 1996). The adopted relation

$$M_r = 4.0 + 11.86\,(r-i) - 10.74\,(r-i)^2 + 5.99\,(r-i)^3 - 1.20\,(r-i)^4 \quad (1)$$

is similar to the Williams et al., Hawley et al. and West et al. relations at the red end, and agrees well with the Siegel et al. relation at the blue end.

This relation is quite steep, for example, $\Delta M_r/\Delta(r-i) \sim 10$ mag/mag at the blue end ($r-i \sim 0.1$). Because of this steepness, very accurate photometry (0.01-0.02 mag) is required to reach the intrinsic accuracy of the photometric relation (about 0.3 mag). Older photographic surveys have photometric errors of $\sim$ 0.1-0.2 mag (Sesar et al. 2005), which result in M_r errors exceeding $\sim$1mag. Hence, with the SDSS, the intrinsic accuracy of the photometric parallax method can be approached to a faint flux limit (implying a large number of stars) and over a large sky area for the first time.

2.2.1. *A Test of the Photometric Parallax Relation with Resolved Binary Stars*

The number of close stellar pairs in the SDSS survey with distances in the range 2-4 arcsec shows an excess relative to the extrapolation from larger distances (Sumi et al., in prep). Statistically, $\sim$70% of these pairs are physically associated binary systems. Since they typically have different $r-i$ colors, they also have different absolute magnitudes. The difference in absolute magnitudes, ΔM, can be computed from the adopted photometric parallax relation without the knowledge of the system's distance, and should agree with the measured difference of their apparent magnitudes, Δm. The distribution of the difference, $\delta = \Delta m - \Delta M$ should be centered on zero and should not be correlated with color if the shape of photometric parallax relation is correct (the overall normalization is not constrained, but this is not an important issue since the relation can be anchored at the red end using nearby stars with geometric parallaxes). The width of the δ distribution provides an upper limit for the intrinsic error of the photometric parallax method.

We have performed a preliminary test using a sample of 87 probable binaries from a 60 deg^2 large high Galactic latitude ($b = 52$ deg) field with $15 < i < 18$, as described in detail by Sumi et al. The median value of δ is -0.11, with comparable values for medians computed in 0.2 mag wide $r-i$ bins. This result places an upper limit on the systematic errors as a function of color in the adopted relation to $\sim$ 0.1 mag. The root-mean-square width of δ distribution without accounting for likely interlopers is 0.4 mag. This implies a distance error of 20%. The distribution is more centrally peaked than a Gaussian, which indicates that the intrinsic magnitude scatter of the photometric parallax method is probably smaller.

2.2.2. *The Pitfalls of the Photometric Parallax Method*

The photometric parallax method is not without pitfalls, even when applied to the SDSS data. Traditionally, the application of this method was prone to significant errors due to sample contamination by evolved stars (subgiants and giants, hereafter giants for simplicity), and their underestimated distances. This effect is also present in this study, but at a much less significant level because of the faint magnitudes probed by SDSS. At these flux levels, the distances corresponding to giants are large and sometimes even beyond the edge of the Galaxy (up to $\sim$100 kpc). The stellar density at these distances is significantly smaller than at distances corresponding to main sequence stars with the same apparent magnitude, and thus the contamination becomes fairly insignificant.

A quantitative illustration of this effect is shown in Fig. 2 for a fiducial Galaxy model. The worst case scenario corresponds to G giants with $g-r \sim 0.4$ and $r-i \sim 0.15$, and their most probable fraction is about 5%. This color range and the fraction of giants was determined using the SDSS data for the globular cluster M13 (the data for the globular cluster Pal 5 imply similar behavior). To be conservative, we have also tested a model with a twice as large fraction of giants. This analysis (see bottom panel) shows that the effect of misidentifying giants as main sequence stars is an overall bias in estimated number density of $\sim$4% ($\sim$8 % when the fraction of giants is 10%), with little dependence on distance from the Galactic plane beyond 500 pc. This is the distance range probed by stars this blue, and thus the worst effect of contamination by giants is a small overall overestimate of the density normalization. Shorter distances are probed by redder stars, M dwarfs, for which the contamination by M giants is negligible because the giant – main sequence luminosity difference is exceedingly large (e.g. there are tens of millions of M dwarfs in our sample, while the 2MASS survey revealed only a few thousand M giants in the same sky region, Majewski et al. 2003). Hence, the misidentified giants are not expected to significantly affect our analysis. This is in agreement with conclusions of a more detailed analysis by Siegel et al. (2002). Since this effect is fairly small, we do not explicitly correct for it.

Another source of systematic errors is the dependence of photometric parallax relation on metallicity. For example, Siegel et al. (2002) address this problem by adopting different relations for low- and high-metallicity stars (cf. Fig. 1). Since the SDSS photometry is not sufficient to reliably estimate metallicity for all the stars considered here, we adopted a single relation. However, the adopted relation does account for metallicity effects to some extent. The distant ($\sim$10 kpc) stars, with presumably low metallicities, are blue and for them the adopted relation is fit to the low-metallicity globular cluster M13. Thus, in some loose "mean" sense, the adopted relation smoothly varies from a relation appropriate for nearby, red, high-metallicity stars to a relation appropriate for more distant, blue, low-metallicity stars[14]. To further control the metallicity (and other systematic) effects, we perform analysis in narrow color bins, as described in more detail below.

Binarity may also play a significant role by systematically making unresolved binary stars, when misidentified as a single star, appear closer then they truly are. As discussed in detail by Siegel et al. (2002), the effect of binarity on derived distance scales, such as scale

[14] When the adopted photometric parallax relation is applied to the Sun ($r-i = 0.10$), the resulting absolute magnitude is too faint by about 0.5 mag. This is an expected result, because the relation is anchored to a low-metallicity globular cluster at the blue end.

height and scale length, is to underestimate them by up to ∼20%. They also show that the value of this bias is only weakly dependent on the actual composition of the binaries (e.g. their color difference and luminosity ratio), but it is dependent on the fraction of binaries in the Galaxy. Since this fraction is not well constrained, we do not take this correction explicitly into account, and thus *distance scales discussed in this work are effectively lower limits*. Note that this uncertainty cannot affect the shapes of various density features discussed below, unless the properties of binary stars vary greatly with the position in the Galaxy.

Perhaps more of a disadvantage, rather than a pitfall, is the inability of this method, when applied to main sequence stars, to probe distances as large as those probed by RR Lyrae and M giants (15 kpc vs. 100 kpc). However, a significant advantage of using main sequence stars is the vastly larger number of stars (the number ratio of main sequence to RR Lyrae stars in the SDSS sample is ∼10,000, and even larger for M giants, Ivezić et al. 2003bc, 2005). This large number of stars allows us to study their number density distribution with a high spatial resolution, and without being limited by Poisson noise.

2.3. *Determination of the Stellar Number Density*

In this Section we describe the stellar sample utilized in this work, and the methods used to construct three-dimensional number density maps.

2.3.1. *The SDSS stellar sample*

We utilize observations from 248 SDSS imaging runs obtained in a 5 year period through September 2003, which cover $6,538$ deg^2 of the sky. This is a superset of imaging runs described in SDSS Data Release 3 (Abazajian et al. 2003), complemented by a number of runs from SDSS Data Release 4 (Adelman et al. 2006) and the so called "Orion" runs (Finkbeiner et al. 2004). The sky coverage of these 248 runs is shown in figure 3. They cover 5450 deg^2 in the northern Galactic hemisphere, and 1088 deg^2 in the south.

We start the sample selection with 122 million observations classified as point sources (stars) by the SDSS photometric pipeline, *Photo* (Lupton et al. 2002, Lupton et al. 2005). For a star to be included in the starting sample, we require that $r < 22$, and that it is also detected (above 5σ) in at least the g or i band. The latter requirement is necessary to be able to compute either the $g - r$ or $r - i$ color. The two requirements reduce the sample to 87 million observations. For each magnitude measurement, *Photo* also provides a fairly reliable estimate of its accuracy (Ivezić et al. 2003a), hereafter σ_g, σ_r and σ_i. We correct all measurements for the interstellar dust extinction using the Schlegel, Finkbeiner & Davis (1998, SFD) maps.

2.3.2. *The Effects of Errors in Interstellar Extinction Corrections*

The SFD maps are believed to be correct within 10%, or better. This uncertainty plays only a minor role in this work because the interstellar extinction is fairly small at the high galactic latitudes analyzed here ($|b| > 25$): the median value of the extinction in the r band, A_r, is 0.08, with 95% of the sample with $A_r < 0.23$ and 99% of the sample with $A_r < 0.38$. Thus, only about 5% of stars could have extinction correction uncertain by more than the photometric accuracy of SDSS data (∼0.02 mag). The SFD maps do not provide the wavelength dependence of the interstellar correction, only its magnitude. The extinction corrections in the five SDSS photometric bands are computed from the SFD maps using conversion coefficients derived from an $R_V = 3.1$ dust model. Analysis of the position of the stellar locus in the SDSS color-color diagrams suggests that these coefficients are satisfactory at the level of accuracy and galactic latitudes considered here (Ivezić et al. 2004).

We apply full SFD extinction correction to all stars in the sample. This is inappropriate for the nearest stars because they are not beyond all the dust. Distances to the nearest stars in our sample, those with $r - i = 1.5$ (the red limit) and $r \sim 14$ (approximately the SDSS r band saturation limit), are ∼30 pc (distance determination is described in the next two sections). Even when these stars are observed at high galactic latitudes, it is likely that they are overcorrected for the effects of interstellar extinction. To estimate at what distances this effect becomes important, we have examined the dependence of the $g - r$ color on apparent magnitude for red stars, selected by the condition $r - i > 0.9$, in the region defined by $210 < l < 240$ and $25 < b < 30$. The distribution of the intrinsic $g - r$ color for these stars is practically independent of their $r - i$ color, with a median of 1.40 and a standard deviation of only 0.06 mag (Ivezić et al. 2004). This independence allows us to test at what magnitude (i.e. distance) the applied SFD extinction corrections become an overestimate because, in such a case, they result in $g-r$ colors that are bluer than the expected value of ~ 1.40. We find that for $r > 15$ the median $g - r$ color is nearly constant – it varies by less than 0.02 mag over the $15 < r < 20$ range. On the other hand, for stars with $r < 15$ the median $g - r$ color becomes much bluer – at $r = 14.5$ the median value is 1.35. This demonstrates that stars at $r > 15$ are already behind most of the dust column. With the median $r - i$ color of 1.17, the implied distance corresponding to $r = 15$ is ∼80 pc. For the probed galactic latitude range, this indicates that practically all the dust is confined to a region within ∼70 pc from the galactic midplane (here we define midplane as a plane parallel to the galactic plane that has Z=-25 pc, because the Sun is offset from the midplane towards the NGP by ∼25 pc; for more details see below). We arrive to the same conclusion about the dust distribution when using an analogous sample in the south galactic plane with $|b| \sim 12$ (in this case the median $g - r$ color is systematically bluer for $r < 19$, due to different projection effects and the Sun's offset from the midplane). Hence, in order to avoid the effects of overestimated interstellar extinction correction for the nearest stars, we exclude stars that are within 100 pc from the galactic plane when fitting galaxy models (described below). Only 0.05% of stars in the sample are at such distances. In summary, the effects of overestimated interstellar extinction correction, just as the effects of sample contamination by giants, are not very important due to the faint magnitude range probed by SDSS.

2.3.3. *The Treatment of Repeated Observations*

SDSS imaging data are obtained by tracking the sky in six parallel scanlines, each 13.5 arcmin wide. The six scanlines from two runs are then interleaved to make a filled stripe. Because of the scan overlaps, and because of the convergence of the scans near the survey poles, about 40% of the northern survey is surveyed at least twice. Additionally, the southern survey areas will be observed dozens of times to search for variable objects and, by stacking the frames, to push the flux limit deeper. For these reasons, a significant fraction of measurements are repeated observations of the same stars.

We positionally identify observations as corresponding to the same object if they are within 1 arcsec of each other (the median SDSS seeing in the r band is 1.4 arcsec). Out of the initial ∼122 million observations, the magnitude cuts and positional matching produce a catalog of 47.7 million unique stars (the "star catalog", table 1). There are two or more observations for about 36% (17.2 million) of these stars. For stars with multiple observations we take the catalog magnitude of the star to be equal to the weighted mean of all observations. In this step there is a tacit assumption that the variability is not important, justified by the main-sequence nature of the stellar sample under consideration (for a preliminary variability analysis of the SDSS stellar sample see Ivezić et al. 2003a).

As discussed in Section 2.2, an accurate determination of stellar distances by photometric parallax hinges on a good estimate of the stellar color and magnitude. In the bottom panel of Fig. 4 we show the mean r magnitude error of stars in the catalog as a function of the r band magnitude. The photometric errors are ∼0.02 mag for bright objects (limited by errors in modeling the point spread function), and steadily increase towards the faint end due to the photon noise. At the adopted sample limit, $r = 22$, the r band photometric errors are ∼0.15 mag. The g and i band magnitude errors display similar behavior as for the r band.

2.3.4. *Maximum Likelihood Estimates of True Stellar Colors*

The photometric parallax relation (eq. 2) requires only the knowledge of $r-i$ color to estimate the absolute magnitude. The accuracy of this estimate deteriorates at the faint end due to increased $r-i$ measurement error. It also suffers for blue stars ($r-i<0.2$) of all magnitudes because the slope of the photometric parallax relation, $\Delta M_r/\Delta(r-i)$, is quite large at the blue end – for these stars it would be better to use the $g-r$ (or $u-g$) color to parametrize the photometric parallax relation. On the other hand, the $g-r$ color is constant for stars later than ∼M0 ($g-r\sim 1.4$), and cannot be used for this purpose. These problems can be alleviated to some extent by utilizing the fact that colors of main sequence stars form a very narrow, nearly one-dimensional locus.

The $r-i$ vs. $g-r$ color-color diagram of stars used in this work is shown in Fig. 5. We find that the stellar locus is well described by the following relation:

$$g-r = 1.39(1-\exp[-4.9(r-i)^3 \quad (2)$$
$$-2.45(r-i)^2 - 1.68(r-i) - 0.050])$$

which is shown by the solid line in the figure.

The intrinsic width of the stellar locus is 0.02 mag for blue stars and 0.06 mag for red stars (Ivezić et al. 2004), which is significantly smaller than the measurement error at the faint end. To a very good approximation, any deviation of observed colors from the locus can be attributed to photometric errors. We use this assumption to improve estimates of true stellar colors and apparent magnitudes.

As illustrated in Fig. 5, for each point and a given error probability ellipse, we find a point on the locus with the highest probability[15], and adopt the corresponding $(g-r)_e$ and $(r-i)_e$ colors. Note that the error ellipse is not aligned with the $g-r$ and $r-i$ axes because the $g-r$ and $r-i$ errors are correlated ($\mathrm{cov}(g-r, r-i) = \mathrm{cov}(g,r) + \mathrm{cov}(g,-i) + \mathrm{cov}(-r,r) + \mathrm{cov}(-r,-i) = -\mathrm{cov}(r,r) = -\sigma_r^2$)

We exclude all points further than 0.3 mag from the locus, as such large deviations are inconsistent with measurement errors, and in most cases indicate a source that is not a main-sequence star. This requirement effectively removes hot white dwarfs (Kleinman et al. 2004), low-redshift quasars ($z < 2.2$, Richards et al. 2001), and white dwarf/red dwarf unresolved binaries (Smolčić et al. 2004). The sample stars span the MK spectral range from ∼F9 to M3 (Table 2).

Using the maximum likelihood colors, we estimate the magnitudes (g_e, r_e, i_e) by minimizing:

$$\chi^2 = \frac{(r-r_e)^2}{\sigma_r^2} + \frac{(g-g_e)^2}{\sigma_g^2} + \frac{(i-i_e)^2}{\sigma_i^2}, \quad (3)$$

which results in

$$r_e = \frac{w_r r + w_g(g-(g-r)_e) + w_i(i+(r-i)_e)}{w_r + w_g + w_i} \quad (4)$$
$$g_e = (g-r)_e + r_e \quad (5)$$
$$i_e = (r-i)_e - r_e \quad (6)$$

where $w_j = 1/\sigma_j^2$ for $j = g, r, i$.

The adopted $(r-i)_e$ color and r_e magnitude uniquely determine (through eq. 2) the absolute magnitude M_r for each star in the catalog. We dub this procedure a "locus projection" method, and refer to the derived colors as "locus-projected colors". In all subsequent calculations we use these "locus-projected" colors, unless explicitly stated otherwise. This method not only improves the color estimates at the faint end, but also helps with debiasing the estimate of density normalization. We further discuss this and other aspects of the locus projection in Appendix A.

2.3.5. *The Distance Estimates*

Given the photometric parallax relation (eq.2), the locus-projected maximum likelihood r band magnitude, and $r-i$ color, it is straightforward to determine the distance D to each star in the catalog using

$$D = 10^{0.2(r-M_r)}\ 10\ \mathrm{pc}, \quad (7)$$

[15] This is effectively a Bayesian maximum likelihood (ML) procedure with the assumption of a uniform prior along the one-dimensional locus. As seen from from Fig 5, the real prior is not uniform. We have tested the effects of non-uniform priors. Adopting an observationally determined (from Fig 5) non-uniform prior would change the locii of posterior maxima by only ∼ 0.005 mag (worst case), while further complicating the ML procedure, which is why we retain the assumption of uniform prior.

Depending on color, for the magnitude range probed by SDSS (r=14–22) the distance varies from ∼100 pc to ∼15 kpc.

Due to photometric errors in color, magnitude, and the intrinsic scatter of the photometric paralax relation, the distance estimate has an uncertainty, σ_D, given by:

$$\sigma^2_{M_r} = (\frac{\partial M_r}{\partial(r-i)})^2\sigma^2_{r-i} + \sigma^2_{M_{r,i}} \quad (8)$$

$$\sigma^2_D = (\frac{\partial D}{\partial M_r})^2\sigma^2_{M_r} + (\frac{\partial D}{\partial r})^2\sigma^2_r \quad (9)$$

where $\sigma_{M_{r,i}}$ is the intrinsic scatter in the photometric parallax relation. With an assumption of $\sigma^2_{r-i} \approx 2\sigma^2_r$, this reduces to a simpler form:

$$\frac{\sigma_D}{D} = 0.46\sqrt{(1 + 2\,(\frac{\partial M_r}{\partial(r-i)})^2)\sigma^2_r + \sigma^2_{M_{r,i}}} \quad (10)$$

The fractional distance error, σ_D/D, is a function of color, apparent magnitude and magnitude error (which itself is a function of apparent magnitude). In the top panel in figure 4 we show the expected σ_D/D as a function of r and $r-i$ with an assumed intrinsic photometric relation scatter of $\sigma_{M_{r,i}} = 0.3$ mag. This figure is a handy reference for estimating the distance accuracy at any location in the density maps we shall introduce in Section 2.4. For example, a star with $r-i = 0.5$ and $r = 20$ (or, using eq. 2, at a distance of $D = 2.5$ kpc) has a ∼18% distance uncertainty. Equivalently, when the stars are binned to three-dimensional grids to produce density maps (Section 2.4), this uncertainty gives rise to a nearly Gaussian radial "smearing function" with color and distance dependent variance σ_D.

To summarize, due to measurement errors, and errors in the adopted photometric parallax relation, the derived density maps, described below, will be different from the true stellar distribution. First, the spatial resolution is smeared due to just described random distance errors. Second, the distance scale has systematic errors, probably color and metallicity dependent, that "stretch or shrink" the density maps. In addition, for a small fraction of stars, the distance estimates may be grossly incorrect due to contamination by giants and multiple unresolved systems. Thus, all quantitative results, such as best-fit model parameters, should not be trusted to better than 10-20%. Nevertheless, these errors are sufficiently small that the maps fidelity is fairly well preserved, and they are a powerful tool for studying the Milky Way's stellar number density distribution.

2.4. *The Construction of the Density Maps*

The distance, estimated as described above, and the Galactic longitude and latitude, (l, b), fully determine the three-dimensional coordinates of each star in the sample. We first divide our star catalog into 19 bins in $r-i$ color[16]:

$$ri_0 < r-i < ri_1 \quad (11)$$

Typically, the width of the color bins $\Delta_{ri} \equiv ri_1 - ri_0$ is $\Delta_{ri} = 0.1$ for bins redder than $r-i = 0.7$ and $\Delta_{ri} = 0.05$ otherwise. ri_0 and ri_1 for each color bin are given in the second column of table 2. This is roughly equivalent to a selection by MK spectral type (Covey et al. 2005). The range of spectral types corresponding to each $r-i$ bin is given in SpT column of table 2.

The analysis of individual narrow color bins, as opposed to the whole sample, allows a better control of various systematic errors and selection effects. In particular, for each color bin we calculate the minimum and maximum observable distance, D_{min} and D_{max}, which define a volume limited sample,

$$D_{min} = 10^{0.2(r_{min}-M_r)}\,10 \text{ pc}, \quad (12)$$

$$D_{max} = 10^{0.2(r_{max}-M_r)}\,10 \text{ pc}, \quad (13)$$

Here $r_{min} = 15$ and $r_{max} = 21.5$ are adopted as bright and faint magnitude limits (SDSS detectors saturate at $r \sim 14$). Note that for each color bin D_{max}/D_{min} ∼20, and for the full sample D_{max}/D_{min} ∼150.

We define the "Cartesian Galactocentric coordinate system" by the following set of coordinate transformations:

$$x = R_\odot - D\cos(l)\cos(b) \quad (14)$$

$$y = -D\sin(l)\cos(b) \quad (15)$$

$$z = D\sin(b) \quad (16)$$

where $R_\odot = 8$ kpc is the adopted distance to the Galactic center (Reid 1993).

The choice of the coordinate system is motivated by the expectation of cylindrical symmetry around the axis of Galactic rotation $\hat{z}$, and mirror symmetry of Galactic properties with respect to the Galactic plane. Its (x, y) origin is at the Galactic center, the $\hat{x}$ axis points towards the Earth, and the $\hat{z}$ axis points towards the north Galactic pole. The $\hat{y} = \hat{z} \times \hat{x}$ axis is defined so as to keep the system right handed. The $\hat{x} - \hat{y}$ plane is parallel to the plane of the Galaxy, and the $z = 0$ plane contains the Sun. The Galaxy rotates clockwise around the $\hat{z}$ axis (the rotational velocity of the Sun is in the direction of the $-\hat{y}$ axis).

We bin the stars onto a three dimensional rectangular grid in these coordinates. The choice of grid pixel size is driven by compromise between two competing requirements: keeping the Poisson noise in each pixel at a reasonable level, while simultaneously avoiding overbinning (and related information loss) in high-density regions of the maps. By manual trial-and-error of a few different pixel sizes, we come to a size (for each color bin) which satisfies both requirements. The pixel sizes used are listed in table 2. For bins with $r-i > 0.3$ the median number of stars per pixel is ∼ 10, growing to ∼ 30 for the bluest $r-i$ bin.

For each volume limited (ri_0, ri_1) color bin sample, this results in a three-dimensional data cube, a *map*, of observed stars with each (x, y, z) pixel value equal to the number of stars observed in $(x - dx/2, x + dx/2)$, $(y - dx/2, y + dx/2)$, $(z - dx/2, z + dx/2)$ interval.

Not all of the pixels in the maps have had their volume fully sampled by the SDSS survey. This is especially true near the edges of the survey volume, and at places where there are holes in the footprint of the survey (cf. figure 3). In order to convert the number of stars observed in a particular pixel (x, y, z) to density, we must know the fraction of pixel volume that was actually sampled by the

[16] To avoid excessive usage of parenthesis, we sometimes drop the minus sign when referring to the colors (e.g. $g - r \equiv gr$ or $(r-i)_1 \equiv ri_1$).

survey. Although simple in principle, the problem of accurately binning the surveyed volume becomes nontrivial due to overlap of observing runs, complicated geometry of the survey, and the large survey area. We solve it by shooting a dense, horizontal, rectangular grid of vertical ($x_r = const, y_r = const$) rays through the observed volume, with horizontal spacing of rays dx_r being much smaller than the pixel size dx (typically, $dx_r/dx = 0.1$). For each ray, we calculate the intervals in z coordinate in which it intersects each imaging run (*"ray-run intersections"*). Since imaging runs are bounded by simple geometric shapes (cones, spheres and planes), the ray-run intersection calculation can be done almost completely analytically, with the only numerical part being the computation of roots of a $4^{\rm th}$ order polynomial. For each ray, the union of all ray-run intersections is the set of intervals in space $([z_0, z_1), [z_2, z_3), [z_4, z_5), ...)$ at a given column (x_r, y_r) which were sampled by the survey. It is then a simple matter to bin such interval sets in $\hat{z}$ direction, and assign their parts to pixels through which they passed. Then, by approximating that the ray sweeps a small but finite area dx_r^2, the survey volume swept by the ray contributing to pixel (x, y, z) is simply dx_r^2 times the length of the ray interval(s) within the pixel. By densely covering all of the (x, y) plane with rays, we eventually sweep the complete volume of the survey and partition between all of the (x, y, z) pixels. This ray-tracing method is very general and can handle any survey geometry in any orientation, as long as the survey geometry can be represented by a set of *runs* along great circles. Using this approach, we compute the volume observed within each pixel with an accuracy of one part in 10^3.

In summary, for each of the 19 $r-i$ color bins, we have a three-dimensional map with each (x, y, z) pixel holding the number of observed stars (N) and the observed volume (V). We estimate the number density in any given pixel within a map by

$$\rho(x, y, z) = \frac{N(x, y, z)}{V(x, y, z)}. \quad (17)$$

The shot noise induced error in density estimate is computed as

$$\sigma_\rho(x, y, z) = \frac{\sqrt{N(x, y, z)}}{V(x, y, z)} \quad (18)$$

For each pixel we also track additional auxiliary information (e.g. a list of all contributing SDSS runs), mainly for quality assurance and detailed a posteriori analysis.

3. ANALYSIS OF THE STELLAR NUMBER DENSITY MAPS

The $r - i$ color range spanned by the 19 color bins (0.10–1.40) probes a large distance range. As the bin color is varied from the reddest to the bluest, the subsamples cover distances ranging from 100 pc to 15 kpc. In this Section we analyze these 19 stellar number density maps constructed as described above. We first present a qualitative survey of the various map cross-sections, and then proceed with a quantitative description within the context of "standard" Galactic models.

3.1. *A Qualitative Survey of the Number Density Maps*

3.1.1. *The Number Density Maps in the $R - Z$ Plane*

We first analyze the behavior of two-dimensional maps in the $R - Z$ plane, where $R = \sqrt{x^2 + y^2}$ and $Z = z$ are the galactocentric cylindrical coordinates. Assuming that the Galaxy is circularly symmetric (we critically examine this assumption below), we construct these maps from the three-dimensional maps by taking a weighted mean of all the values for a given $Z - R$ pixel (i.e. we average over the galactocentric polar angle ϕ). We show a subset of these maps in Fig. 6. They bracket the analyzed $r - i$ range; the remaining maps represent smooth interpolations of the displayed behavior.

The bottom two panels in Fig. 6 correspond to the reddest bins, and thus to the Solar neighborhood within ~ 1 kpc. They show a striking simplicity in good agreement with a double exponential disk model:

$$\rho(R, Z) = \rho(R_\odot, 0)\ \exp\left(-\frac{R - R_\odot}{L}\right)\ \exp\left(-\frac{|Z + Z_\odot|}{H}\right). \quad (19)$$

Here ρ is the number density of disk stars, $R_\odot$ and $Z_\odot$ are the cylindrical coordinates of the Sun, and L and H are the exponential scale length and scale height, respectively. This model predicts that the isodensity contours have the linear form

$$|Z + Z_\odot| = C - \frac{H}{L} R, \quad (20)$$

where C is an arbitrary constant, a feature that is in good agreement with the data.

As the bin color becomes bluer (the middle and top panels), and probed distances larger, the agreement with this simple model worsens. First, the isodensity contours become curved and it appears that the disk flares for $R > 14$ kpc. Further, as we discuss below, the Z dependence deviates significantly from the single exponential given by eq. 19, and additional components are required to explain the Z dependence displayed by the data.

We test whether the number density maps are circularly symmetric by examining isodensity contours on a cylindrical surface at $R = R_\odot$ kpc. Fig. 7 shows such projections for two color bins, where we plot the dependence of isodensity contours on galactocentric azimuth ϕ, and distance from the plane Z. In case of circular symmetry, the contours would be horizontal. The top panel shows the isodensity contours for the $1.0 < r - i < 1.1$ color bin, which (in terms of this plot) is representative of all bins redder than $r - i \geq 0.35$ mag. The contours are horizontal, and the number density maps are indeed approximately circularly symmetric. However, for bins $r - i < 0.35$ mag, detectable deviations from circular symmetry do exist, especially at large distances from the Galactic plane (a few kpc and beyond). We show an example of this in the bottom panel, where there is a slight upturn of the isodensity contour at $Z \sim$10,000 and $\phi \sim 40$ deg, indicating the presence of an overdensity. We will discuss such overdensities in more detail in the following section.

3.1.2. *The $X - Y$ Cross-sections of the 3-dimensional Number Density Maps*

Instead of contracting the three-dimensional maps by taking the mean of all the values for a given $Z - R$ pixel,

two-dimensional analysis can be based on simple cross-sections parallel to an appropriately chosen plane. A convenient choice is to study the $X-Y$ cross-sections that are parallel to the Galactic plane. A series of such projections for the bluest color bin is shown in Figs. 8–10. Their outlines are determined by the data availability. In particular, the gap between the two largest data regions will be eventually filled in as more SDSS imaging data becomes available[17].

An unexpected large overdensity feature is easily discernible in all six panels in Fig. 8. In all standard Galaxy models, the stellar density in the upper half should mirror the bottom half ($Y < 0$), and in most models density depends only on the distance from the center of the Galaxy (each annulus enclosed by two successive circles should have roughly a single color). In contrast, the observed density map, with a strong local maximum offset from the center, is markedly different from these model predictions. This is the same feature that is responsible for the structure visible at Z ∼10 kpc and R ∼5 kpc in the top left panel in Fig. 6, and for the upturn of the isodensity contour at Z ∼10,000 and $\phi \sim 40$ in in the bottom panel in Fig. 7. We discuss this remarkable feature in more detail in Section 4.

The top three panels (Z=3-5 kpc) in Fig. 9 clearly show another local overdensity at $R \sim 16$ kpc and $Y \sim 0$. This is the "Monoceros Stream" discovered by Newberg et al. (2002) using a subset of the data analyzed here (this overdensity is also discernible in the top left panel in Fig. 6 at $R \sim 16$ kpc and $Z \sim 3.5$ kpc). The maps discussed here suggest that the stream is well localized in the radial direction with a width of ~ 3 kpc. This well-defined width rules out the hypothesis that this overdensity is due to disk flaring. An alternative hypothesis of a "ring" around the Galaxy, proposed by Ibata et al. (2003), was questioned by Rocha-Pinto et al. (2003). They analyzed 2MASS M giants and concluded that this structure is not a homogeneously dense ring that surrounds the Galaxy but possibly a merging dwarf galaxy with tidal arms. The inhomogeneity of the stream apparent in top three panels of Fig. 9, as well as $R = const.$ projections of these maps, support the conclusions by Rocha-Pinto et al.

Closer to the plane, at distances less than about 1 kpc, the number density maps typically become smoother and less asymmetric, with deviations from a simple exponential model given by eq. 19 not exceeding 30-40% (measured upper limit). This is true of all color bins for which region closer than ~ 1 kpc is well sampled, and is shown in Fig. 10 for $1.0 < r - i < 1.1$ color bin.

3.2. *A Quantitative Interpretation of the Number Density Maps*

Traditionally, the stellar distribution of the Milky Way has been decomposed into several components: the thin and thick disks, the central bulge, and a much more extended and tenuous halo. While it is clear from the preceding discussion that there are a number of overdensities that rule out this simplistic model, the dynamic range of the number density variation in the Galaxy (orders of magnitude) is large compared to the local density excess due to those features (a factor of few). Hence, it should still be possible to capture the overall density variation using simple models, and here we attempt to analyze the number density maps using exponential disks and power-law elliptical halos. Before attempting a full complex multi-parameter fits to the overall number density distribution, we perform a simple quantitative analysis of the density variation in the radial (R) and vertical (Z) directions. We do this type of analysis to get a better understanding of what types of models are at all compatible with the data, and to obtain the starting values of parameters for global multi-parameter fits.

3.2.1. *The Thin and Thick Disks Plus Elliptical Halo Models*

The qualitative analysis of the number density maps from the preceding section, as well as a quantitative analysis of the density variation in the radial R and vertical Z directions described further below, suggest that the gross behavior can be captured by assuming "standard" Galaxy models. Such models are typically based on two exponential disks and a power-law elliptical halo. Following earlier work (see e.g. Majewski 1993, Siegel et al. 2002, Chen et al. 2002), we assume that the overall number density is the sum of disk and halo contributions

$$\rho(R,Z) = \rho_D(R,Z) + \rho_H(R,Z). \quad (21)$$

We ignore the bulge contribution because the maps analyzed here only cover regions more than 3-4 kpc from the Galactic center, where the bulge contribution is negligible compared to the disk and halo contributions (for plausible bulge parameters determined using IRAS data for asymptotic giant stars, see e.g. Jackson, Ivezić & Knapp 2002).

The disk is modeled as a sum of two exponential components, allowing for different scale lengths and heights:

$$\rho_D(R,Z) = \rho_D(R,Z;L_1,H_1) + \epsilon_D \rho_D(R,Z;L_2,H_2) \quad (22)$$

where

$$\rho_D(R,Z;L,H) = \rho_D(R_\odot,0)\exp(-\frac{R-R_\odot}{L} - \frac{|Z+Z_\odot|}{H}) \quad (23)$$

Here H_1, H_2 and L_1 and L_2 are the scale heights and lengths for the thin and thick disk, respectively, ϵ_D is the thick disk normalization relative to the thin disk at ($R = R_\odot, Z = 0$), and $Z_\odot$ is the Solar offset from the Galactic plane. From previous work, typical best-fit values are H_1 ∼300 pc, H_2 ∼1-2 kpc, ϵ_D ∼1-10% and $Z_\odot$ ∼10-50 pc (e.g. Siegel et al. 2002, table 1). We also explored models with the same scale length for the two disk components, that is a linear function of the distance from the Galactic plane.

The halo is modeled as a two-axial power-law ellipsoid

$$\rho_H(R,Z) = \rho_D(R_\odot,0)\,\epsilon_H \left(\frac{R_\odot}{\sqrt{R^2+(Z/q_H)^2}}\right)^\alpha. \quad (24)$$

Here parameter q_H controls the halo ellipticity, with the ellipsoid described by axes $a = b$ and $c = q_H\,a$. For $q_H < 1$ the halo is oblate, that is, "squashed" in the same sense as the disk. The halo normalization relative to the thin disk at ($R = R_\odot, Z = 0$) is specified by ϵ_H.

[17] This region of the sky has already been imaged, and will be a part of SDSS Data Release 5 projected to be released in July 2006.

From previous work, typical best-fit values are α ∼2.5-3.0, $\epsilon_H \sim 10^{-3}$ and $q_H \sim 0.5 - 1$.

Even with this minimalistic model, there are still as many as ten free parameters. It is not easy to assess the uniqueness of a best-fit model, nor to understand interplay between the fitted parameters. As an illuminating example of fitting degeneracies, we show in Fig. 11 density distributions for two significantly different models: a thin plus thick disk model without a halo, and a single disk plus halo model. Despite this fundamental intrinsic difference, it is possible to fine-tune the model parameters to produce nearly identical Z dependence of the density profiles at $R = 8$ kpc. An immediate conclusion is that pencil beam surveys with a limited sky coverage cannot break such model degeneracies. As shown in the bottom panel, significant differences between these two models are only discernible at $|Z| > 3$ kpc and R significantly different from 8 kpc.

Similarly, even when the halo is postulated to exist, Fig. 12 shows that there are severe degeneracies in the best-fit parameters. The large sky area observed by the SDSS can alleviate some of these degeneracies, but not all. For example, the regions with large Z, where it is easy to distinguish various thick disk and halo models, are "contaminated" by large irregular overdensities. In order to assess the plausibility of the adopted Galaxy model, we first examine the density variation in the radial R and vertical Z directions for several characteristic lines of sight.

3.2.2. *The Z-dependence of the Number Density*

Fig. 13 shows the stellar number density for several color bins as a function of the distance from the Galactic plane, Z, at $R = R_\odot$. The behavior for red bins, which probe the heights from 50 pc to ∼1 kpc, is shown in the top panel. They are all well fit by an exponential distribution[18] with a scale height of 270 pc[19]. While the absolute value of this scale height is uncertain to at least 10% (due to possible systematic errors in the adopted photometric parallax relation), it is encouraging that the same value applies to all the bins. This indicates that the slope of the adopted photometric parallax relation is not greatly incorrect at the red end.

The extrapolations of the best exponential fits for $Z < 0$ and $Z > 0$ to small values of $|Z|$ cross at $Z = (24 \pm 5)$ pc. This is the well-known Solar offset from the Galactic plane towards the north Galactic pole (e.g. Reid & Majewski 1993), which is here determined essentially directly using a few orders of magnitude greater number of stars (several million). The quoted uncertainty is determined by simply assuming a 20% systematic uncertainty in the adopted distance scale, and does not imply a Gaussian error distribution (the formal random fitting error is much smaller than 1 pc).

By selecting bluer bins, the Z dependence of the number density can be studied beyond 1 kpc, as illustrated in the middle panel. At these distances the number density clearly deviates from a single ∼270 pc disk model. The excess of stars at distances beyond 1 kpc, compared to this model, is usually interpreted as evidence for another disk component, the thick disk. The data shown in the middle panel in Fig. 13 provide robust constraint on the thick disk parameters because of a large dynamic range of distances and a large number of stars. We later show that the thick-to-thin disk scale height ratio is 4.3, with an uncertainty of less than about 10%. The normalization of the thick disk, relative to the thin disk, is 0.04, with an uncertainty of about ±0.015. These parameters may be somewhat biased because the fits do not include the halo component.

The need for yet another, presumably halo, component, is discernible in the bottom panel in Fig. 13, which shows the number density for the bluest color bin. The data show that beyond 3-4 kpc even the thick disk component underpredicts the observed counts. The observations can be explained by adding a power-law halo component such as described by eq. 24.

Although the density profiles shown in Fig. 13 are determined with high signal-to-noise ratios, it is somewhat disturbing that multiple components are introduced to explain the data, especially since they are simply phenomenological descriptions without a firm physical basis. Could it be that, for example, the thick disk component is an artifact of interplay between the thin disk and halo?

We address this question by exploiting the fact that halo stars have lower metallicities than disk stars by about 1-2 dex. Such a large difference in metallicity affects the $u - g$ color of turn-off stars. An analysis of SDSS colors for Kurucz model atmospheres (Ivezić et al., in prep.) suggests that stars at the tip of the stellar locus with $0.7 < u - g \lesssim 1$ necessarily have metallicities lower than about −1.5. These stars also have markedly different kinematics further supporting the claim that they are halo stars (Bond et al., in prep.).

We select two subsamples of stars from the $0.10 < r - i < 0.15$ color bin: low metallicity halo stars with $0.60 < u - g < 0.95$, and high metallicity disk stars with $0.95 < u - g < 1.15$. This separation is of course only approximate and significant mixing is expected both at the faint end (disk stars contaminated by the more numerous halo stars) and at the bright end (halo stars contaminated by the more numerous disk stars). Nevertheless, the density profiles for these two subsamples, shown in Fig. 14, are clearly different. In particular, the disk profile is much steeper, and dominates for $Z \lesssim 3$ kpc, while the halo profile takes over at larger distances from the Galactic plane. This behavior suggests that the multiple components visible in the bottom panel in Fig. 13 are not an over-interpretation of the data. In addition to supporting a separate low-metallicity halo component, this test shows that a single exponential disk model is insufficient to explain the density profile of high-metallicity stars.

With only the data presented here, one could argue that the thin vs. thick separation is simply a consequence of our attempt to describe the density profile by simple analytic functions. However, there is independent evidence that the two disks are indeed separate Galaxy components, such as the difference in their metallicity

[18] Sometimes the sech^2 function is used instead of exponential dependence. The latter function provides a significantly better description of the data than the former. For example, the exponential distribution is a good fit all the way towards the plane to 1/6 or so of the scale height, where the sech^2 function would exhibit significant curvature in the $\ln(\rho)$ vs. Z plot.

[19] This is the scale height as fitted directly on the data, without accounting for the Malmquist bias. The Malmquist corrected scale height is 280pc (see Eqs. 30)

distributions (e.g. Bensby et al. 2005 for the Milky Way, and Seth, Dalcanton & deJong 2005 for external galaxies) or the difference in kinematics (e.g. Parker et al. 2004 and references therein).

3.2.3. *The R-dependence of the Number Density*

We analyze the dependence of number density on the (cylindrical) distance from the Galactic center in Figs. 15, 16 and 17. Each figure shows the number density as a function of R for a given $r-i$ color bin at different heights above the Galactic plane. For red bins, which probe the Solar neighborhood within ∼1 kpc, the density profiles are approximately exponential (i.e. straight lines in $\ln(\rho)$ vs. R plot, see Fig. 15). The exponential scale length seems to increase with the distance from the Galactic plane, but due to the small baseline this variation is not strongly constrained. Indeed, the scale length itself is not well determined, with plausible values around 3.5 kpc and an uncertainty of at least 30%.

At distances from the Galactic plane exceeding 1-2 kpc, the exponential radial dependence is a fairly poor fit to the observed density profile (Fig. 16). It appears that the main source of discrepancies are several overdensities mentioned in the preceeding sections. In particular, the Monoceros stream is particularly prominent at Z ∼2-8 kpc, especially when the density profiles are extracted only for $|Y| < 1$ kpc slice (Fig. 17).

3.2.4. *Global Galactic Model Fits*

As is evident from the preceding discussion, the global fitting of models described by eqs. 21–24 will be biased by various overdensities so the best-fit results have to be constructed and interpreted with caution. Despite the difficulties, we were able to obtain satisfactory model fits for the disk components of the Galaxy, and by subsequent subtraction from the data, to reveal lower-level overdensities that were not easily detectable otherwise.

To obtain a reliable global fit we begin by excluding the regions where obvious localized deviations exist. The excluded regions are shown in figure 18. We exclude the newly found large overdensity discernible in Fig. 8 (the "Virgo overdensity") by masking the pixels that simultaneously satisfy:

$$\sin(30^\circ)(X - 8\,\mathrm{kpc}) - \cos(30^\circ)Y < 0$$
$$\sin(120^\circ)X - \cos(120^\circ)Y > 0 \qquad (25)$$
$$(X - 8\,\mathrm{kpc})^2 + Y^2 + Z^2 > (2.5\,\mathrm{kpc})^2 \qquad (26)$$

The third condition is to exclude from the cut the pixels closer than 2.5kpc to the Sun, as those are uncontaminated by the overdensity. The region excluded by eqs. 25 is shown bounded by the rectangle in top panel of figure 18. The Monoceros stream is approximately parallel to the plane of the galaxy and located at a constant galactocentric radius. We exclude it by masking all pixels that satisfy either of the two conditions:

$$13\,\mathrm{kpc} < R < 19\,\mathrm{kpc} \wedge 0 < Z < 5\,\mathrm{kpc} \qquad (27)$$
$$16\,\mathrm{kpc} < R < 19\,\mathrm{kpc} \wedge 0 < Z < 7\,\mathrm{kpc} \qquad (28)$$

which corresponds to the region bounded by the white polygon in the bottom panel in Fig. 18.

The remaining pixels are averaged over the galactocentric polar angle ϕ, to produce the equivalent of (R, Z) maps shown in fig. 6. We show all 19 "cleaned up" maps in figure 19. The contours denote the locations of constant density. The gray areas show the regions with available SDSS data. Compared to Fig. 6, the constant density contours are much more regular, and the effect of the Virgo overdensity is largely suppressed. The regularity of the density distribution is particularly striking for redder bins (e.g., for $r - i > 0.7$). In the bluest bin ($0.10 < r - i < 0.15$), there is a marked departure from a smooth profile in the top left part of the sampled region. This is the area of the (R, Z) plane where the pixels that are sampled far apart in (X, Y, Z) space map into adjacent pixels in (R, Z) space. Either deviations from axial symmetry or small errors in photometric parallax relation can lead to deviations of this kind. Unfortunately, which one of the two it is, is impossible to disentangle with the data at hand.

We begin the modeling by fitting a single exponential disk to the three reddest color bins to find the value of the Solar offset $Z_\odot$ and disk normalization $\rho_D(R = R_\odot, Z = 0)$. To avoid contamination by the thick disk, we only use the pixels with $|Z| < 500$pc, and to avoid effects of overestimated interstellar extinction correction for the nearest stars (Section 2.3.2), we further exclude pixels with $|Z| < 100$. In all three bins we obtain the same best fit value of the Solar offset:

$$Z_\odot = (24 \pm 5)\,\mathrm{pc} \qquad (29)$$

The quoted uncertainty is determined by simply assuming a 20% systematic uncertainty in the adopted distance scale, and does not imply a Gaussian error distribution (the formal random fitting error is much smaller than 1 pc). The value of the Solar offset we obtain is in very good agreement with recent independent measurements ($Z_\odot = (27.5 \pm 6)$ pc, Chen et al. 1999; $Z_\odot = (27 \pm 4)$ pc, Chen et al. 2001; (24.2 ± 1.7) pc obtained from trigonometric Hipparcos data by Maíz-Apellániz 2001). Keeping the value of the Solar offset and density normalization fixed, using the standard Levenberg-Marquardt nonlinar fit procedure, we simultaneously fit all of the remaining free parameters in eq. 22 (L_1, L_2, H_1, H_2 and ϵ_D) in the four reddest color bins ($r - i \geq 1.0$). To account for the effects of Malmquist bias (Teerikorpi 1997), we generate Monte Carlo simulations of the data within the survey area and flux limits, and put it through the same fitting procedure. We assume that the intrinsic scatter in the photometric paralax relation is the dominant contributor to error in distance estimate, and take it to follow a Gaussian distribution with with $\sigma_{M_{r,i}} = 0.3$ mag when converting the magnitudes of simulated stars to distances. We vary the simulated model parameters until the fitted model parameters of the simulation are equal to the fitted model parameters of the data. The fits (corrected for Malmquist bias as described above) rapidly converge to:

$$H_1 = (280 \pm 10)\,\mathrm{pc} \qquad (30)$$
$$L_1 = (2400 \pm 200)\,\mathrm{pc} \qquad (31)$$
$$H_2 = (1200 \pm 50)\,\mathrm{pc} \qquad (32)$$
$$L_2 = (3500 \pm 1000)\,\mathrm{pc} \qquad (33)$$
$$\epsilon_D = 0.04 \pm 0.015 \qquad (34)$$

The solution is the mean of the best-fit values obtained in the four bins, and the quoted uncertainty is the variance

between them. Residual maps for fits in these four bins show very small residuals and little or no structure (see the bottom two rows in Fig. 20). Reduced χ^2 values for the fits are in the $1.5 - 2.3$ range.

Obtaining good disk fits for maps of stars bluer than $r - i = 1.0$ becomes exceedingly difficult due to an increasingly large influence of the stellar halo for $|Z| > 3$ kpc, and small, previously unnoticed, deviations from a smooth density profile. The panels in Fig. 20 illustrate fitting results for four color bins where the influence of the halo and localized features is the largest. The columns, from left to right, show the data, the model and the residuals. The bottom three rows are results of fitting a disk-only model, while the top row also includes a fit for the halo.

While the best-fit models appear to be in qualitatively good agreement with the data, the residual maps show some localized features. The most prominent feature is found at practically the same position ($R \sim$6.5 kpc and $Z \sim 1.5$ kpc) for all color bins, and in figure 20 is the most prominent in the top right panel. Since the apparent (and absolute) magnitudes of stars in this feature vary by $\sim$3.5 mag from the bluest to the reddest color bin, this consistency suggests that the adopted photometric parallax relation doesn't have large systematic errors. The feature itself is not symmetric with respect to the Galactic plane, though a weaker counterpart seems to exist at $Z < 0$. Another smaller overdensity is noticeable in all but the reddest Data-Model panel of figure 20 at $R \sim 9$ kpc and $Z \sim 0.8$ kpc, apparently extending for $\sim$1 kpc in the radial direction.

For even bluer color bins the probed distance range is larger and the halo component plays an important role. Because of the Monoceros and Virgo overdensities, the best-fit halo parameters are probably biased. Nevertheless, it is possible to derive some robust conclusions about the halo properties. Fig. 21 shows residual maps for the bluest color bin and for four different halo models, with the thin and thick disk parameters kept fixed at values determined using redder bins (eqs. 30-34). The Monoceros and Virgo overdensities, and the overdensity at $R \sim$6.5 kpc and $Z \sim 1.5$ kpc, are clearly evident, but their detailed properties significantly depend on the particular halo model subtracted from the data. It appears that the halo power-law index is only weakly constrained to be between 2 and 3. We also find that a power-law halo model always over- or underestimates the stellar counts in the far outer halo, suggesting the use of a different profile may be more appropriate. However, no matter what the exact shape of the profile or the power law index is, only significantly oblate halos with $q_H \sim 0.5$ provide good fits to the data (compare the top two panels in Fig. 21). The formal best-fit halo parameters for data shown in figure 21 are $\alpha = 2.3$, $q_H = 0.45$, and ϵ_H=0.001.

We emphasize that these halo models, especially the best-fit values of the power law index and the normalization, should be interpreted with caution because the analyzed data set is insufficient to fully mask various overdensities. The currently unprocessed SDSS observations taken after September 2003 cover a larger area, and their analysis, including an attempt to explicitly model the most significant overdensities, will be presented in a subsequent paper.

4. THE VIRGO OVERDENSITY

As briefly discussed in Section 3.1.2, the $X-Y$ projections of the number density maps at the heights above 5 kpc from the Galactic plane show a strong deviation from expected circular symmetry. In this Section we explore this remarkable feature in more detail. We refer to this feature as *"the Virgo overdensity"* because the highest detected overdensity is in the direction of constellation Virgo.

4.1. *The Extent and Profile of the Virgo overdensity*

To quantify the extent and profile of the Virgo overdensity, we only consider the data in the region that passes through the Galactic center, and is rotated $\phi = 30°$ clockwise around the $\hat{z}$ axis (see Fig. 8). In the top left panel in Fig. 22 we show the projection of the corresponding number density map in the Z vs. R plane for the bluest color bin. Isodensity contours show a significant deviation from a monotonic decrease with R, expected for a cylindrically symmetric Galaxy. Instead, the contours indicate the existence of an overdense region around $R \sim$ 7-8 kpc and $Z \sim$10 kpc. The radial density profiles for several heights above the Galactic plane are shown in Fig. 23. As discernible from the figure, the Virgo overdensity is responsible for at least a factor of 2 number density excess when $Z > 10$ kpc.

In order to further quantify this feature, we subtract a Galaxy model from the data shown in the top panel in Fig. 22. We fit a model described by eqs. 21–24 to the part of the observed map with $Y < 0$. As suggested by Fig. 8, this region does not seem significantly affected by the Virgo overdensity. The ratio of the observed map and the best-fit model is shown in the top right panel in Fig. 22. The data-to-model ratio map shows with much more detail the extent and location of the Virgo overdensity. There is a significant excess (up to a factor of 3) over the entire sampled Z range ($5 < Z/\mathrm{kpc} < 15$).

The importance of the Virgo overdensity, relative to the smooth Milky Way background, increases with Z. This increase is due to the fast decrease of the Milky Way number density with Z, which causes the ratio of the two components to increase with Z. However, the number density of the Virgo feature increases towards the Galactic plane, as shown in the bottom panels in Fig. 22. Because no local maximum is detected as Z approaches the data region boundary at $Z = 5$ kpc, the true vertical (Z) extent of the overdensity cannot be quantified with the currently available data. It is possible that it extends all the way into the Galactic plane and, if it is a merging galaxy or stream, perhaps even to the southern Galactic hemisphere.

In the radial direction, the Virgo overdensity is detected in the $2.5 < R/\mathrm{kpc} < 12.5$ region. The thickness of the overdensity in the direction perpendicular to the plane of the image in Fig. 22 (the "Y'" direction) is not less than 5 kpc. As in the case of the Z direction, the true extent remains unknown because of the current data availability. Note that the size of the overdensity as seen in the maps in the direction of the line of sight towards the Sun, is a combination of true size and the smearing induced by the photometric measurement and paralax errors (Fig. 4), and could therefore be an overestimate on the order of 20-25%.

The bottom two panels of figure 22 attempt to visualize the morphology of the Virgo overdensity. The number density in this feature decreases with the height from the Galactic plane. The position of the maximum density moves from $R \sim$6 kpc at $Z = 5$ kpc to $R \sim$7 kpc at $Z = 15$ kpc. The width ("full-width at half density") decreases by a factor of ~ 2 as Z increases from 5 to 15 kpc. While not a definitive proof, these properties are consistent with a merging galaxy or stream.

4.2. *Direct Verification of the Virgo Overdensity*

Significant data processing was required to produce maps such as the one revealing the Virgo overdensity (e.g. the top left panel in Fig. 22). In order to test and examine this find in a more direct, and presumably more robust, way, we examine the Hess diagrams constructed for the region of the sky that includes the maximum overdensity, and for a control region that appears unaffected by the Virgo feature. The boundaries of these two regions, which are symmetric with respect to the $l = 0$ line, the corresponding Hess diagrams, and their difference, are shown in Fig. 24.

The top left panel of Fig. 24 shows the northern (in Galactic coordinates) sky density of stars with $0.2 < g - r < 0.3$ and $20 < r < 21$ in the Lambert equal area projection of Galactic coordinates (the north Galactic pole is in the center, l=0 is towards the left, and the outermost circle is $b = 0°$). This map projection does not preserve shapes (it is not conformal, Gott et al. 2005), but it preserves areas - the area of each pixel in the map is proportional to solid angle on the sky, which makes it particularly suitable for study and comparison of counts and densities on the celestial sphere. The color and magnitude constraints select stars in a $D \sim 13$ kpc heliocentric shell, and can be easily reproduced using the publicly available SDSS database. The Virgo overdensity is clearly visible even with these most basic color and magnitude cuts, and extends over a large patch of the sky, roughly in the $l = 300°, b = 65°$ direction. The overall number density distribution is clearly *not* symmetric with respect to the horizontal $l = 0, 180$ line. For example, in the $D \sim 13$ kpc shell there are 1.85 ± 0.03 times more stars in the $l = 300°, b = 65°$ direction, than in the corresponding symmetric ($l = 60°, b = 65°$) direction, a $\sim 28\sigma$ deviation from a cylindrically symmetric density profile. When the color range is sufficiently red (e.g. $0.9 < g - r < 1.0$), and in the same magnitude range, the asymmetry disappears (not shown). These stars have a smaller absolute magnitude and are therefore much closer.

The two panels to the right in Fig. 24 show the Hess diagrams for two 540 deg^2 large regions towards ($l = 300°, b = 60°, top$) and ($l = 60°, b = 60°, bottom$) (marked as polygons in the top left panel). The bottom left panel shows the Virgo field CMD after the control field has been subtracted. Note the strong overdensity at $g - r \sim 0.3$ and $r \gtrsim 20$. We quantitatively analyze the Hess diagram difference in figure 25. For red stars the counts in two regions are indistinguishable, while for blue stars the counts difference is highly statistically significant. There is no indication for a turnover in blue star number count difference strongly suggesting that the Virgo overdensity extends beyond the SDSS faint limit. We conclude that the Hess diagram analysis robustly proves the existence of a significant star count overdensity towards $l = 300°, b = 65°$ direction, from approximately $r \sim 18$ mag to $r \sim 21.5$ mag.

From the diagram in bottom left panel of Fig. 24, a crude estimate of the surface brightness of the overdensity can be made by summing up the fluxes of all stars in the CMD and dividing the total flux by the area observed. To isolate the overdensity, we only count the fluxes of stars satisfying $0.2 < g - r < 0.8$ and $18 < r < 21.5$. *This will effectively be a lower limit,* because we will miss stars dimmer than the limiting magnitude ($r = 21.5$), and bright giants ($r < 18$). We obtain a value of:

$$\Sigma_r = 32.5 \,\mathrm{mag\,arcsec^{-2}} \quad (35)$$

This is about a magnitude and a half fainter than the surface brightness of Sagittarius dwarf northern stream ($\Sigma_V \sim 31$ mag arcsec^{-2}; Martínez-Delgado et al. 2001, Martínez-Delgado et al. 2004).

Assuming the entire overdensity covers ~ 1000 deg^2 of the sky (consistent with what is seen in the top left panel of Fig. 24), and is centered at a distance of $D \sim$ 10kpc, from the surface brightness we obtain an estimate of the integrated absolute r band magnitude, $M_r = -7.7$ mag. This corresponds to a total luminosity of $L_r = 0.09 \cdot 10^6 L_\odot$, where we calculate the absolute r band magnitude of the Sun to be $M_{r\odot} = 4.6$, using Eqs. 2 and 3 from Jurić et al. (2002), and adopting $(B - V)_\odot = 0.65$ and $V_\odot = 4.83$ from Binney & Merrifield (1998). This luminosity estimate is likely uncertain by at least a factor of a few. Most of the uncertainty comes from the unknown exact distance and area covered by the overdensity. Uncertainty due to the flux limit depends on the exact shape of the luminosity function of stars making up the overdensity, but is likely less severe. For example, assuming that the luminosity function of the overdensity is similar to that of the Solar neighborhood (Reid, Hawley & Gizis 2002, table 4), and that our sample of overdensity stars is incomplete for $g - r > 0.5$ (see bottom left panel of Fig. 24), the corrected luminosity and absolute magnitude are $L_r = 0.10 \cdot 10^6 L_\odot$ and $M_r = -7.8$ (note that only the red end of the luminosity function is relevant here). Taking a more conservative incompleteness bound of $g - r > 0.3$, the luminosity grows to $L_r = 0.11 \cdot 10^6 L_\odot$ (22% difference), or $M_r = -8$, in terms of absolute magnitude. Again, *these are all lower limits.*

4.3. *Metallicity Constraints*

The SDSS u band measurements can be used to gauge metallicity of the Virgo overdensity. As already discussed in Section 3.2.2, stars at the tip of the stellar locus ($0.7 < u - g \lesssim 1$) typically have metallicities lower than about -1.5. This $u - g$ separation can be improved by using instead the principal axes in the $g - r$ vs. $u - g$ color-color diagram (Ivezić et al. 2004)

$$P_{1s} = 0.415(g - r) + 0.910(u - g) - 1.28 \quad (36)$$

$$P_{2s} = 0.545(g - r) - 0.249(u - g) + 0.234 \quad (37)$$

The main sequence stars can be isolated by requiring

$$-0.06 < P_{2s} < 0.06 \quad (38)$$

and the low-metallicity turn-off stars using

$$-0.6 < P_{1s} < -0.3. \quad (39)$$

The high-metallicity turn-off stars have $P_{1s} > -0.2$.

In Fig. 26 we show Hess diagrams of P_{1s} color vs. r magnitude for the Virgo overdensity field and the control field, and their difference. A significant excess of stars with $P_{1s} < -0.3$ exists in the Virgo overdensity field. There is no statistically significant difference in star counts for stars having $P_{1s} > -0.2$. This implies that the Virgo overdensity stars have metallicities lower than (thick) disk stars, and similar to those of halo stars.

4.4. *Detections of Related Clumps and Overdensities*

There are a number of stellar overdensities reported in the literature that are probably related to the Virgo overdensity. Newberg et al. (2002) searched for halo substructure in SDSS equatorial strips ($\delta \sim 0$) and reported a density peak at $(l, b) \sim (297, 63)$. They tentatively concluded that this feature is *"a stream or other diffuse concentration of stars in the halo"* and pointed out that follow-up radial velocity measurements are required to ascertain that the grouping is not a product of chance and statistics of small numbers.

Detections of RR Lyrae stars are particularly useful because they are excellent standard candles. Using RR Lyrae detected by the QUEST survey, Vivas et al. (2001, see also Zinn et al. 2003) discovered an overdensity at $\sim$ 20 kpc from the Galactic center at $(l, b) \sim (314, 62)$ (and named it the "$12^{\rm h}.4$ clump"). The same clump is discernible in the SDSS candidate RR Lyrae sample (Ivezić et al. 2000, 2003bcd). More recently, the NSVS RR Lyrae survey (Wozniak et al. 2004) detected an overdensity in the same direction, and at distances extending to the sample faint limit, corresponding to about ∼6 kpc (P. Wozniak, private communication).

2MASS survey offers an all-sky view of the Milky Way. We have followed a procedure developed by Majewski et al. (2003) to select M giant candidates from the public 2MASS database. We find a significant excess of candidate giants in the Virgo overdensity area, compared to a region symmetric with respect to the $l = 0$ line. Both the number ratio and implied distances (using M giant candidates that belong to the Sgr dwarf stream, we estimate that their mean magnitude at 10 kpc is $K \sim 9.7$, for more details see Majewski et al. 2003 and Ivezić et al. 2003cd) are consistent with the properties of the Virgo overdensity inferred from SDSS data. For example, the distribution of high-latitude ($55^\circ < b < 80^\circ$) M giant candidates selected using $9.2 < K < 10.2$ and $1.0 < J - K < 1.3$ is very asymmetric with respect to the galactic longitude: there are 66 stars with $240 < l < 360$, and only 21 stars with $0 < l < 120$, with the former clustered around $l \sim 300$. There is no analogous asymmetry in the southern Galactic hemisphere. The sky distribution of the northern 2MASS M giant candidates is shown in Fig. 27.

While these independent detections are insufficient to fully resolve the nature of the overdensity (either because of insufficient sky coverage, or a small number of tracer stars), they provide strong support that this feature is real, and not a product of the photometric parallax method used in this work.

4.5. *A Merger, Tri-axial Halo, Polar Ring, or?*

The Virgo overdensity is a major new Galaxy feature: even within the limited sky coverage of the available SDSS data, it extends over a thousand square degrees of sky. Given the well defined overdensity outline, low surface brightness and luminosity, its most plausible explanation is that of a tidally disrupted reminant of a merger event involving the Milky Way and a smaller, lower-metallicity dwarf galaxy. However, there are other possibilities.

An attempt may be made to explain the detected asymmetry by postulating a non-axisymmetric component such as a triaxial halo. This alternative is particularly interesting because Newberg & Yanny (2005), who essentially used the same data as analyzed here, have suggested that evidence for such a halo exists in SDSS starcounts. A different data analysis method employed here – the three-dimensional number density maps – suggests that the excess of stars associated with the Virgo overdensity is *not* due to a triaxial halo. The main argument against such a halo is that, despite its triaxiality, it still predicts that the density decreases with the distance from the Galactic center. But, as shown in Figs. 8 and 23, the observed density profile has a local maximum that is *not* aligned with the Galactic center. This can still be explained by requiring the axis of the halo to be inclined with respect to the symmetry axis of the Galactic disk. However, even this model requires the halo density to attain maximal value in the Galactic center, and as seen from figure 22 a modest linear extrapolation of Virgo overdensity to $Z = 0$ still keeps it at $R \sim 5.5$ kpc away from the Galactic center.

Nevertheless, while this makes the explanation of the Virgo overdensity by a triaxial halo unlikely, it does not preclude the existence of such a halo. However, it would be very difficult to obtain a reliable measurement of the halo triaxiality with the currently available SDSS data because of "contamination" by the Virgo overdensity and uncertancies about its true extent. As more SDSS and other data become available in other parts of the sky, it may become possible to mask out the overdensity and attempt a detailed halo fit to reveal the exact details of its shape and structure.

Another possible explanation of the Virgo overdensity is a "polar ring" around the Galaxy. This possibility seems much less likely than the merger scenario because there is no visible curvature towards the Galactic center at high Z in Fig. 22. Indeed, there seem to be a curvature in the opposite sense, where the bottom part of the overdense region appears to be about 1 kpc closer to the Galactic center than its high-Z part. In addition, there is no excess of 2MASS M giant candidates in the southern sky that could be easily associated with the northern Virgo overdensity.

Finally, the coincidence of this overdensity and the famous Virgo galaxy supercluster (Binggeli 1999) could raise a question whether the overdensity could be due to faint galaxies that are misclassified as stars. While plausible in principle, this is most likely not the case because the star/galaxy classifier is known to be robust at the 5% level to at least $r = 21.5$ (Ivezić et al. 2002), the overdensity is detected over a much larger sky area (1000 deg^2 vs. $\sim$ 90 deg^2), and the overdensity is confirmed by apparently much brighter RR Lyrae stars and M giants.

5. DISCUSSION

Traditionally, studies of the Milky Way's main components are based on counting stars in a given patch of the sky (although sometimes kinematic data are also utilized). Given the star counts, a standard approach to modeling the structure of the Galaxy is to adopt initial mass function, mass-luminosity relationship, luminosity function, a color-luminosity relation, and a number density parametrization for each Galaxy component deemed important. With these ingredients, one produces model counts as a function of color, apparent magnitude and the position on the sky. The observed stellar counts are then used to constrain the numerous model parameters. In addition to a formidable minimization problem (see e.g. Peiris 2000, and Larsen & Humphreys 2003), a question of uniqueness remains even when a successful best-fit model is found (a good comparison of various methods and their results is presented by Reid & Majewski 1993).

A vivid example of various uncertainties associated with this traditional approach is illustrated in Fig. 1 of Siegel et al. 2002: the thick disk best-fit parameters published by various authors vary by significantly more than the claimed uncertainties. In particular, Siegel et al. pointed out that best-fit parameters based on SDSS data (Chen et al. 2001) are significantly different from other determinations reported in the literature, a discrepancy that partially motivated this work (note, however, that Siegel et al. used data for seven Kapteyn selected areas and obtained similar best-fit parameters for the thick disk as those reported by Chen et al.).

This work represents an attempt at a qualitatively different approach to studies of the Milky Way density structure. In contrast to traditional star count analysis, *here we do not assume any a-priori Galactic model*. Instead, the wide sky coverage and a large number of observed stars allow us to directly construct stellar number density maps of the Galaxy. With these maps, the analysis of Milky Way's structure now becomes more akin to studies of external galaxies.

This qualitative paradigm shift was made possible by the availability of SDSS data. SDSS is superior to previous optical sky surveys because of its high catalog completeness and accurate multi-band photometry to faint flux limits over a large sky area. In particular, the results presented here were enabled by several distinctive SDSS characteristics:

- A large majority of stars detected by the SDSS are main-sequence stars, which have a fairly well-defined color-luminosity relation. Thus, accurate SDSS colors can be used to estimate luminosity, and hence, distance, for each individual star. Accurate photometry ($\sim$ 0.02 mag) allows to reach the intrinsic accuracy of photometric parallax relation, and thus to estimate distances with typical random errors caused by the photometry not exceeding 15-20%.

- Thanks to faint flux limits ($r \sim 22$), distances as large as 15 kpc are probed using numerous main sequence stars ($\sim$ 48 million). At the same time, the large photometric dynamic range and the strong dependence of stellar luminosities on color allow constraints ranging from the Sun's offset from the Galactic plane ($\sim$ 24 pc) to a detection of overdensities at distances beyond 10 kpc.

- Large sky area observed by the SDSS (as opposed to pencil beam surveys), spanning a range of galactic longitudes and latitudes, enables not only a good coverage of the (R, Z) plane, but also of a large fraction of the Galaxy's volume. The full three-dimensional analysis, such as slices of the maps in $X-Y$ planes, reveals a great level of detail.

- The SDSS u band photometric observations can be used to identify stars with sub-solar metallicities, and to study the differences between their distribution and that of more metal-rich stars.

Photometric parallax method has already been used to study the Milky Way structure (Gilmore & Reid 1983, Kuijken & Gilmore 1989, Chen et al. 2001, and for a more complete list see Table 1 in Siegel et al. 2002). An excellent example of the application of this method to pre-SDSS data is the study by Siegel et al. (2002). While their and SDSS data are of similar photometric quality, the sky area analyzed here is over 400 times larger than that analyzed by Siegel et al. This large increase in the sample size enables a shift in emphasis, from modelling to direct model-free *mapping* of the complex and clumpy Galactic density distribution, as exemplified by the discovery of the low-contrast large-area Virgo overdensity. Although the photometric parallax method is prone to systematic errors, and thus the quantitative description of the new structures will be biased, it is evident that the purely smooth description of the Milky Way's main components (e.g. Bahcall & Soneira 1980, Gilmore, Wyse & Kuijken 1989) is an oversimplification.

When the exponential disk models are used to describe the gross behavior of the stellar number density distribution, we obtain the best-fit parameters that are similar to previous work, with the local thick-to-thin disk normalization of $\sim$4% and a somewhat larger ratio of the exponential disk scale heights of 4.3:1. The exponential scale length, particularly that of the thick disk, is much less constrained and varies in the range of 2.5-4.5 kpc. The halo appears oblate, with the axes ratio of $\sim$2, local normalization of $\sim$0.001, and a power-law profile with only weakly constrained index (2–3). We note that the quantitative values of the model parameters presented here should be interpreted with caution, because of the difficulty of getting a "clean" model fit, unaffected by clumpy substructure. Also, possible systematics in the photometric parallax relation, and its large intrinsic scatter, make for an additional source of error to which all of the surveys employing the photometric parallax method, including ours, are intrinsically susceptable.

The most interesting result of our analysis is the discovery of Virgo overdensity and robust evidence for ubiquitous substructure at the edges of, and within the Galactic disk. Despite the size and closeness, the low surface brightness of Virgo overdensity kept it from being recognized by smaller surveys. Given the low surface brightness, its well defined outline, and low metallicity, the most plausible explanation of Virgo overdensity is that it is a result of a merger event involving the Milky Way and a smaller, lower-metallicity dwarf galaxy. For now, based on existing maps, we are unable to differentiate whether the observed overdensity is a tidal stream, a merger remnant, or both. However, it is evident that the Virgo overdensity is suprisingly large, extending in

vertical (Z) direction to the boundaries of our survey ($5 < Z < 15$ kpc), and ~ 10 kpc in R direction. It is also exceedingly faint, with a lower limit on surface brightness of $\Sigma_r = 32.5\,\mathrm{mag\,arcsec^{-2}}$. Assuming that the observed overdensity is just a part of a larger stream, it would be of interest to check for a possible continuation in the southern Galactic hemisphere – our preliminary analysis of 2MASS M-giants data did not reveal a similarly large density enhancement in the south. Also, it would be interesting to follow the stream towards the Galactic north, beyond the $Z \sim 15$ kpc limit of our survey. But above all, the understanding of the Virgo overdensity would probably greatly benefit from measurements of proper motion and radial velocity for its likely constituent stars.

While the rich halo substructure has been known for a while (e.g. Ivezić et al. 2000, Yanny et al. 2000, Vivas et al. 2001, Majewski et al. 2002, and references therein), here we show that the thin and thick disk substructure is equally complex. An approximate extrapolation of the four overdensities seen in our survey volume to the full Galactic disk ($|Z| < 3$kpc, $R < 15$kpc) leads to a conclusion that there are ∼20 - 40 clumpy substructures of this type in the Galaxy. This is comparable to the number of satellite dwarf galaxies predicted by cold dark matter models (Kauffmann, White, & Guiderdoni, 1993, Sellwood & Kosowsky 2002). These satellites have not been confirmed observationally, leading to a discrepancy known as "the missing satellite problem". One may speculate that such satellites have simply merged with the Milky Way, leaving behind a trail of overdensities as their remains. If so, not only is the Milky Way is cannibalizing its neighbors, but it does so with quite an appetite.

The three-dimensional maps offer an effective method to study the properties of individual features such as the Monoceros stream. The maps demonstrate that this feature is well localized in the radial direction, which rules out the hypothesis that this overdensity is due to disk flaring. The maps also show that the Monoceros stream is not a homogeneously dense ring that surrounds the Galaxy, and provide support for the claim by Rocha-Pinto et al. (2003) that this structure is a merging dwarf galaxy (see also Penarrubia et al. 2005). Similarly, the maps demonstrate that the Virgo overdensity appears consistent with an another tidally disrupted merging galaxy or a stream, rather than reflecting an asymmetry due to a triaxial halo.

Despite these results, this study is only a first step towards a better understanding of the Milky Way enabled by modern large-scale surveys. Star counting, whether interpreted with traditional modeling methods, or using number density maps, is limited by the number of observed stars, the flux limit and sky coverage of a survey, and the ability to differentiate stellar populations. All these data aspects will soon be significantly improved.

First, the SDSS has entered its second phase, with a significant fraction of observing time allocated for the Milky Way studies (SEGUE, the Sloan Extension for Galaxy Understanding and Exploration, Newberg et al. 2003). In particular, the imaging of low galactic latitudes and a large number of stellar spectra optimized for Galactic structure studies will add valuable new data to complement this work. In addition, the SDSS kinematics data, both from radial velocities and from proper motions (determined from astrometric comparison of the SDSS and the Palomar Observatory Sky Survey catalog, Munn et al. 2004) is already yielding significant advances in our understanding of the thin and thick disk, and halo kinematic structure (Bond et al., in prep.).

Another improvement to the analysis presented here will come from the GAIA satellite mission (e.g. Wilkinson et al. 2005). GAIA will provide geometric distance estimates and 15-band photometry for a large number of stars brighter than $V \sim 20$. Despite the relatively bright flux limit, these data will be invaluable for calibrating photometric parallax relation, and for studying the effects of metallicity, binarity and contamination by giants. At the moment, the uncertanties of the photometric parallax relation are the single largest contributor to uncertanties in the derived parameters of Galactic models, and improvements in its calibration are of great interest to all practitioners in this field.

A further major leap forward will be enabled by upcoming deep synoptic sky surveys, such as Pan-STARRS (Kaiser 2002) and LSST (Tyson 2002). These surveys will provide multi-band optical photometry of similar, or better, quality as SDSS, over an even larger region of the sky (∼20,000 deg^2). One of their advantages will be significantly deeper data – for example, the LSST will enable studies such as this one to a 5 magnitudes fainter limit, corresponding to a distance limit of 150 kpc for the turn-off stars. LSST proper motion measurements will constrain tangential velocity to within 10 km/s at distances as large as that of the Virgo overdensity reported here (∼10 kpc). These next-generation maps will be based on samples exceeding a billion stars and will facilitate not only the accurate tomography of the Milky Way, but of the whole Local Group.

Acknowledgments

We thank Princeton University and the University of Washington for generous financial support of this research.

Funding for the creation and distribution of the SDSS Archive has been provided by the Alfred P. Sloan Foundation, the Participating Institutions, the National Aeronautics and Space Administration, the National Science Foundation, the U.S. Department of Energy, the Japanese Monbukagakusho, and the Max Planck Society. The SDSS Web site is http://www.sdss.org/.

The SDSS is managed by the Astrophysical Research Consortium (ARC) for the Participating Institutions. The Participating Institutions are The University of Chicago, Fermilab, the Institute for Advanced Study, the Japan Participation Group, The Johns Hopkins University, the Korean Scientist Group, Los Alamos National Laboratory, the Max-Planck-Institute for Astronomy (MPIA), the Max-Planck-Institute for Astrophysics (MPA), New Mexico State University, University of Pittsburgh, University of Portsmouth, Princeton University, the United States Naval Observatory, and the University of Washington.

This publication makes use of data products from the Two Micron All Sky Survey, which is a joint project of the University of Massachusetts and the Infrared Processing and Analysis Center/California Institute of Tech-

nology, funded by the National Aeronautics and Space Administration and the National Science Foundation.

REFERENCES

Abazajian, K., Adelman, J.K., Agueros, M., et al. 2003, AJ, 126, 2081
Adelman, J.K., et al. 2006, ApJ Supp, accepted for publication
Bahcall, J.N. & Soneira, R.M. 1980, ApJSS, 44, 73
Bensby, T., Feltzing, S., Lundström, I., & Ilyin, I. 2005, A&A, 433, 185
Binggeli, B. 1999, LNP Vol. 530: The Radio Galaxy Messier 87, 530, 9
Binney, J., & Merrifield, M. 1998, Galactic astronomy / James Binney and Michael Merrifield. Princeton, NJ : Princeton University Press, 1998. (Princeton series in astrophysics) QB857 .B522 1998
Chen, B., Figueras, F., Torra, J., Jordi, C., Luri, X., & Galadí-Enríquez, D. 1999, A&A, 352, 459
Chen, B., Stoughton, C., Smith, J.A., et al. 2001, ApJ, 553, 184
Fan, X. 1999, AJ, 117, 2528
Finkbeiner, D. P., Padmanabhan, N., Schlegel, D. J., et al. 2004, AJ, 128, 2577
Finlator, K., Ivezić, Ž., Fan, X., et al. 2000, AJ, 120, 2615
Fukugita, M., Ichikawa, T., Gunn, J.E., Doi, M., Shimasaku, K., & Schneider, D.P. 1996, AJ, 111, 1748
Gilmore, G., Wyse, R.F.G. & Kuijken, K. 1989, Annual review of astronomy and astrophysics. Volume 27, pp. 555-627.
Gott, J. R. I., Jurić, M., Schlegel, D., Hoyle, F., Vogeley, M., Tegmark, M., Bahcall, N., & Brinkmann, J. 2005, ApJ, 624, 463
Gunn, J.E., Carr, M., Rockosi, C., et al. 1998, AJ, 116, 3040
Gunn, J.E., et al. 2005, AJ, submitted
Harris, W.E. 1996, AJ, 112, 1487
Hawley, S.L., Covey, K.R., Knapp, G.R., et al. 2002, AJ, 123, 3409
Helmi, A., Ivezić, Ž., Prada, F., et al. 2003, ApJ, 586, 195
Hogg, D.W., Finkbeiner, D.P., Schlegel, D.J. & Gunn, J.E. 2002, AJ, 122, 2129
Ibata, R. A., Irwin, M. J., Lewis, G. F., Ferguson, A. M. N., & Tanvir, N. 2003, MNRAS, 340, L21
Ivezić, Ž., Goldston, J., Finlator, K., et al. 2000, AJ, 120, 963
Ivezić, Ž., Tabachnik, S., Rafikov, R., et al. 2001, AJ, 122, 2749
Ivezić, Ž., Menou, K., Knapp, G.R., et al. 2002, AJ, 124, 2364
Ivezić, Ž., Lupton, R.H., Anderson, S., et al. 2003b, Proceedings of the Workshop *Variability with Wide Field Imagers*, Mem. Soc. Ast. It., 74, 978 (also astro-ph/0301400)
Ivezić, Ž., Lupton, R.H., Schlegel, D., et al. 2003c, Proceedings of "Satellites and Tidal Streams", May 26-30, 2003, La Palma, Spain (also astro-ph/0309075)
Ivezić, Ž., Lupton, R.H., Schlegel, D., et al. 2003d, Proceedings of "Milky Way Surveys: The Structure and Evolution of Our Galaxy", June 15-17, 2003, Boston (also astro-ph/0309074)
Ivezić, Ž., Lupton, R.H., Schlegel, D., et al. 2004, AN, 325, 583
Ivezić, Ž., Vivas, A.K., Lupton, R.H. & Zinn, R. 2005, AJ, 129, 1096
Jackson, T., Ivezić, Ž., & Knapp, G.R. 2002, MNRAS, 337, 749
Jurić, M., Ivezić, Ž., Lupton, R. H., et al. 2002, AJ, 124, 1776
Kaiser, N., Aussel, It., Burke, B.e., et al. 2002, in "Survey and Other Telescope Technologies and Discoveries", Tyson, J.A. & Wolff, S., eds. Proceedings of the SPIE, 4836, 154
Kleinman, S. J., Harris, H. C., Eisenstein, D. J., et al. 2004, ApJ, 607, 426
Larsen, J.A., & Humphreys, R.M. 2003, AJ, 125, 1958
Lenz, D.D., Newberg, J., Rosner, R., Richards, G.T., Stoughton, C. 1998, ApJS, 119, 121
Lupton, R.H., Gunn, J.E., & Szalay, A. 1999, AJ, 118, 1406
Lupton, R.H., Ivezić, Ž., Gunn, J.E., Knapp, G.R., Strauss, M.A. & Yasuda, N. 2003, in "Survey and Other Telescope Technologies and Discoveries", Tyson, J.A. & Wolff, S., eds. Proceedings of the SPIE, 4836, 350
Lupton, R. 2005, AJ, submitted
Maíz-Apellániz, J. 2001, AJ, 121, 2737
Majewski, S.R., Skrutskie, M.F., Weinberg, M.D. & Ostheimer, J.C. 2003, ApJ, 599, 1082
Martínez-Delgado, D., Alonso-García, J., Aparicio, A., & Gómez-Flechoso, M. A. 2001, ApJ, 549, L63
Martínez-Delgado, D., Gómez-Flechoso, M. Á., Aparicio, A., & Carrera, R. 2004, ApJ, 601, 242
Munn, J.A., *et al.* 2004, AJ, 127, 3034
Newberg, H. J., Yanny, B., Rockosi, C., et al. 2002, ApJ, 569, 245
Newberg, H. J., & Sloan Digital Sky Survey Collaboration 2003, American Astronomical Society Meeting Abstracts, 203,
Newberg, H.J. & Yanny, B. 2005, to appear in ASP conference Series, "Astrometry in the Age of the Next Generation of Large Telescopes", eds. A. Monet and K. Seidelmann, also astro-ph/0502386
Oke, J.B., & Gunn, J.E. 1983, ApJ, 266, 713
Parker, J.E., Humphreys, R.M., & Larsen, J.A., 2003, AJ, 126, 1346
Parker, J.E., Humphreys, R.M., & Beers, T.C. 2004, AJ, 127, 1567
Peiris, H. 2000, ApJ, 544, 811
Peñarrubia, J., Martínez-Delgado, D., Rix, H. W., et al. 2005, ApJ, 626, 128
Pier, J.R., Munn, J.A., Hindsley, R.B., Hennesy, G.S., Kent, S.M., Lupton, R.H. & Ivezić, Ž. 2003, AJ, 125, 1559
Reid, N. & Majewski, S.R. 1993, ApJ 409, 635
Reid, M. J. 1993, ARA&A, 31, 345
Reid, I. N., Gizis, J. E., & Hawley, S. L. 2002, AJ, 124, 2721
Richards, G. T., Fan, X., Schneider, D. P., et al. 2001, AJ, 121, 2308
Schlegel, D., Finkbeiner,D.P. & Davis, M. 1998, ApJ500, 525
Spitzer, L. J. 1942, ApJ, 95, 329
Rocha-Pinto, H.J., Majewski, S.R., Skrutskie, M.F. & Crane, J.D. 2003, ApJ, 594, L115
Searle, L., & Zinn, R. 1978, ApJ, 225, 357
Sesar, B., Svilković, D., Ivezić, Ž., et al. 2005, submitted to AJ (also astro-ph/0403319)
Seth, A.C., Dalcanton, J.J. & de Jong, R.S., 2005, in *Resolved Stellar Populations*, ASP Conference Series, eds. D. Valls-Gabaud & M. Chavez, in press (also astro-ph/0506429)
Siegel, M.H., Majewski, S.R., Reid, I.N., & Thompson, I.B. 2002, ApJ, 578, 151
Smith, J.A., Tucker, D.L., Kent, S.M., et al. 2002, AJ, 123, 2121
Smolčić, V., Ivezić, Ž., Knapp, G.R., et al. 2004, ApJ, 615, L141
Stoughton, C., Lupton, R.H., Bernardi, M., et al. 2002, AJ, 123, 485
Teerikorpi, P. 1997, ARA&A, 35, 101
Tucker, D., et al. 2005, AJ, submitted (MT Pipeline)
Tyson, J.A. 2002, in *Survey and Other Telescope Technologies and Discoveries*, Tyson, J.A. & Wolff, S., eds. Proceedings of the SPIE, 4836, 10
Vivas, A.K., Zinn, R., Andrews, P., *et al.* 2001, ApJ, 554, L33
Wilkinson, M. I., Vallenari, A., Turon, C., et al. 2005, MNRAS, 359, 1306
Yanny, B., Newberg, H. J., Kent, S., et al. 2000, ApJ, 540, 825
York, D.G., Adelman, J., Anderson, S., et al. 2000, AJ, 120, 1579
Zinn, R., Vivas, A.K., Gallart, C., & Winnick, R. 2003, astro-ph/0309827
Williams, C. C., et al. 2002, Bulletin of the American Astronomical Society, 34, 1292

N_{app}	$N(r<22)$	$N(r<21.5)$
1	30543044	2418472
2	11958311	1072235
3	3779424	3471972
4	856639	785711
5	220577	199842
6	105481	93950
7	141017	132525
8	43943	40065
9	59037	57076
10	15616	15002
11	1522	1273
12	2012	1772
13	2563	2376
14	1776	1644
15	1864	1741
16	3719	3653
17	1281	1253
N_{stars}	47737826	39716935
N_{obs}	73194731	62858036

TABLE 1

Repeat observations in the stellar sample: Because of partial imaging scan overlaps and the convergence of scans near the survey poles, a significant fraction of observations are repeated observations of the same stars. In columns $N(r<22)$ and $N(r<21.5)$ we show the number of stars observed N_{app} times for stars with average magnitudes less than $r=22$ and $r=21.5$, respectively. The final two rows list the total number of stars in the samples, and the total number of observations.

	ri_0 - ri_1	$<gr>$	$<M_r>$	SpT	dx [pc]	D_{min} [pc]	D_{max} [pc]	N_{stars}
1	0.10 - 0.15	0.36	5.33	∼F9	500	961	15438	4232426
2	0.15 - 0.20	0.48	5.77	F9-G6	400	773	12656	3842970
3	0.20 - 0.25	0.62	6.18	G6-G9	400	634	10555	2780382
4	0.25 - 0.30	0.75	6.56	G9-K2	300	529	8939	1950374
5	0.30 - 0.35	0.88	6.91	K2-K3	200	448	7676	1527679
6	0.35 - 0.40	1.00	7.23	K3-K4	200	384	6673	1308590
7	0.40 - 0.45	1.10	7.52	K4-K5	200	334	5864	1178986
8	0.45 - 0.50	1.18	7.79	K5-K6	150	293	5202	1088285
0	0.50 - 0.55	1.25	8.04	K6	150	260	4653	1009596
10	0.55 - 0.60	1.30	8.27	K6-K7	150	233	4191	933843
11	0.60 - 0.65	1.33	8.49	K7	100	210	3798	858864
12	0.65 - 0.70	1.36	8.70	K7	100	190	3458	804603
13	0.70 - 0.80	1.38	9.00	K7-M0	100	173	2897	1433278
14	0.80 - 0.90	1.39	9.37	M0-M1	60	145	2450	1367152
15	0.90 - 1.00	1.39	9.73	M1	50	122	2079	1341331
16	1.00 - 1.10	1.39	10.09	M1-M2	50	104	1764	1323791
17	1.10 - 1.20	1.39	10.45	M2-M3	40	88	1493	1266917
18	1.20 - 1.30	1.39	10.81	M3	30	74	1258	1129342
19	1.30 - 1.40	1.39	11.18	M3	25	63	1056	892709

TABLE 2

The number density map parameters. Each of the 19 maps is a volume limited three-dimensional density map of stars with $ri_0 < r-i < ri_1$, corresponding to MK spectral types listed in SpT column, with mean $g-r$ color and absolute magnitude M_r listed in $<gr>$ and $<M_r>$ columns, respectively. The minimum and maximum distance, D_{min} and D_{max}, are the color-dependent distance limits which define a volume limited sample for each $r-i$ color bin. The density maps are constructed by binning and counting the observed stars in dx large cubical pixels, and by dividing the count by the observed volume of the pixel. The total number of stars in each map is listed in N_{stars} column.

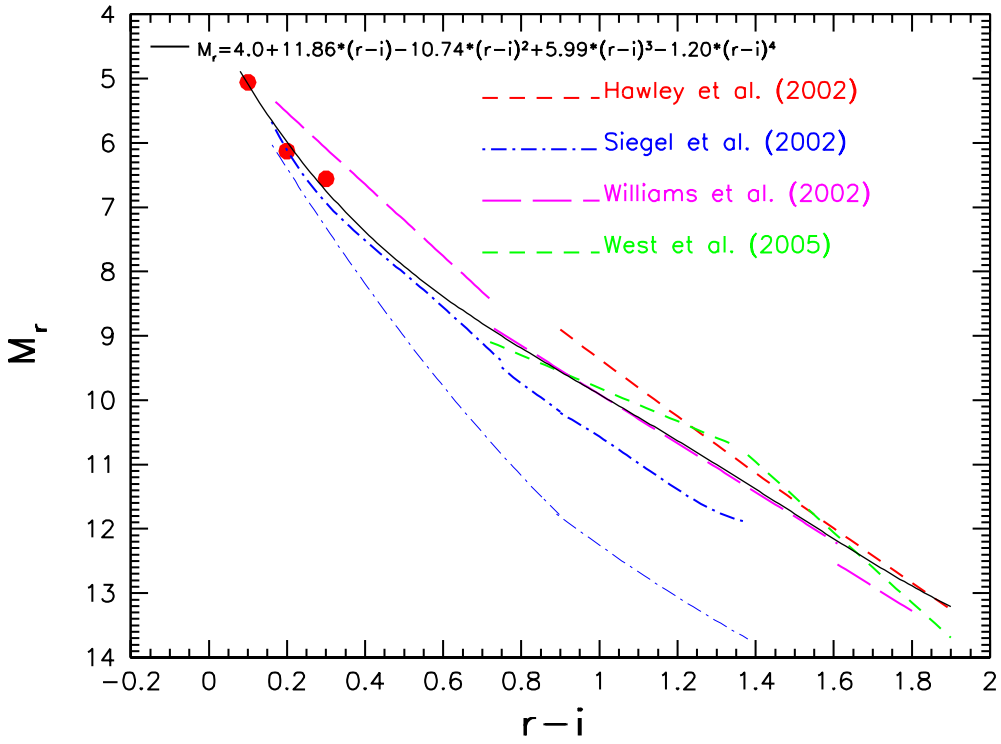

FIG. 1.— The solid line shows the photometric parallax relation adopted in this work. Other lines show photometric parallax relations from the literature, as marked. The lower (thin) curve from Siegel et al. corresponds to low metallicity stars. The large symbols show a normalization based on the SDSS observations of globular cluster M13.

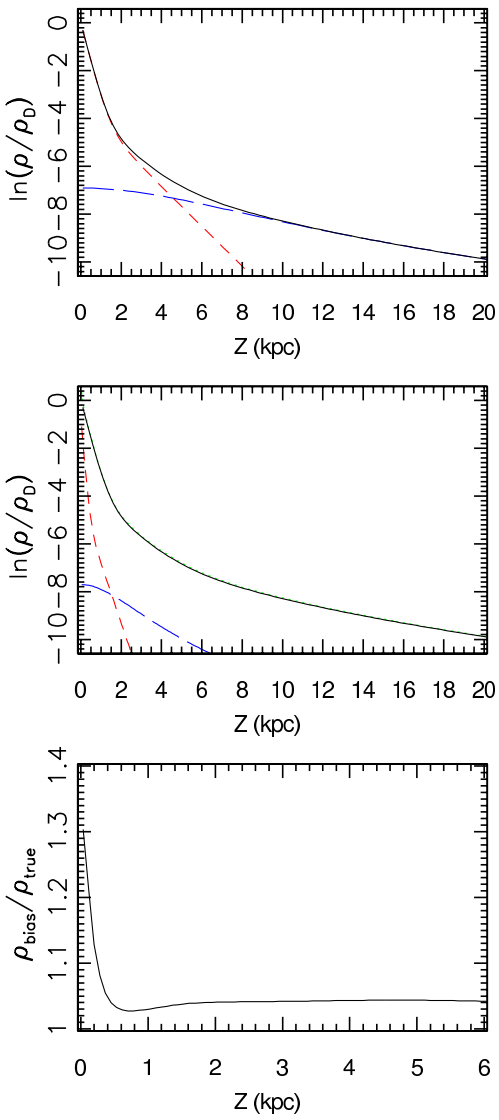

FIG. 2.— An illustration of the effects of misidentifying giants as main sequence stars. The top panel shows the Z dependence of stellar density at R=8 kpc for a fiducial model consisting of two disks with scale heights of 300 pc and 1200 pc. The contribution of the disks is shown by the short-dashed line, and the long-dashed line shows the contribution of a power-law spherical halo with the power-law index of 3. The middle panel shows the contribution of misidentified giants from disks (short-dashed) and halo (long-dashed) for an assumed giant fraction of 5%, and underestimated distances by a factor of 3. The "contaminated" model is shown by dotted line, just above the solid line, which is the same as the solid line in the top panel. The ratio of the "contaminated" and true density is shown in the bottom panel (note the different horizontal scale).

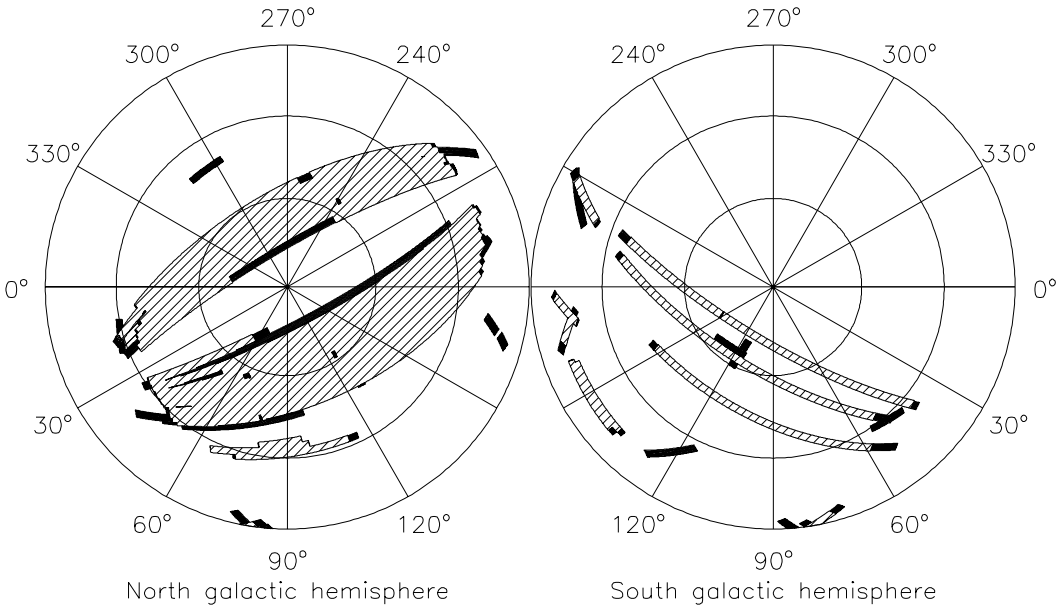

FIG. 3.— Footprint on the sky of SDSS observations used in this work shown in Lambert equal area projection (hatched region). The circles represent contours of constant galactic latitude, with the straight lines showing the location of constant galactic longitude. For this study, observations from 248 SDSS imaging runs were used, stretching over the course of 5 years. We cover 5450 deg^2 of the north Galactic hemisphere, and a smaller but more frequently sampled area of 1088 deg^2 in the southern Galactic hemisphere.

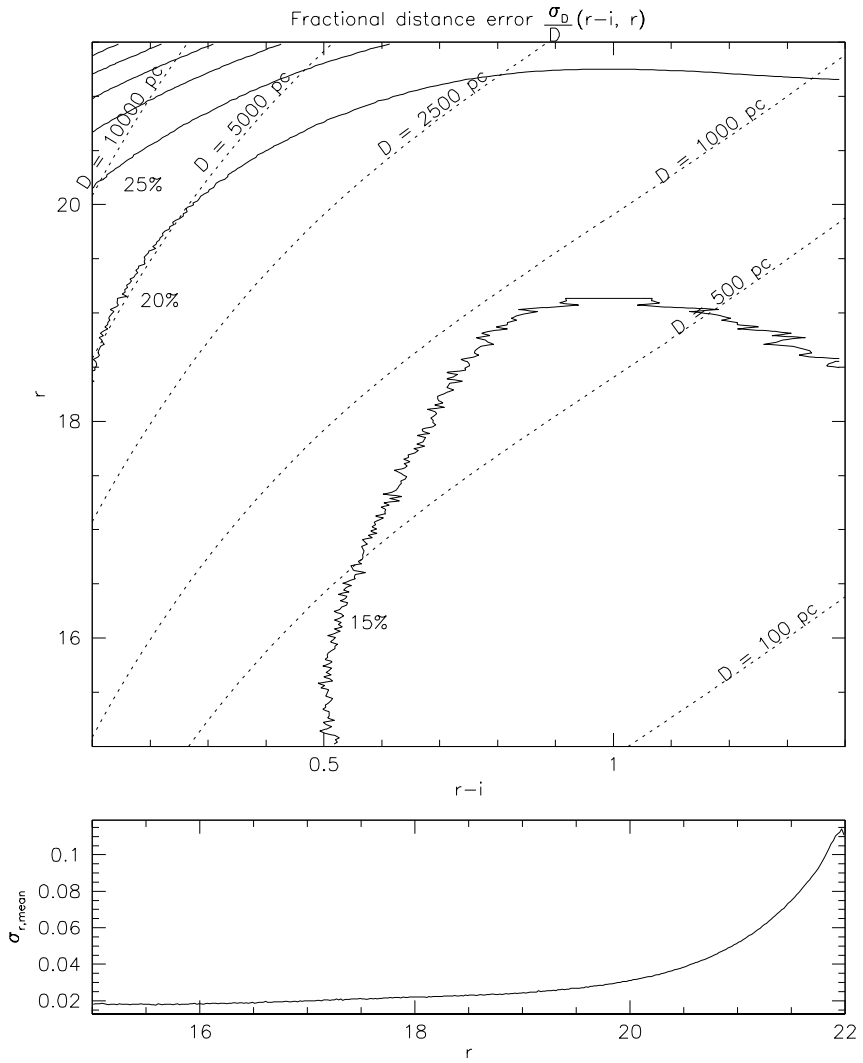

FIG. 4.— The top panel shows the mean fractional distance error as a function of the $r - i$ color and r band magnitude, assuming the intrinsic photometric parallax relation scatter of $\sigma_{M_{r,i}} = 0.3$ mag. The solid lines are contours of constant fractional distance error, starting with $\sigma_D/D = 15\%$ (lower right) and increasing in increments of 5% towards the top left corner. The dotted lines are contours of constant distance, and can be used to quickly estimate the distance errors for an arbitrary combination of color and magnitude/distance. Note that fractional distance errors are typically smaller than $\sim 20\%$.

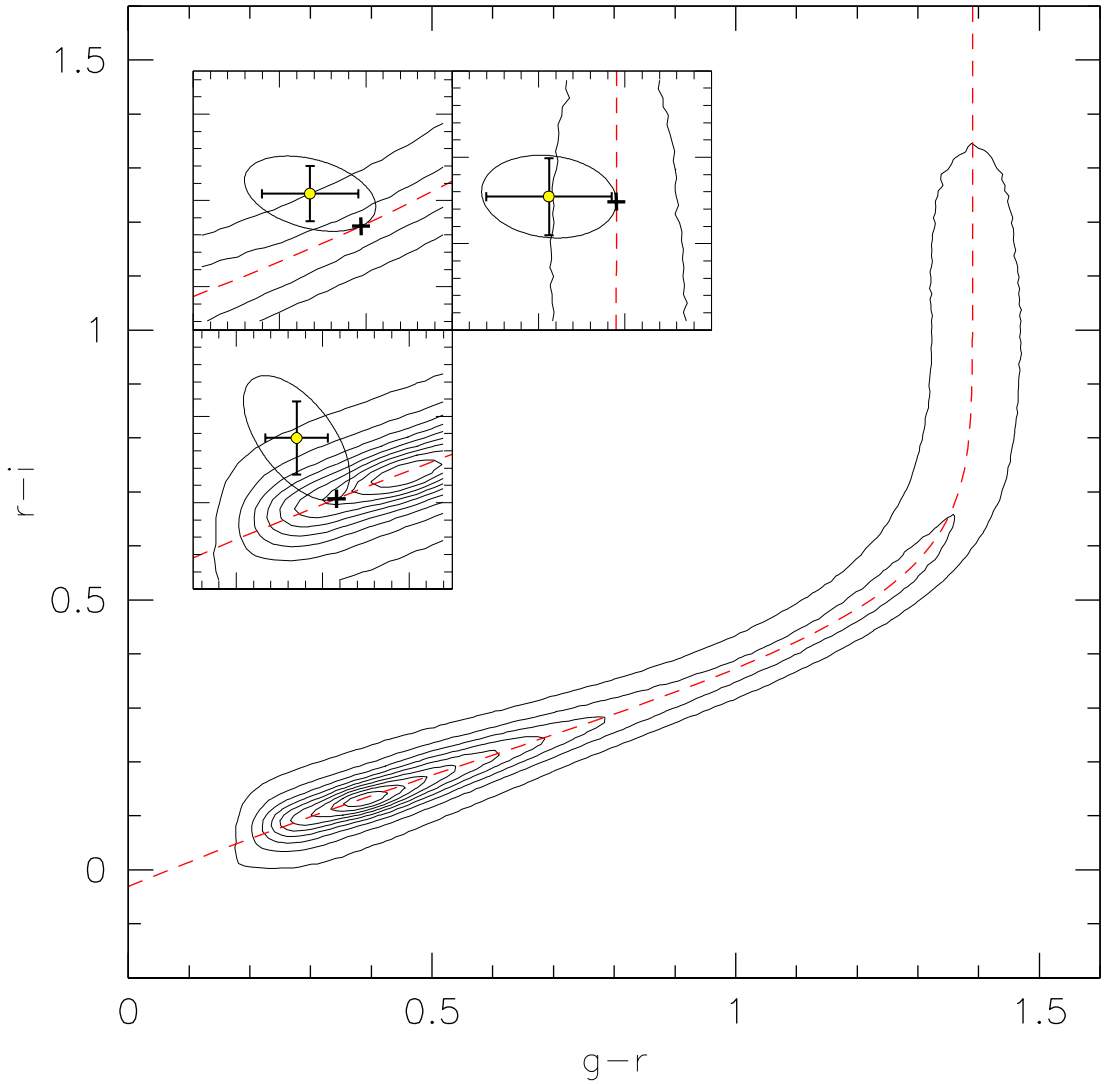

FIG. 5.— The distribution of ∼48 million stars analyzed in this work in the $r-i$ vs. $g-r$ color-color diagram, shown by isodensity contours. Most stars lie on a narrow locus, shown by the dashed line, whose width at the bright end is 0.02 mag for blue stars ($g-r \lesssim 1$) and 0.06 mag for red stars ($g-r \sim 1.4$). The inserts illustrate the maximum likelihood method used to improve color estimates: the ellipses show measurement errors, and the crosses are the color estimates obtained by requiring that a star lies exactly on the stellar locus. Note that the principal axes of the error ellipses are not aligned with the axes of the color-color diagram because both colors include the r band magnitude.

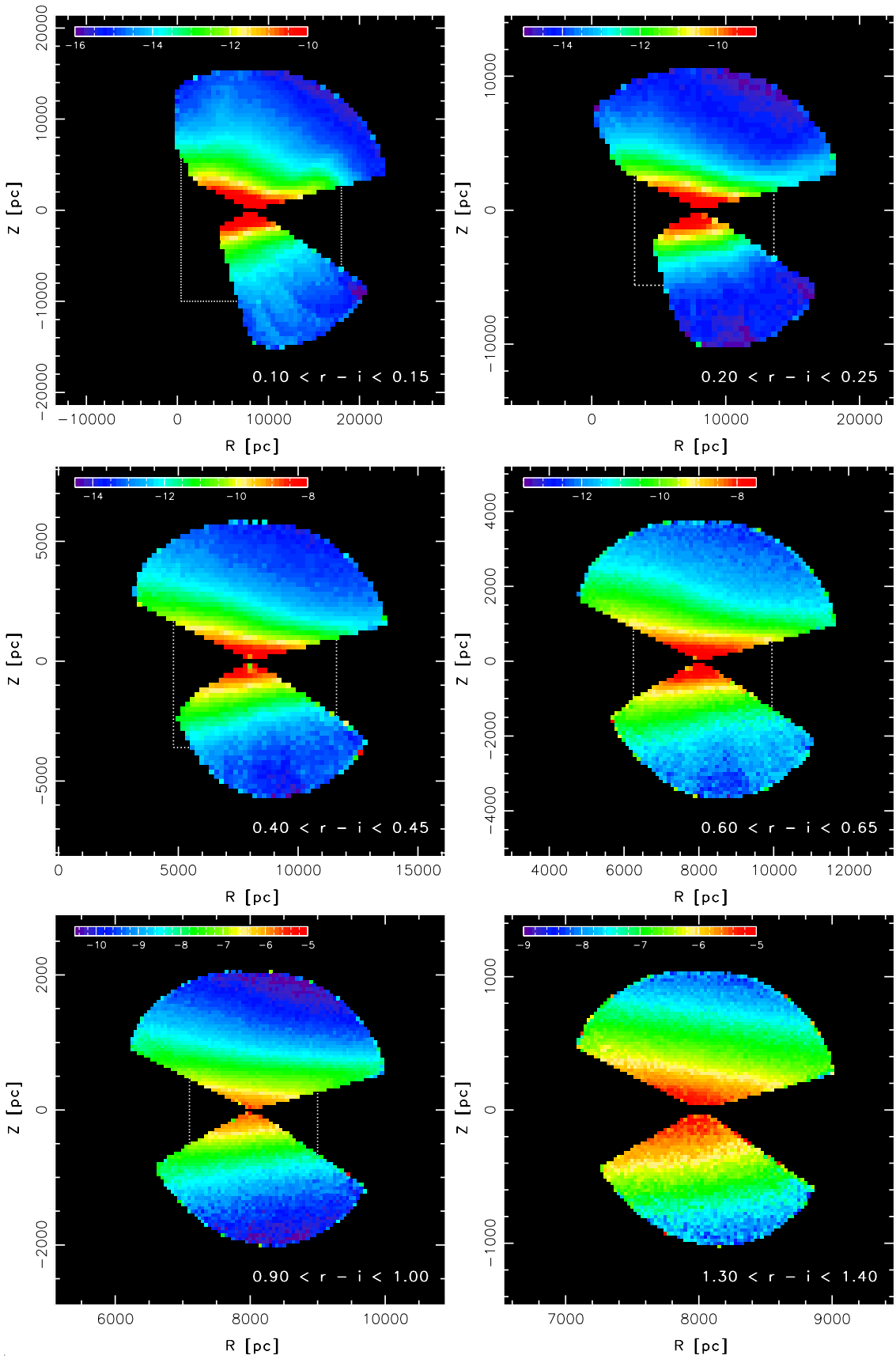

FIG. 6.— The stellar number density as a function of Galactic cylindrical coordinates R (distance from the axis of symmetry) and Z (distance from the plane), for different $r-i$ color bins, as marked in each panel. Each pixel value is the median for all polar angles. The density is shown on a logarithmic scale, and coded from blue to red (black pixels are regions without the data). Note that the distance scale greatly varies from the top left to the bottom right panel – the size of the the bottom right panel is roughly equal to the size of four pixels in the top left panel. Each white dotted rectangle denotes the bounding box of region containing the data on the following panel.

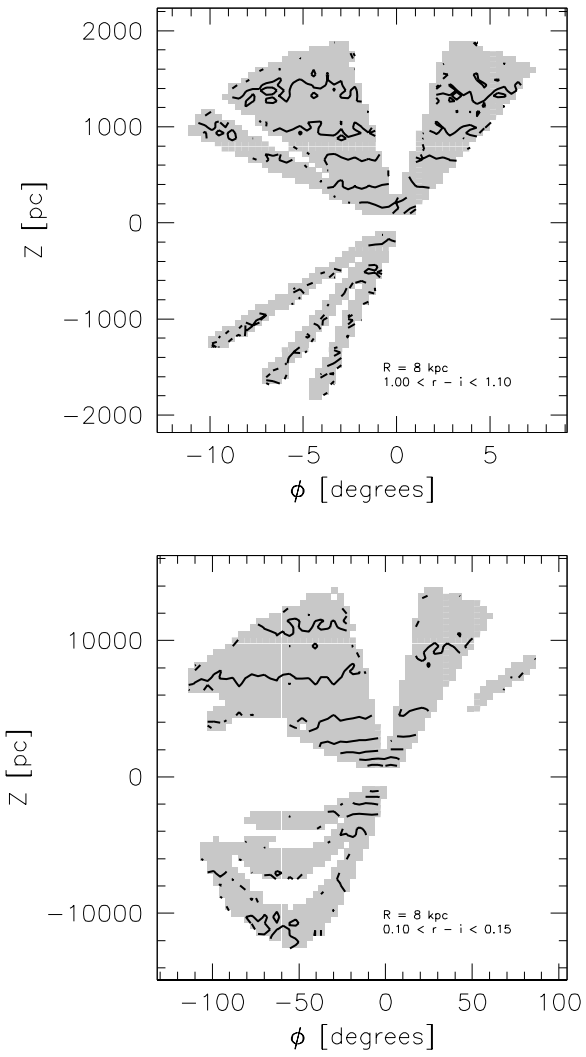

FIG. 7.— The azimuthal dependence of the number density for $R = R_{\odot}$ kpc cylinder around the Galactic center. The shaded region is the area covered by the SDSS survey, and the lines show constant density contours for two color bins ($1.0 < r - i < 1.1$ in the top panel and $0.10 < r - i < 0.15$ in the bottom panel). The fact that isodensity contours are approximately horizontal supports the assumption that the stellar number density distribution is circularly symmetric around the Galactic center, and at the same time indicates that the assumed photometric parallax distribution is not grossly incorrect. Nevertheless, note that deviations from circular symmetry do exist, e.g. at $Z \sim$10,000 and $\phi \sim 40°$ in the bottom panel.

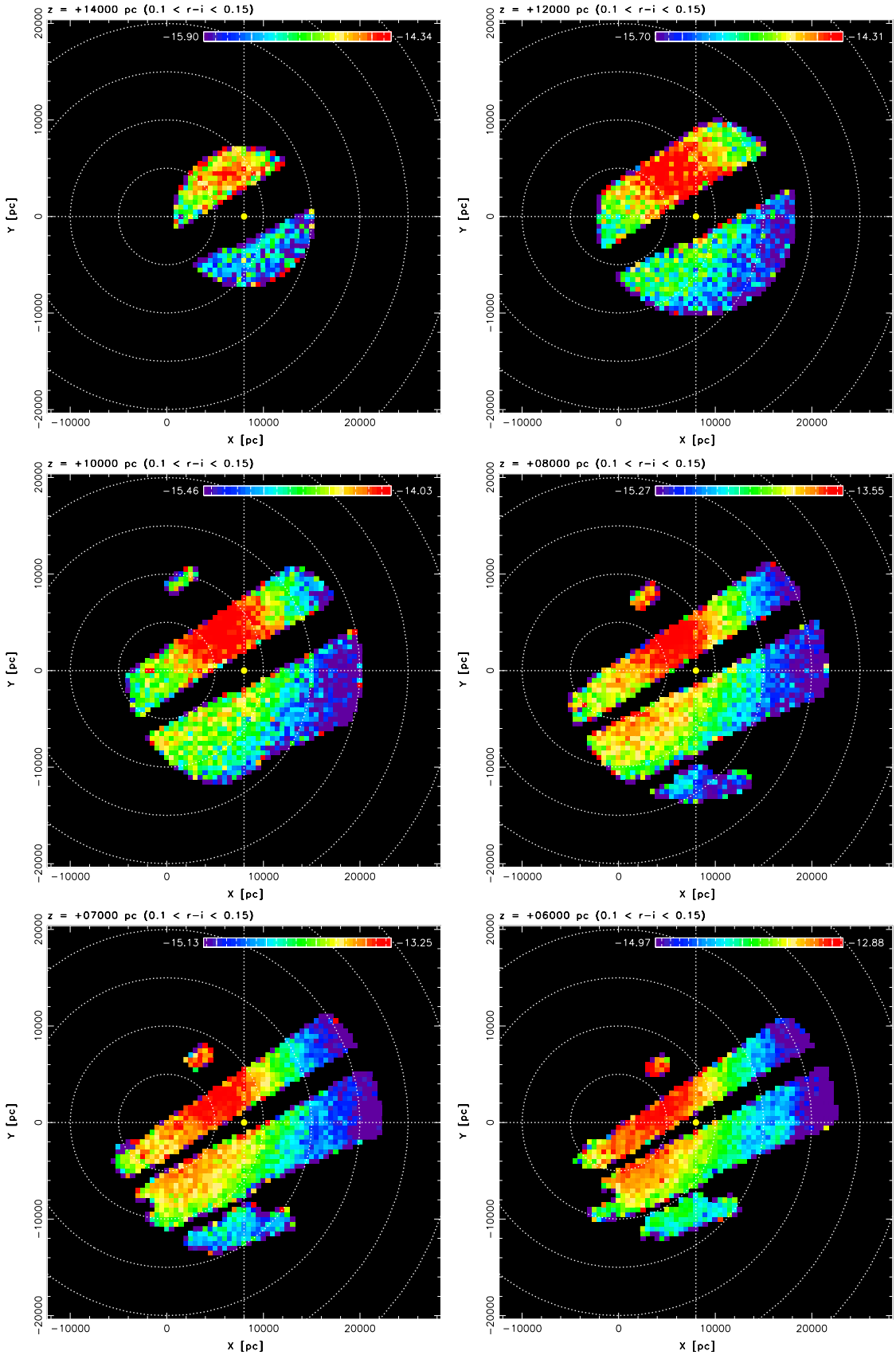

FIG. 8.— The stellar number density for the same color bin as in the top left panel in Fig. 6 ($0.10 < r - i < 0.15$), shown here for cross-sections parallel to the Galactic plane, as a function of the distance from the plane. The distance from the plane varies from 16 kpc (top left) to 6 kpc (bottom right), in steps of 2 kpc. The circles visualize presumed axial symmetry of the Galaxy, and the origin marks our position (the Galactic center is at $x = -8$ kpc and $y = 0$). Note the strong asymmetry with respect to the $y = 0$ line.

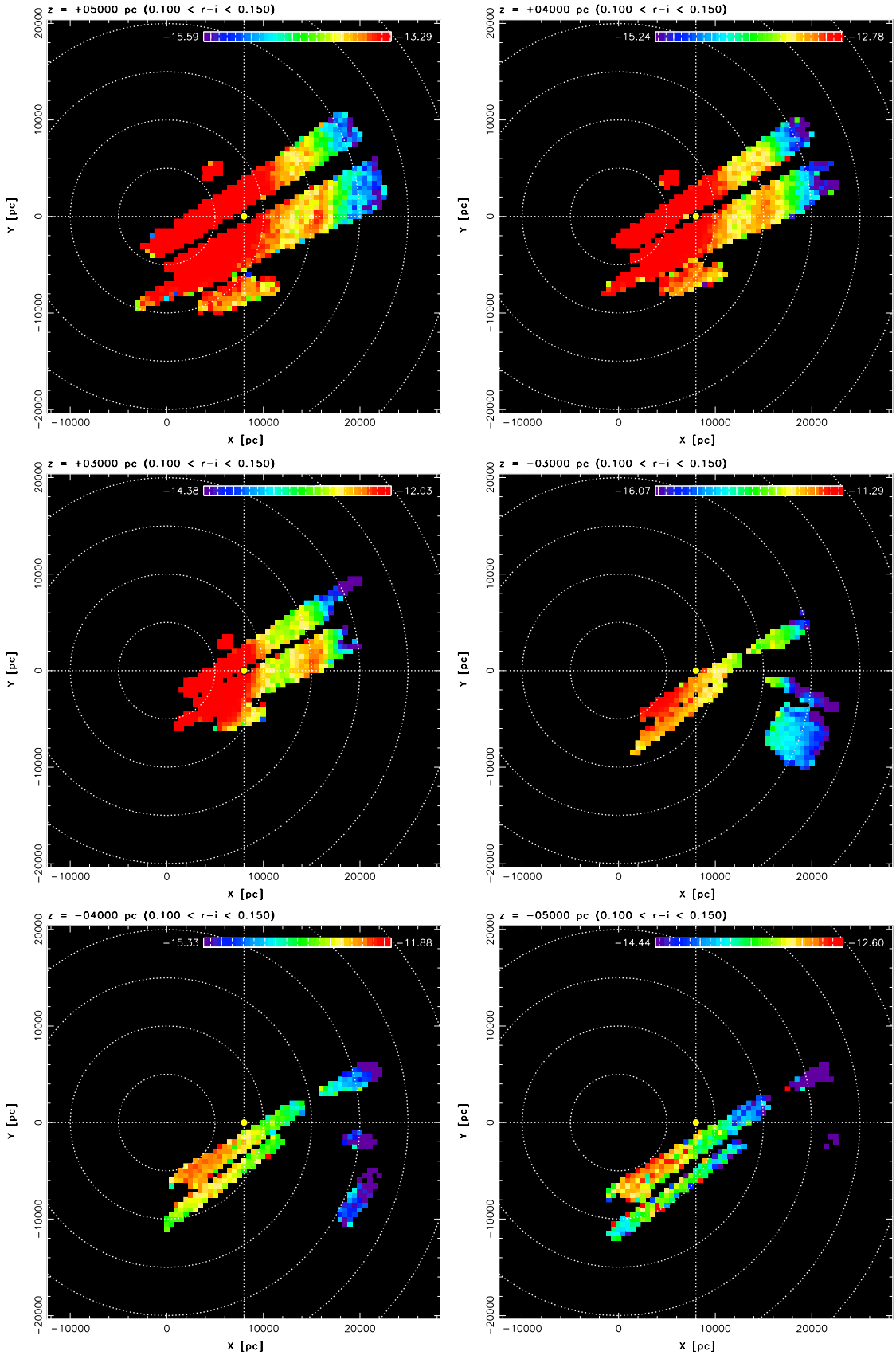

FIG. 9.— Analogous to Fig. 8, except that three symmetric slices at z=3, 4 and 5 kpc above and below the plane are shown. The color stretch in panels for z=3, 4 and 5 kpc is optimized to bring out the Monoceros overdensity at $R \sim 16$ kpc and $y \sim 0$.

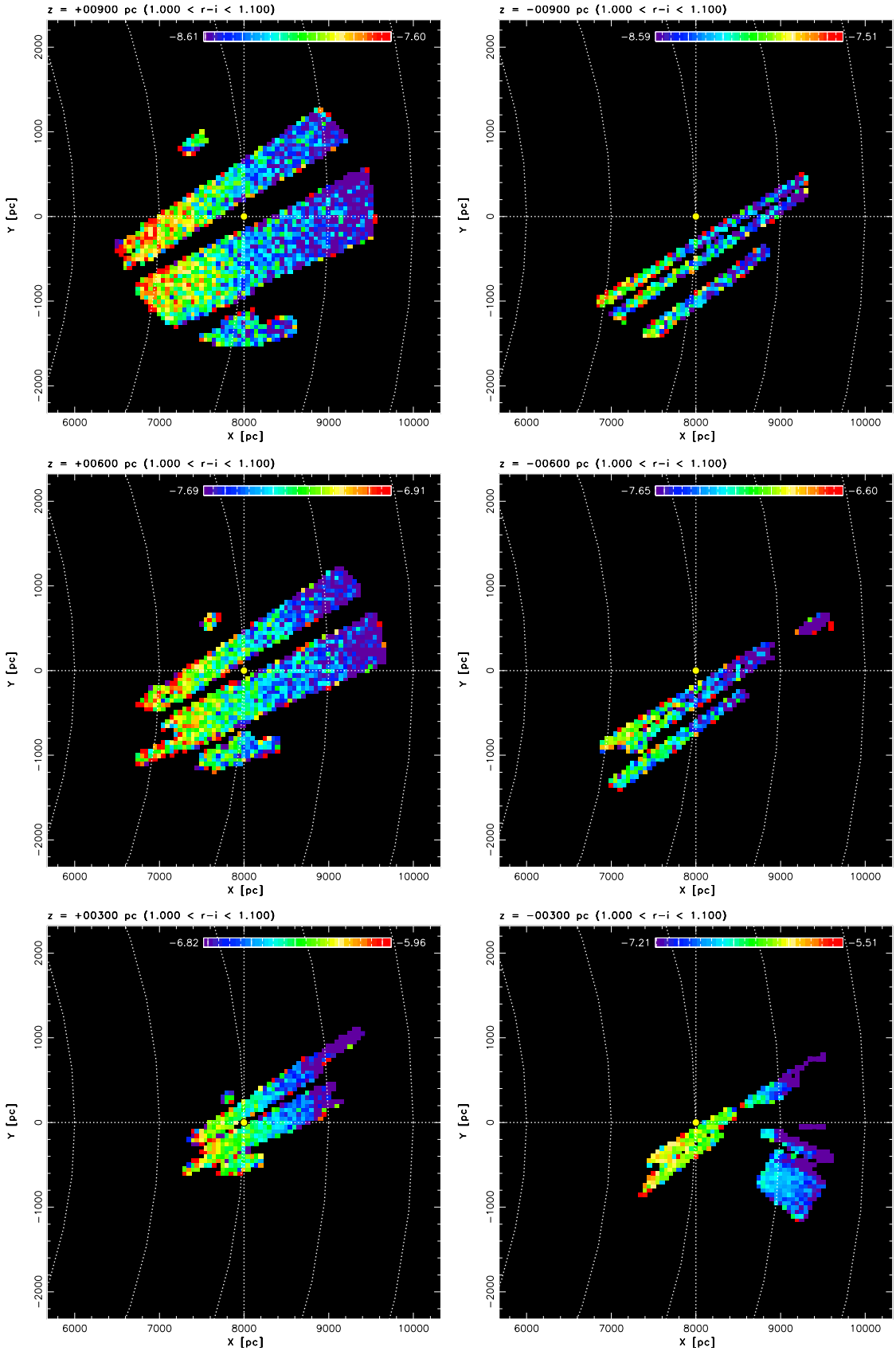

FIG. 10.— Analogous to Fig. 8, except that here three symmetric slices at z=300, 600 and 900 pc above and below the plane are shown, for the $1.00 < r - i < 1.10$ color bin. Note that at these distance scales there are no obvious discernible substructures in the density distribution.

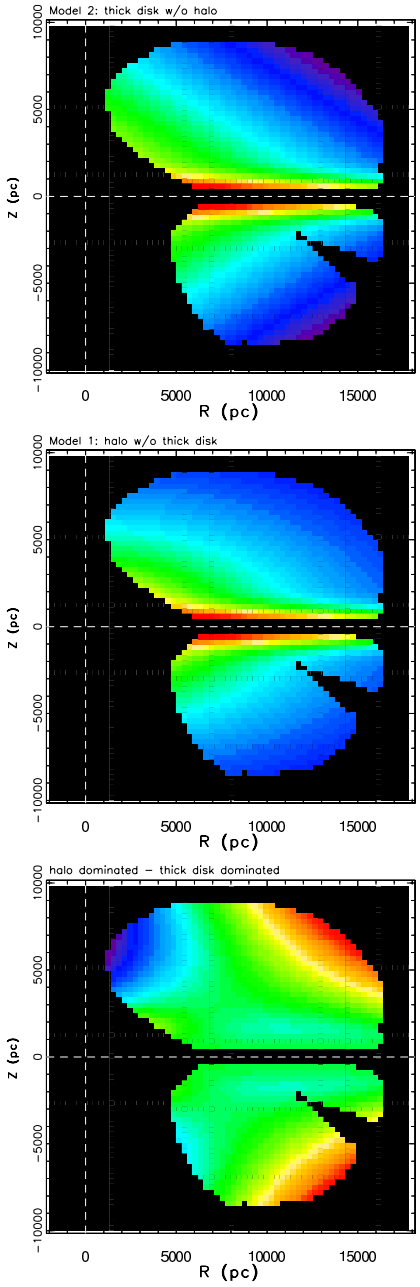

FIG. 11.— An illustration of the degeneracies in fitting models for stellar distribution. The top panel shows a thin disk plus thick disk model, without any contribution from the halo (volume density on a logarithmic stretch, from blue to red, shown only for the regions with SDSS data), and the middle panel shows a single think disk plus an oblate halo model. Both models are fine-tuned to produce nearly identical counts for $R = 8$ kpc and $|Z| < 8$ kpc. The bottom panel shows the difference between the two models (logarithmic stretch for $\pm$ a factor of 3, from blue to red, the zero level corresponds to green color). The models are distinguishable only at $|Z| > 3$ kpc and R significantly different from 8 kpc.

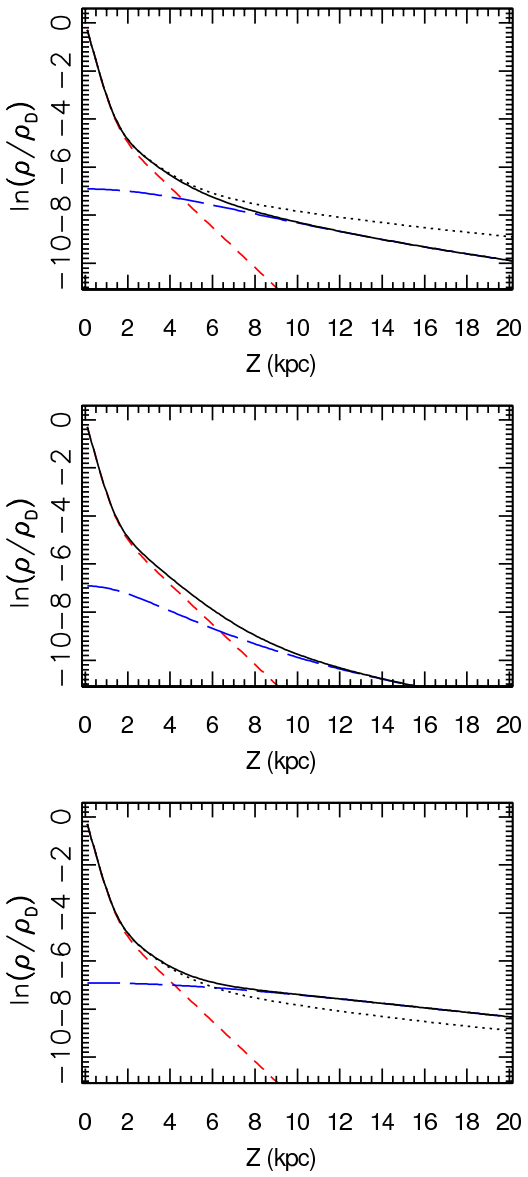

FIG. 12.— An illustration of the halo effects on the interpretation of stellar distribution. The solid line in the top panel shows the Z dependence of stellar density at R=8 kpc, for a model consisting of two disks with scale heights of 300 pc and 1200 pc (the disks contribution is shown by the short-dashed line), and a power-law spherical halo with power-law index of 3 (long-dashed line). The dotted line shows a similar model with the halo power-law index changed to 2. The middle panel shows a model with an oblate (q_H=0.5) halo (all other parameters are kept fixed), and the bottom panel shows a model with a prolate (q_H=2) halo. The dotted line in the bottom panel is the same as the dotted line in the top panel. As evident, for a given line of sight, the model degeneracies are strong.

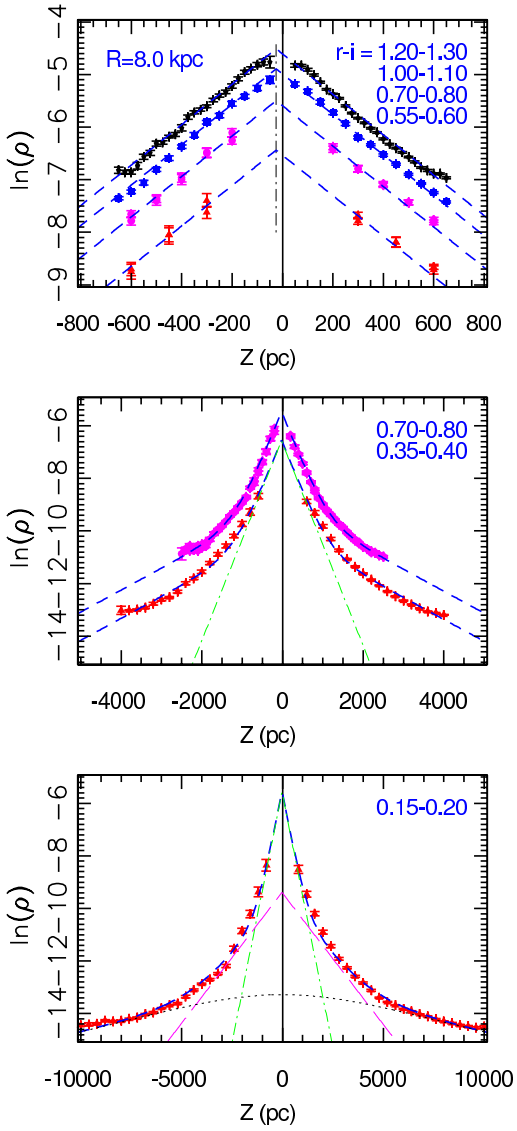

FIG. 13.— The vertical (Z) distribution of SDSS stellar counts for $R = 8$ kpc, and different $r - i$ color bins, as marked. The lines are best-fit models to measured distribution (uncorrected for Malmquist bias). The dashed lines in the top panel correspond to a disk with a scale height of 270 pc. The vertical dot-dashed line marks the position of the density maximum, and implies a Solar offset from the Galactic plane of 24±5 pc. The dashed lines in the middle panel correspond to a sum of two disks with scale heights of 270 pc and 1400 pc, and the relative normalization of 0.04. The dot-dashed line is the contribution of the 270 pc disk for the bluer color bin. Note that the 1400 pc disk becomes important for $|Z| > 1000$ pc. The dashed line in the bottom panel (closely following the data points) corresponds to a sum of two disks (with scale heights of 260 pc and 1000 pc, and the relative normalization of 0.022), and a power-law spherical halo with power-law index of 3, and a relative normalization with respect to the 260 pc disk of 4.5×10^{-4}. The dot-dashed line is the contribution of the 260 pc disk, the long-dashed line is the contribution of the 1000 pc disk, and the halo contribution is shown by the dotted line. Disk parameters of the bottom panel are different from the top two panels, because of the different populations of stars under consideration (G dwarfs vs. M dwarfs, in the bottom and top panels, respectively).

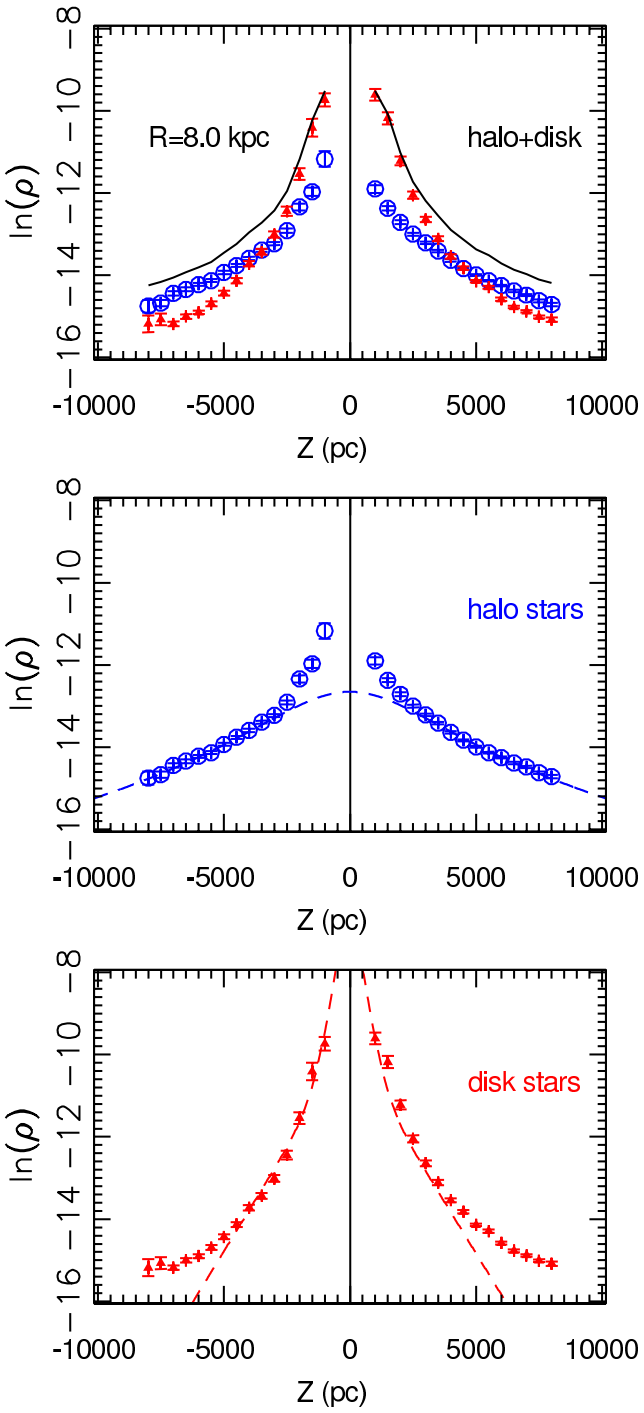

FIG. 14.— The vertical (Z) distribution of SDSS stellar counts for $R = 8$ kpc, and $0.10 < r - i < 0.15$ color bin. Stars are separated by their $u - g$ color, which is a proxy for metallicity, into a sample representative of the halo stars (low metallicity, $0.60 < u - g < 0.95$, circles) and a sample representative of the disk stars (high metallicity, $0.95 < u - g < 1.15$, triangles). The line in the top panel shows the sum of the counts for both subsamples. The counts for each subsample are shown separately in the middle and bottom panels, and compared to the best fit models, shown as lines. Note that the disk stars are more concentrated towards the Galactic plane. Due to a simple $u - g$ cut, both samples are expected to suffer from contamination: close to the Galactic plane ($|Z| < 2$ kpc) the halo sample is contaminated by the disk stars, while further away from the plane ($|Z| > 5$ kpc) the disk sample is contaminated by halo stars.

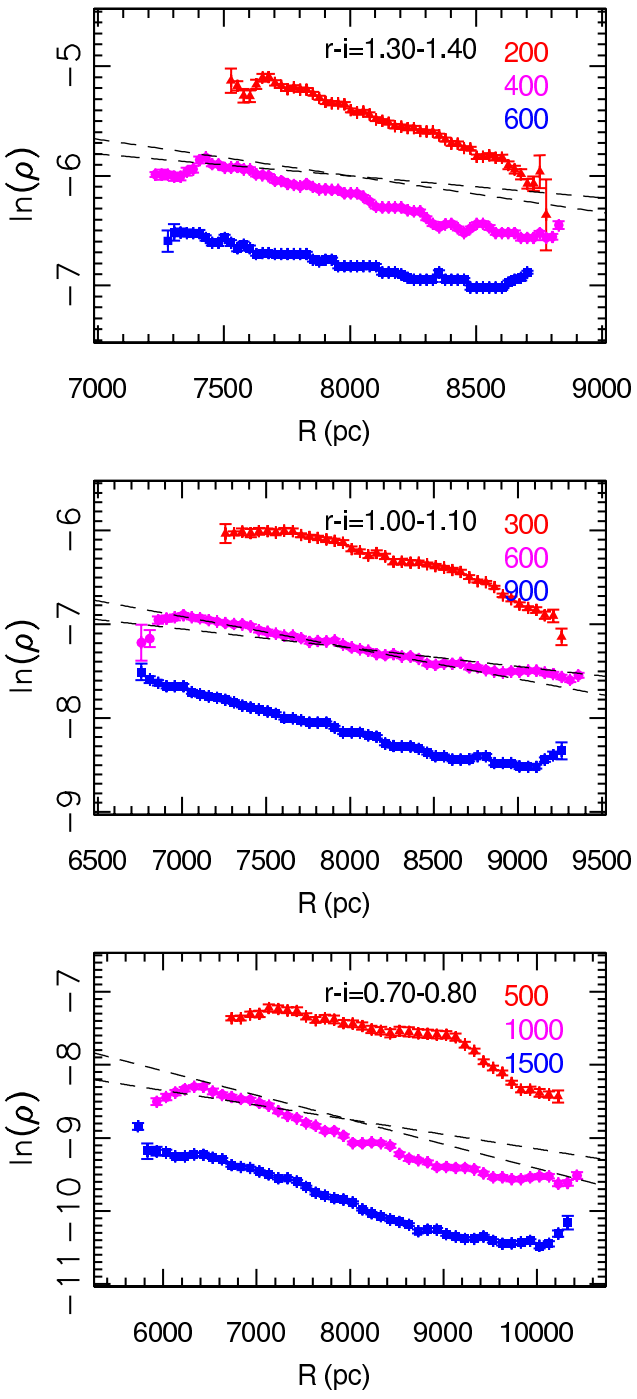

FIG. 15.— The radial distribution of SDSS stellar counts for different $r-i$ color bins, and at different heights above the plane, as marked in each panel (pc). The two dashed lines show the exponential radial dependence of density for scale lengths of 3000 and 5000 pc (with arbitrary normalization).

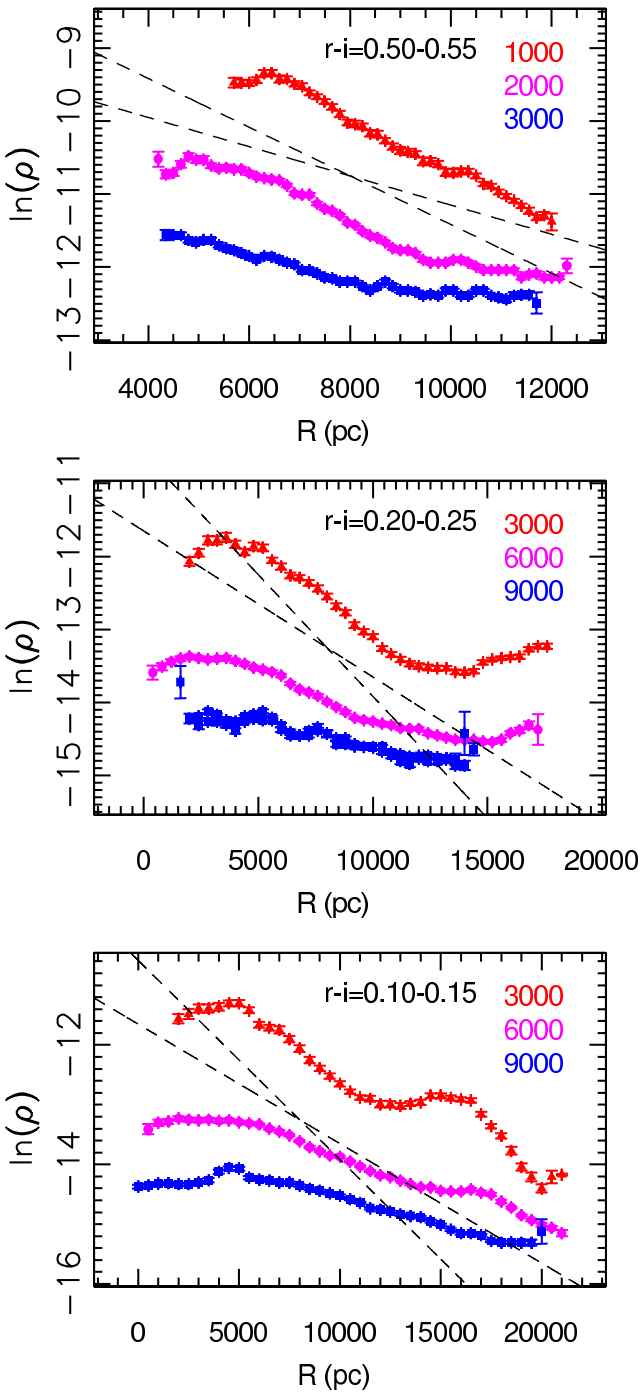

FIG. 16.— Analogous to Fig. 15, except for bluer color bins, which probe larger distances.

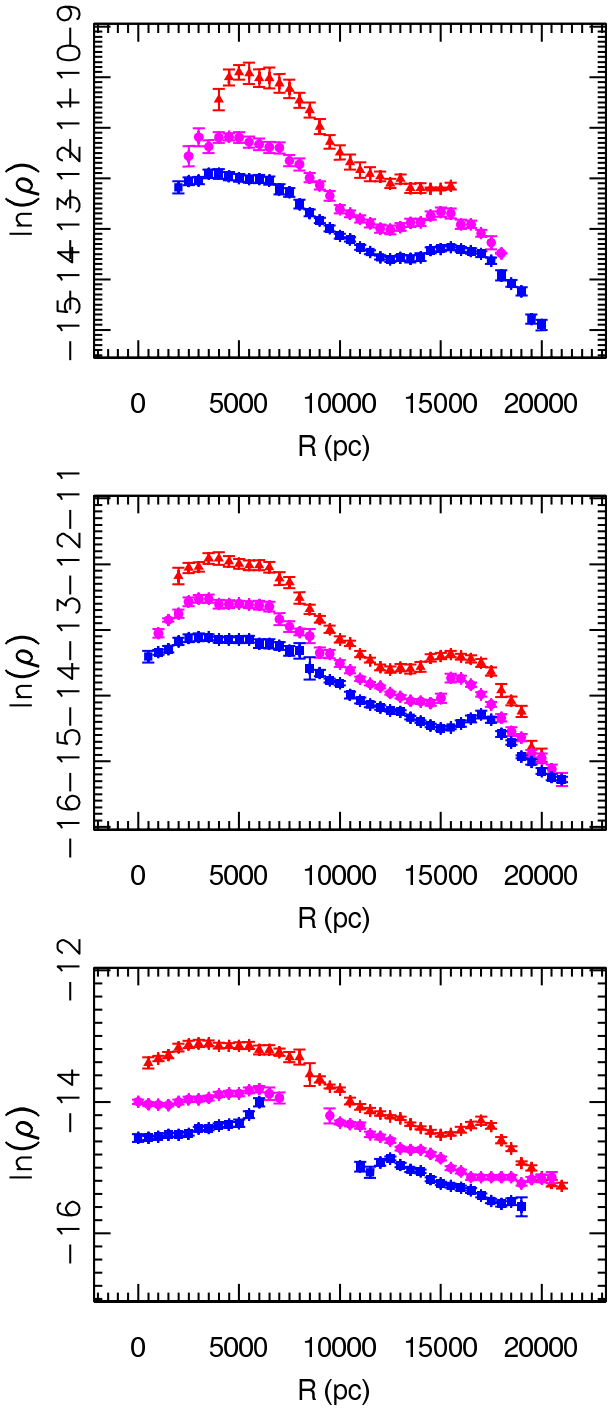

FIG. 17.— The radial distribution of SDSS stellar counts for $0.10 < r - i < 0.15$ color bin, with the data restricted to $|y| < 1$ kpc. The selected heights are, from top to bottom, (2,3,4), (4,5,6) and (6,8,10) kpc. The Monoceros stream at is easily visible as local maxima at $R = 16 - 17$ kpc, and the Virgo overdensity as the wide bump at $R \sim 6$ kpc.

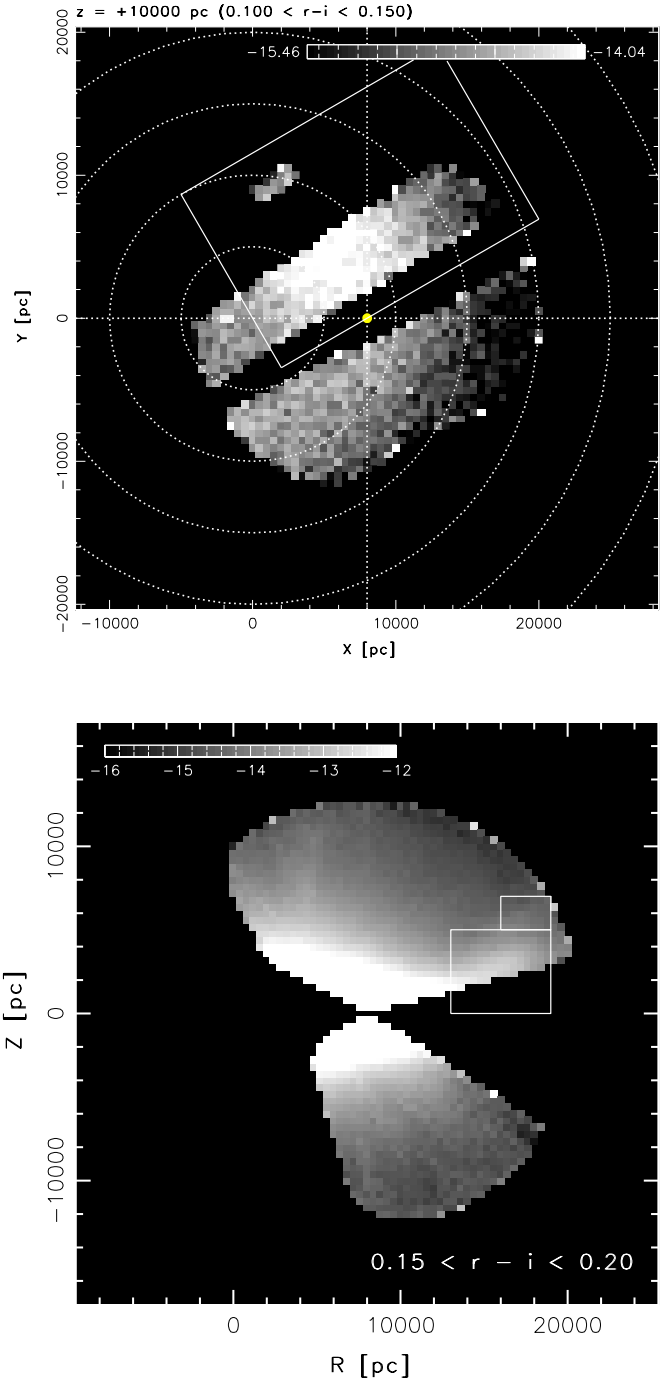

FIG. 18.— The regions excluded from global Galactic model fits. The pixels within the rectangle in the top panel are excluded to avoid contamination by the Virgo overdensity. In the bottom panel, the pixels enclosed by the polygon at $R \sim 16$ kpc are excluded to avoid the contamination by the Monoceros stream.

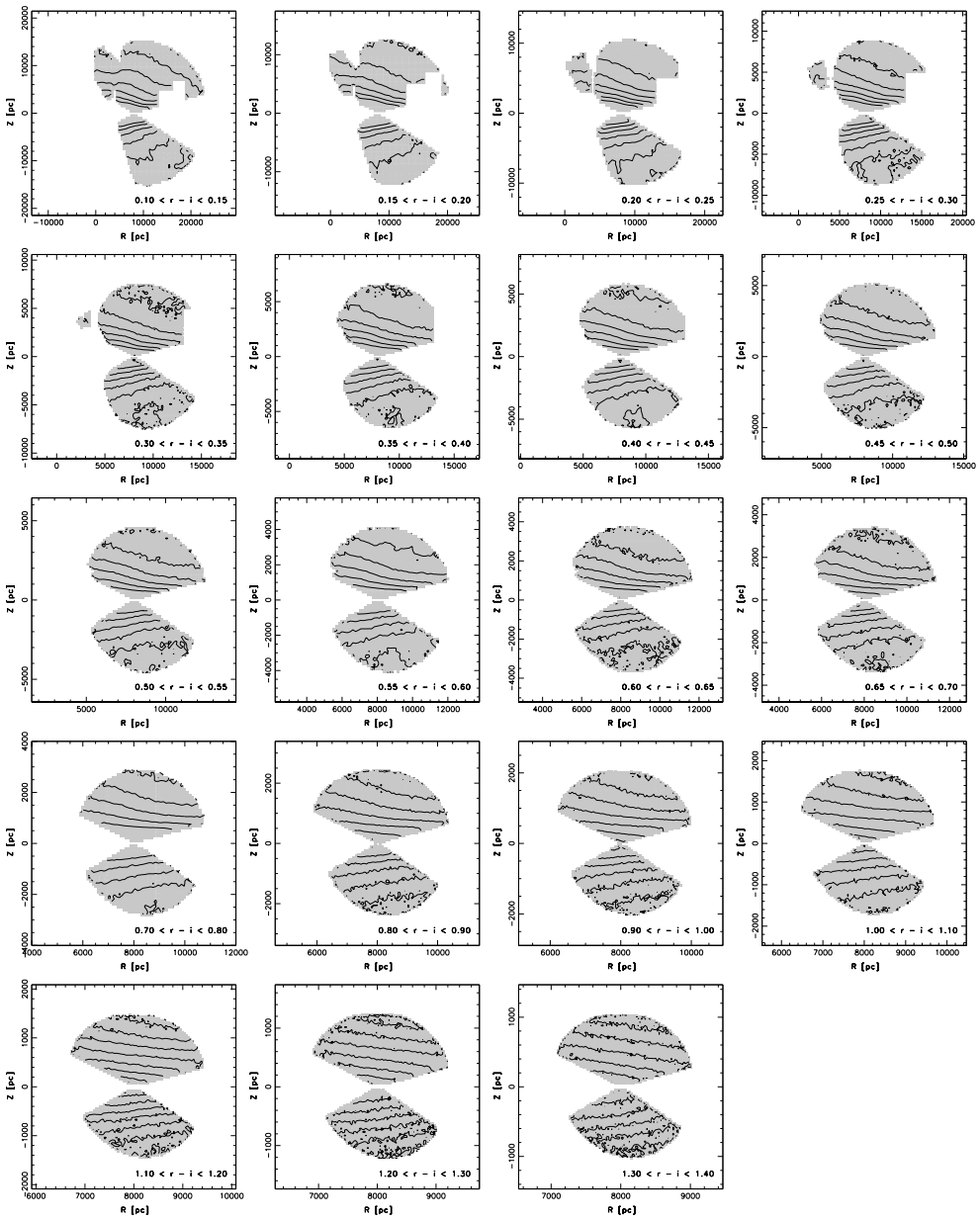

FIG. 19.— "Cleaned up" (R, Z) maps of the Galaxy, analogous to figure 6, but with pixels in obvious overdensities (fig. 18) excluded from azimuthal averaging. We show the maps for all 19 color bins, with the bluest bin in the top left corner and the reddest bin in the bottom right. The contours are the lines of constant density, spaced at constant logarithmic intervals.

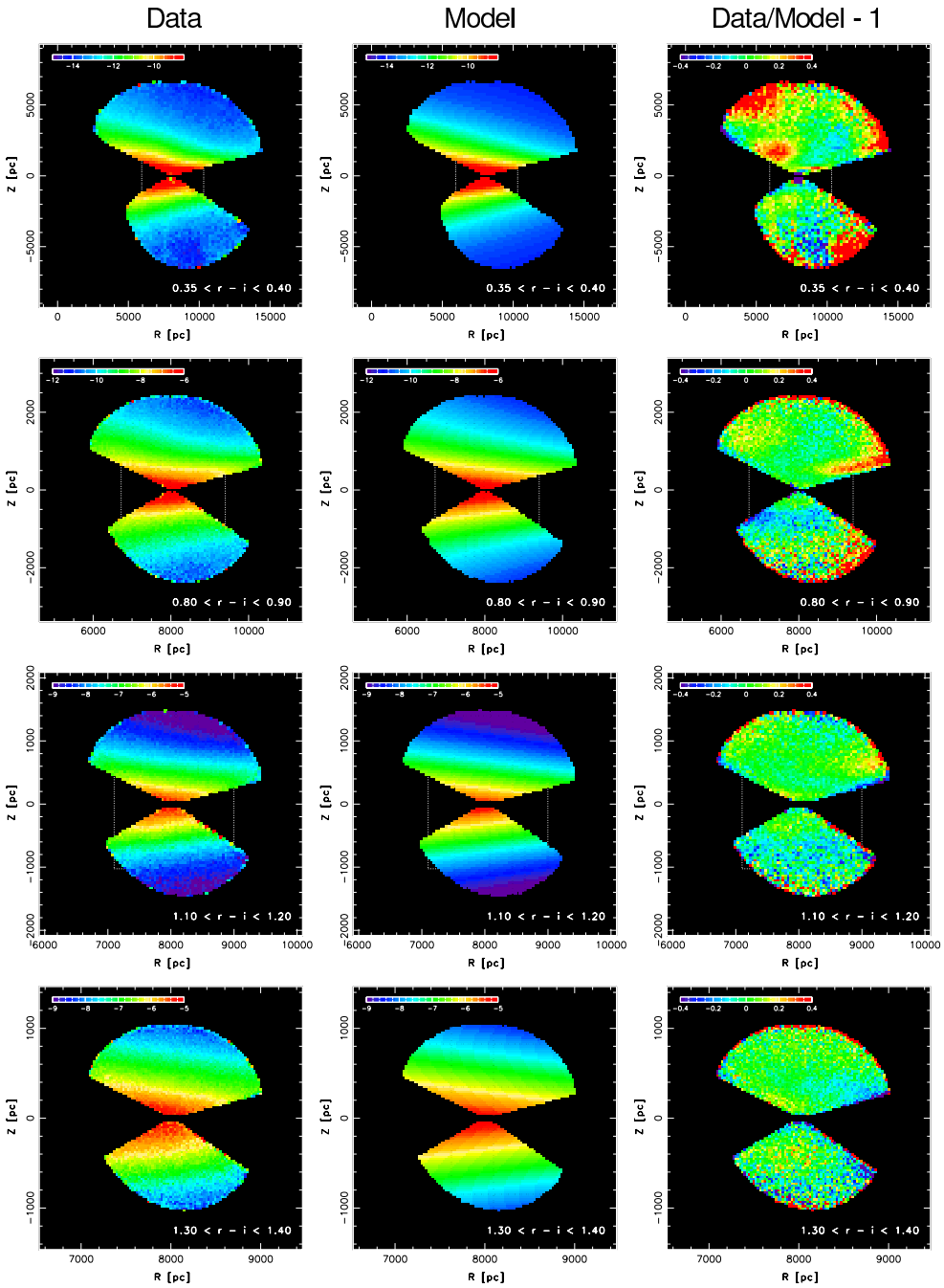

FIG. 20.— Examples of model fits for four color bins, one per each row. Note the different scales. The left panel of each row shows the data, the middle panel the best-fit model and the right panel shows (data-model) residuals, normalized to the model. The residuals are shown on a linear stretch, from -40% to +40%. Note the excellent agreement of the data and the model for reddest color bins (bottom row), and an increasing number of overdensities as we move towards bluer bins. In the residuals map for the $0.35 < r - i < 0.40$ bin (top row) the edges of the Virgo overdensity (top right) and the Monoceros stream (left), the overdensity at $(R \sim 6.5, Z \sim 1.5)$ kpc and a small overdensity at $(R \sim 9.5, Z \sim 0.8)$ kpc (a few red pixels) are easily discernible. The apparently large red overdensity in the south at $(R \sim 12, Z \sim -5)$ kpc is an instrumental effect and not a real feature.

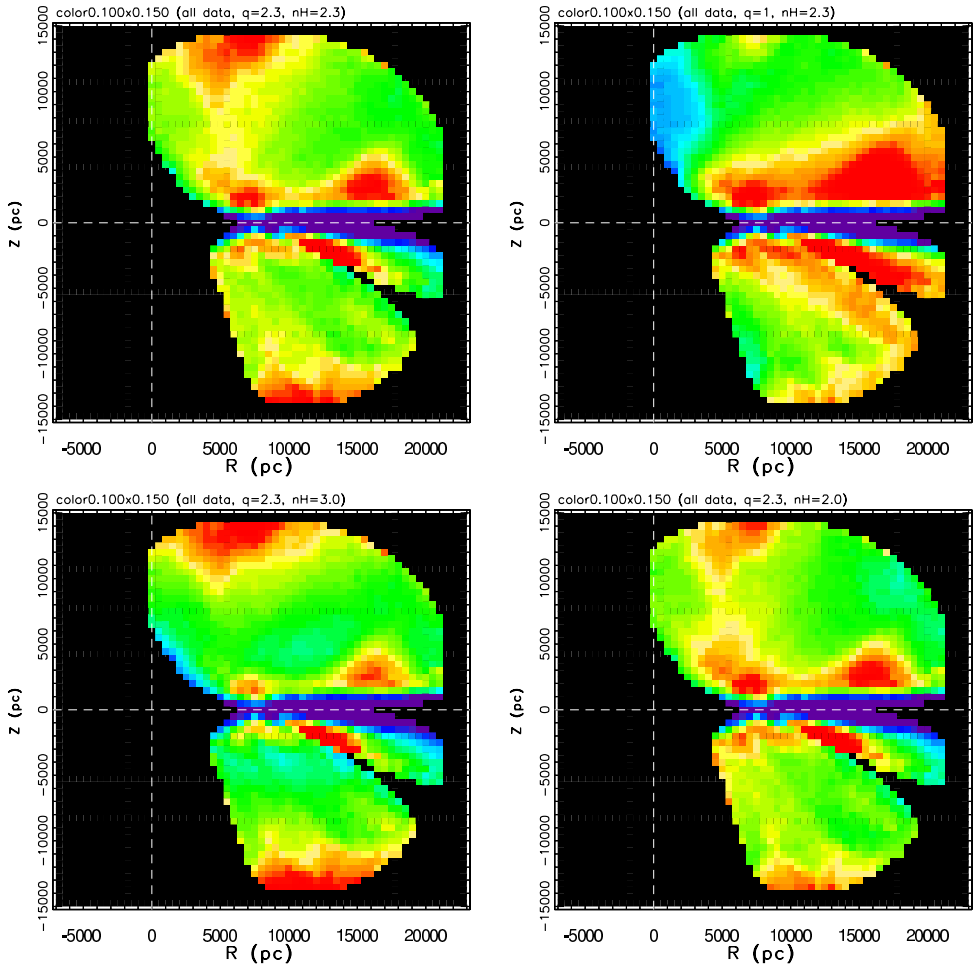

FIG. 21.— Similar to Fig. 20, except that only the (data-model) residuals for color bin $0.10 < r - i < 0.15$, and for four different models, are shown (logarithmic stretch, for $\pm$ a factor of 3, from blue to red, the zero level corresponds to green color). All four models have identical thin and thick disk parameters, and only the halo parameters are varied. The top left panel shows residuals for a best-fit model with $\alpha = 2.3$ and $q_H = 0.45$ (oblate halo). The top right panel shows residuals for a best-fit spherical halo model ($q_H = 1$, with $\alpha = 2.3$), the bottom left panel for $\alpha = 3.0$ and the bottom right for $\alpha = 2.0$ (the latter two for $q_H = 0.45$). Note that, while α is not strongly constrained, the data strongly favor an oblate halo.

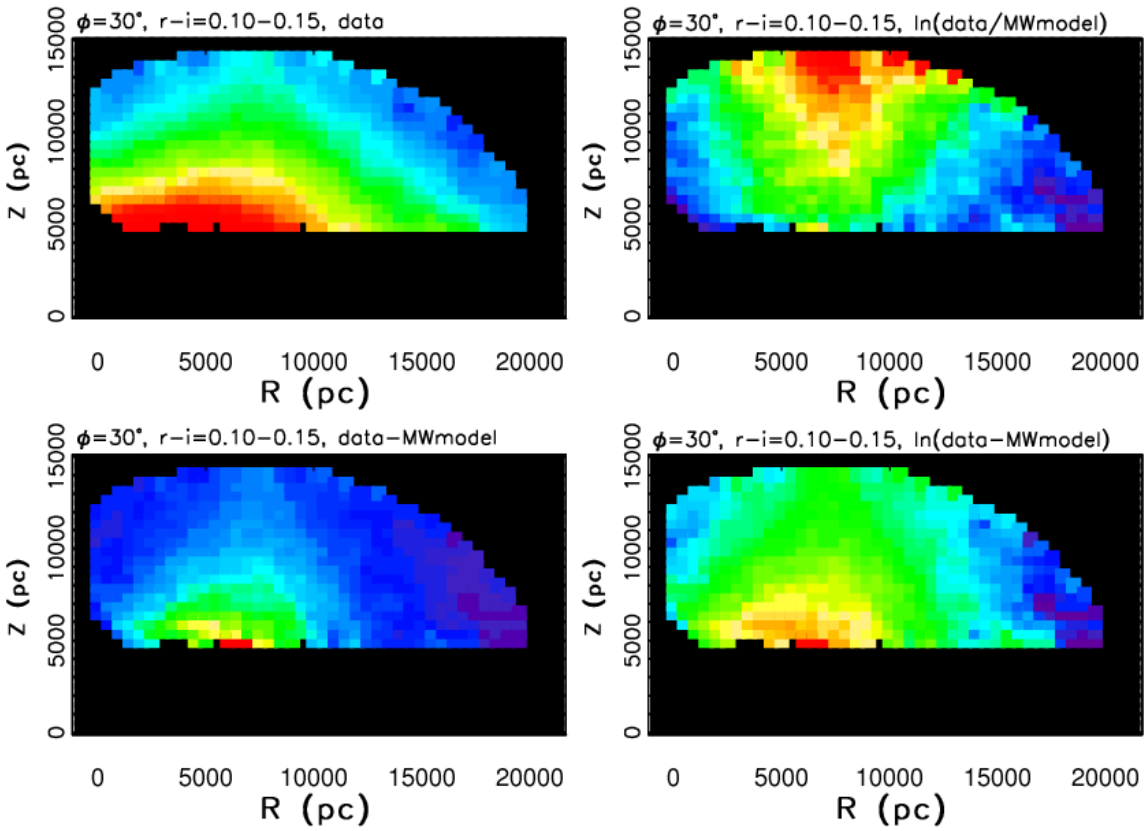

FIG. 22.— The top left panel is similar to the top left panel in Fig. 6, except that here only the data from a narrow plane defined by $\phi \sim 30^\circ$ are shown (see Fig. 8). The top right panel shows *the ratio* of the observed map and a best-fit model constrained using the data from the $y < 0$ region. The bottom left panel show *the difference* between the observed map and the same best-fit model. The bottom right panel displays the map from the bottom left panel on a logarithmic scale.

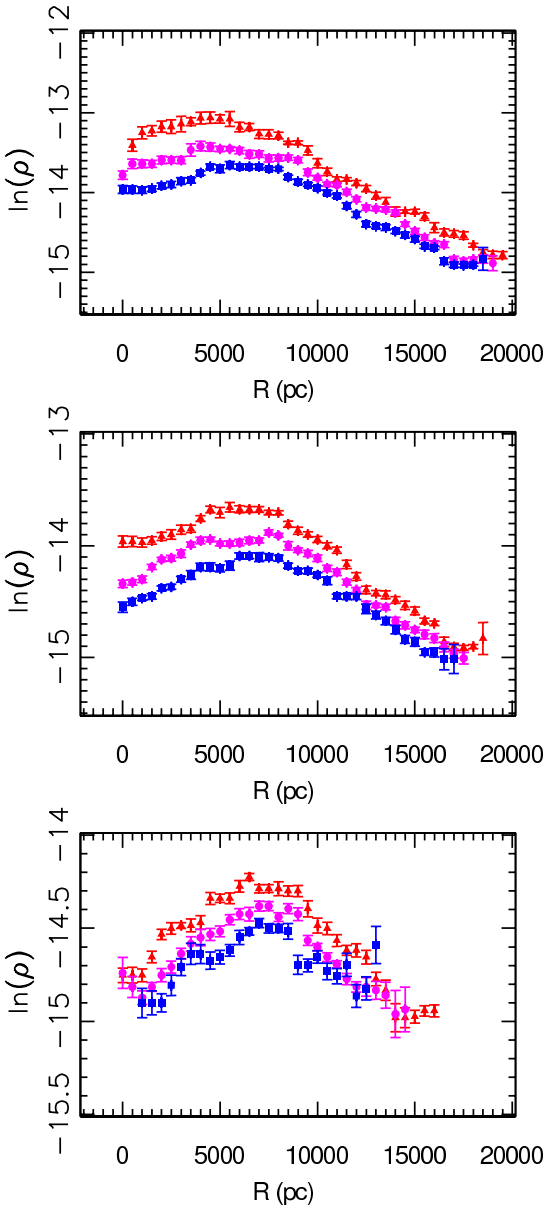

FIG. 23.— The radial distribution of SDSS stellar counts for $0.10 < r - i < 0.15$ color bin, in a narrow plane defined by $\phi = 30°$, and for different heights above the plane, from top to bottom: (6,7,8), (8,9,10) and (11,12,13) kpc.

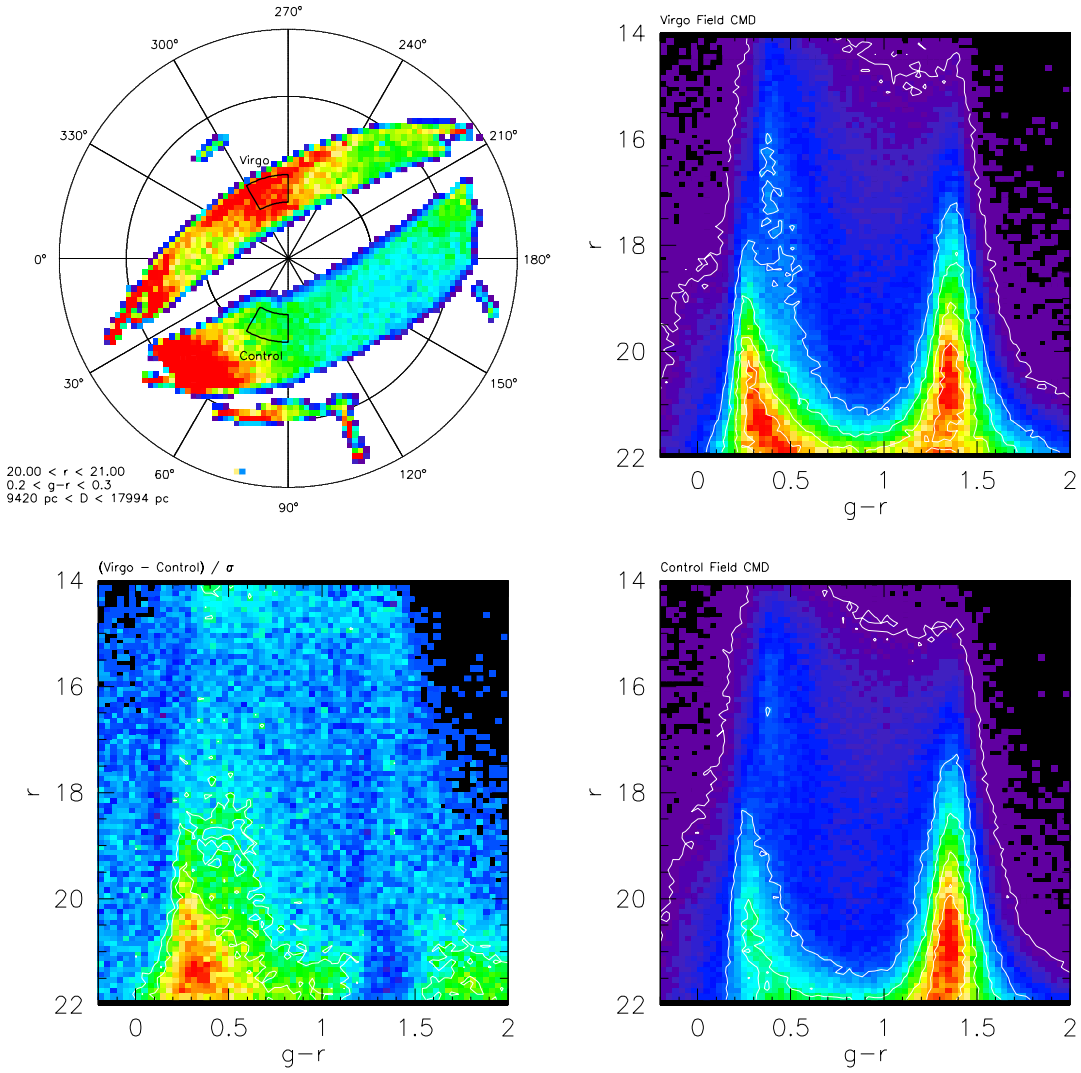

FIG. 24.— The top left panel shows the sky density of stars with $b > 0°$, $0.2 < g - r < 0.3$ and $20 < r < 21$ in the Lambert projection (concentric circles correspond to constant galactic latitude; equal area corresponds to equal solid angle on the sky) of galactic coordinates (the north Galactic pole is in the center, l=0 is towards left, and the outermost circle is $b = 0°$). The number density is encoded with a rainbow color map and increases from blue to red. Note that the sky density distribution is *not* symmetric with respect to the horizontal $l = 0, 180$ line. When the stellar color range is sufficiently red (e.g. $0.9 < g - r < 1.0$), this asymmetry disappears (not shown). The two right panels show the Hess diagrams for two 540 deg^2 large regions towards ($l = 300°, b = 60°, top$) and ($l = 60°, b = 60°, bottom$) (marked as polygons in the top left panel). The bottom left panel shows the difference of these Hess diagrams, normalized by the expected Poisson fluctuations – note the strong statistically significant overdensity at $g - r \sim 0.3$ and $r \gtrsim 20$.

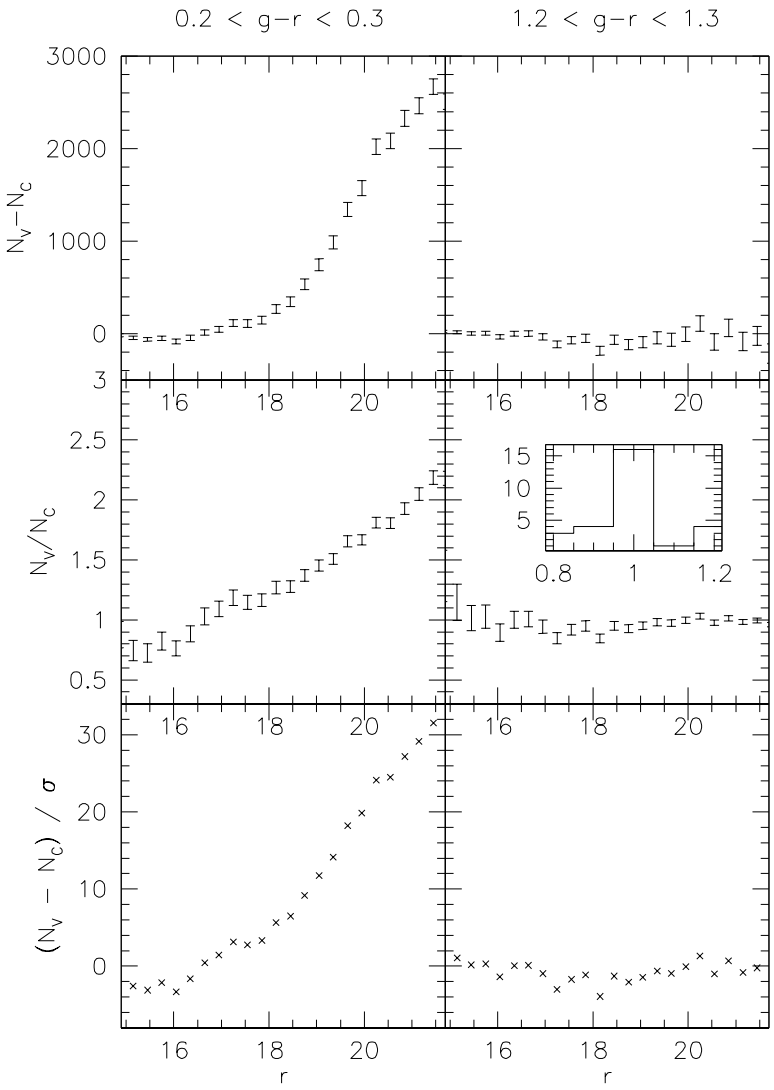

FIG. 25.— Quantitative analysis of the Hess diagram difference shown in the bottom left panel in Fig. 24. The left column corresponds to the color bin $0.2 < g - r < 0.3$ that is representative of the Virgo overdensity, and the right column is a control sample with stars satisfying $1.2 < g - r < 1.3$. The top panels show the counts difference as a function of apparent magnitude, and the middle panels shows the counts ratio. The inset in the middle right panel shows a histogram of the counts ratio for $r < 21.5$. The bottom panels show the counts difference normalized by the expected Poisson fluctuations. Note that for red stars the counts are indistinguishable, while for blue stars the difference is highly statistically significant.

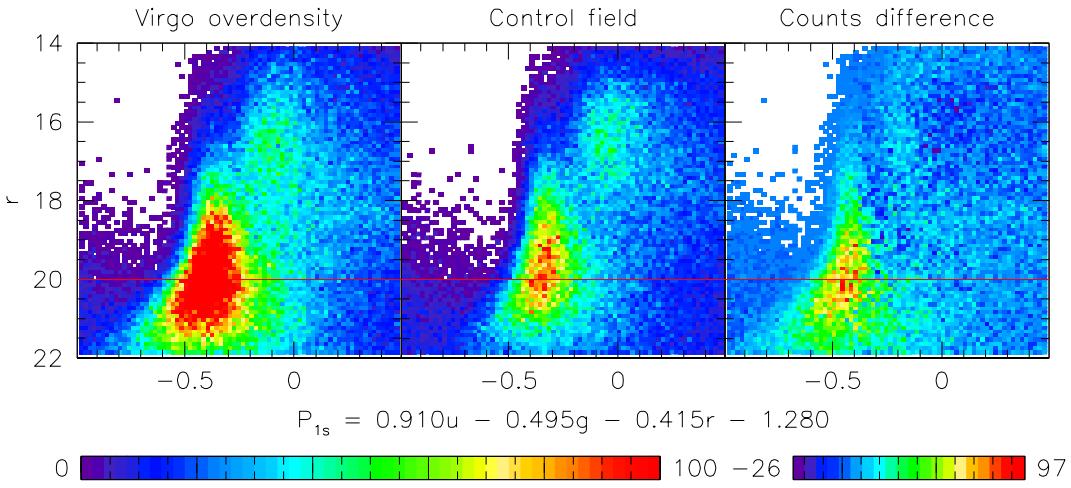

FIG. 26.— Hess diagrams of P_{1s} color vs. r magnitude for the Virgo overdensity field (left), the control field as defined on figure 24 (middle), and their difference (right). The colors encode star counts within the fields. There exists a significant excess of stars with $P_{1s} < -0.2$ in the Virgo overdensity field. There is no statistically significant difference in star counts for stars having $P_{1s} > -0.2$, implying that the stars which constitute of the Virgo overdensity have metallicities lower than disk stars, more consistent with halo stars.

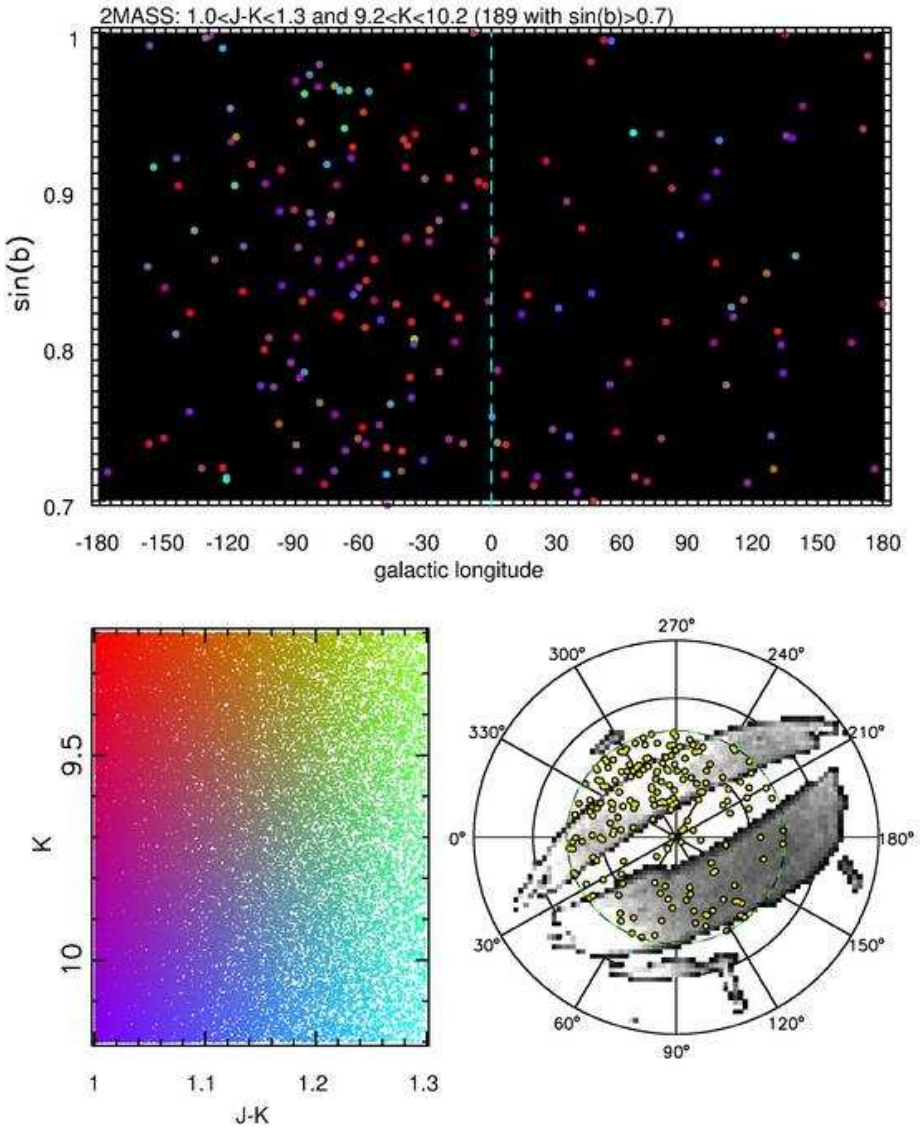

FIG. 27.— The sky distribution of 189 2MASS M giant candidates with $b > 45°$, selected by $9.2 < K < 10.2$ and $1.0 < J - K < 1.3$. The symbols in the top panel are color-coded using their K band magnitude and $J - K$ color, according to the scheme shown in the bottom panel (which shows all 75,735 candidates from the whole sky). At $sin(b) > 0.8$, there are 2.5 times as many stars with $l < 0$ than with $l > 0$. This asymmetry provides an independent confirmation of the Virgo overdensity revealed by the SDSS data.

APPENDIX

EFFECTS OF LOCUS PROJECTION

The improvement in the estimate of $r-i$ color resulting from the locus projection depends on the local slope of the locus. If the locus has a steep or almost vertical slope, as for stars with $g-r \sim 1.4$ (cf. figure 5), the knowledge of $g-r$ color does not further constrain $r-i$ color. On the other hand, for shallow slopes the knowledge of $g-r$ color determines the intrinsic $r-i$ to a much better accuracy than the the $r-i$ measurement alone. For most of the observed $g-r$ color range we are closer to the second regime, with the locus having a slope of $d(r-i)/d(g-r) \sim 0.3$ for $0 < g-r < 1$.

To illustrate the effects of locus projection, in Fig. A28 we simulate an ensemble of 10^5 stars with the same color ($g-r = 0.4, r-i = 0.143$) subjected to photometric errors representative of SDSS observations ($\sigma_{r-i} = \sigma_{g-r} = 0.03$ mag). Errors introduce a scatter in observed colors as shown in the inset. Using only the $r-i$ information we obtain the expected $\sigma_{r-i} = 0.03$ mag scatter in observed $r-i$ color (dashed histogram). By projecting the colors to the locus, the scatter is reduced to $\sigma_{r-i} = 0.01$ mag. As we construct density maps for stars binned in color bins with $\Delta(r-i) = 0.05$ mag width, this is a significant reduction in scatter.

There are other benefits of locus projection. Figure A30 illustrates how photometric errors can bias the determination of the number of stars in regions with large gradients of the number density (in the $g-r$ vs. $r-i$ color-color diagram). The solid line shows the true density distribution of stars as a function of $r-i$ color. In this toy model, we used $\rho(r-i) \propto (r-i)^2$, with a sharp cutoff at $r-i = 0.24$ (solid histogram). Scattering the stars drawn from that distribution with the $\sigma_{r-i} = \sigma_{g-r} = 0.03$ mag photometric errors, and binning in $r-i$ color bins, produces the dashed histogram (effectively, a convolution of the original distribution with the SDSS photometric errors). It systematically underestimates the original density distribution by as much as 50% in the region of highest negative gradient (near the $r-i = 0.24$ cutoff), while overestimating the density in regions with positive density gradient. The exact under or overestimation depends on the scale at which the true density changes appreciably. If it is significantly smaller than σ_{r-i} or σ_{g-r}, as is the case near the cutoff in figure A30, the biases become significant. Applying the locus projection gives a much better estimate of the original distribution (dotted histogram).

This is not a purely hypothetical example – this type of strong density gradient is observed near $g-r \sim 0.2$ (cf. figure 5). Figure A30 compares the number of stars per $r-i$ color bin for observed $r-i$ colors (dashed histogram) and the colors estimated by locus projection (solid histogram) for the 48 million stars in our star catalog. In the regions of maximal gradients the locus projection has a $\sim 20\%$ effect on the total number of stars per $r-i$ bin. Not including this correction would similarly bias the density normalization of Galactic models deduced from this sample. The bias would further propagate to luminosity function determination.

One may further be concerned about the dependence of the location of the $r-i$ vs. $g-r$ stellar locus on other parameters. We do observe a slight magnitude dependence of the locus, especially for stars with bluer $g-r$ colors. Figure A31 shows the dependence of the measured $r-i$ color on the r band magnitude for stars with $0.29 < g-r < 0.31$ (the "worst case $g-r$ color", where we find the dependence of the locus location on the magnitude to be the largest). We find a weak, approximately linear dependence, with $d(r-i)_{locus}/dr \sim 0.007$ mag/mag (solid line). The horizontal dashed line shows the location of the locus for this bin as given by eq. 3. The two match for $r = 19$. We have chosen to disregard this magnitude dependence when performing the locus projection procedure. We reason that the real dependence is not on magnitude but on metallicity and probably other unknown factors for which we do not have a firm handle. By attempting to correct for those, we risk introducing additional unknown and more complicated biases. Secondly, the magnitude dependence is relatively small and only affects the bluest bins.

Finally, the three panels in Fig. A32 show the histograms of observed $r-i$ colors for stars which have their locus projected colors in the $0.1^{\rm mag} < (r-i)_e < 0.15^{\rm mag}$ color range. The top panel shows the histogram for all stars in the sample. The 0.03 mag scatter is comparable to SDSS photometric errors. To check for the effects discussed in the previous paragraph, the center and bottom panels show histograms for the brightest and faintest magnitude bin respectively. Slight magnitude dependence can be seen as a small shift of histogram median to the left (center panel) and right (top panel). Also, the worsening of photometric precision at the faint end is quite visible in the bottom panel, as the scatter increases to 0.08 mag.

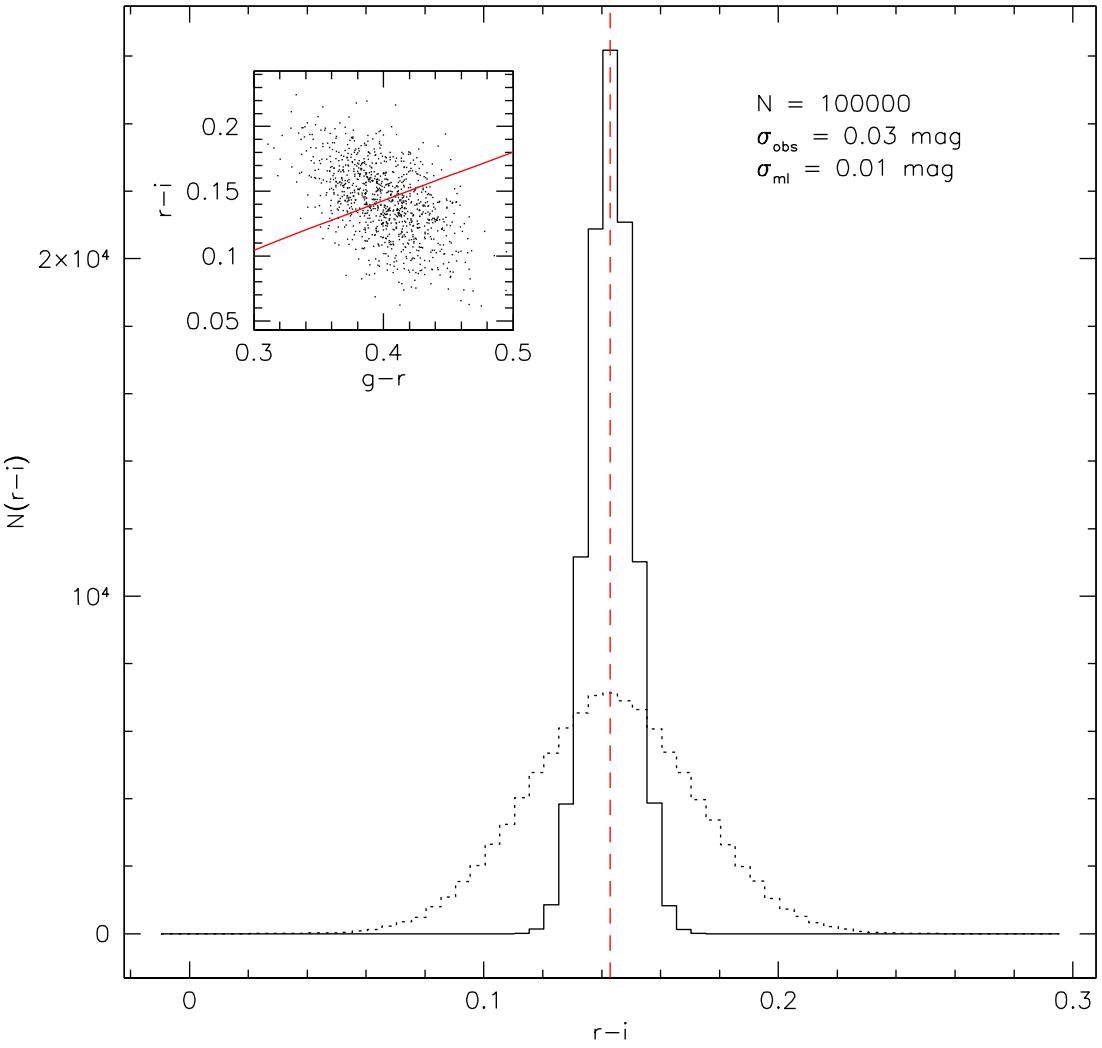

FIG. A28.— An illustration of the reduction in the $r-i$ color scatter after applying the locus projection. An ensemble of 10^5 stars with the same color ($g-r=0.4, r-i=0.143$) is subjected to SDSS photometric errors ($\sigma_g=\sigma_r=\sigma_i=0.02$ mag), resulting in the color distribution shown in the inset. Its $r-i$ histogram (dashed line) has a root-mean-square scatter of $\sigma_{r-i}=0.03$ mag. After the colors are locus corrected (solid histogram), the scatter is reduced to $\sigma_{r-i}=0.01$ mag. The amount of reduction of the scatter depends on the slope of the locus – the more horizontal the locus gets, the better is the determination of the true $r-i$ color.

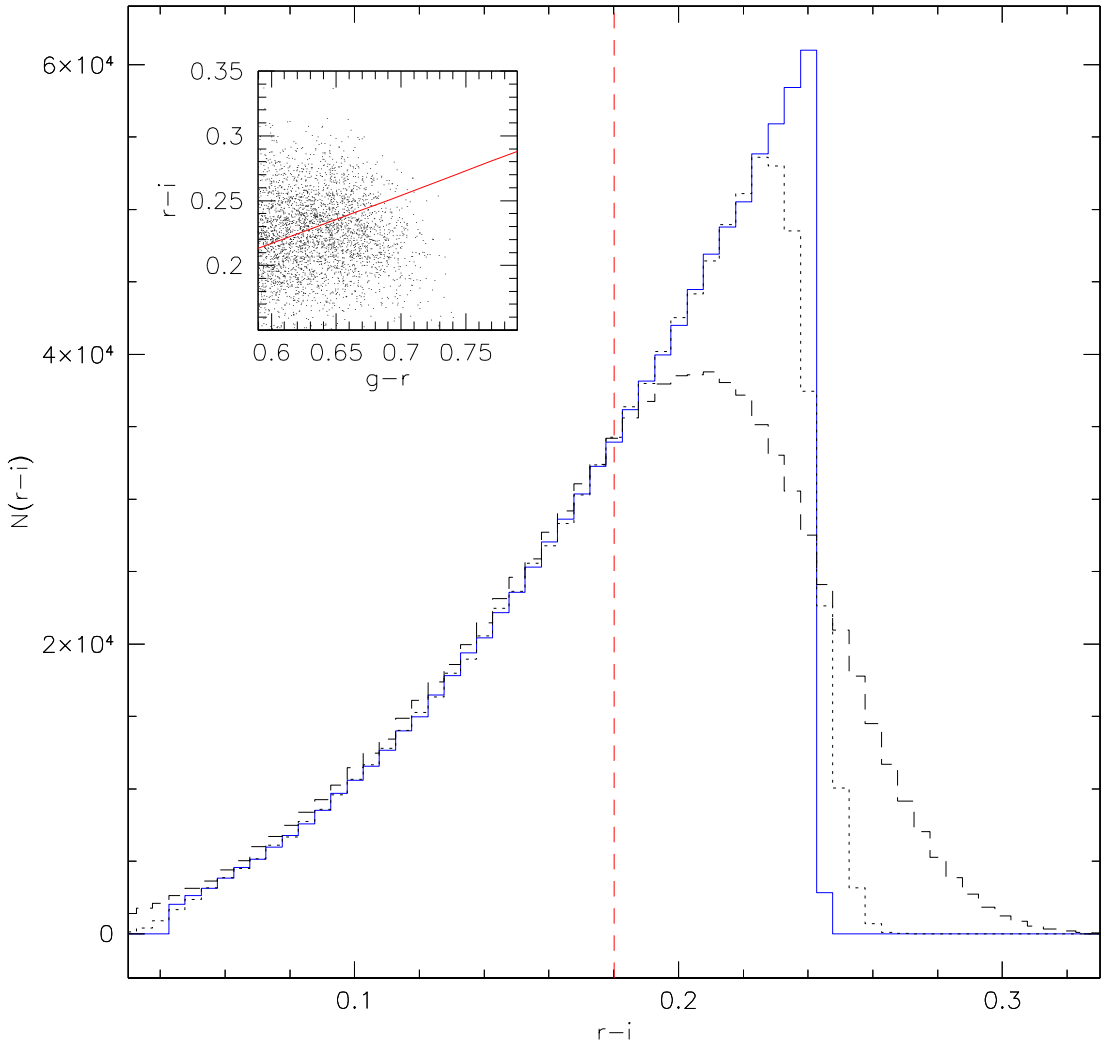

FIG. A29.— An illustration of the bias in the determination of the number density introduced by photometric errors. The solid histogram shows a toy model distribution as a function of the $r-i$ color ($\rho(r-i) \propto (r-i)^2$, with a sharp cutoff at $r-i=0.24$). The dashed histogram is the convolution of the original distribution with SDSS photometric errors ($\sigma_g = \sigma_r = \sigma_i = 0.02$ mag). The measured density of stars with $r-i=0.24$ is underestimated by as much as 50%. Applying the locus projection gives an improved estimate of the original distribution (dotted histogram).

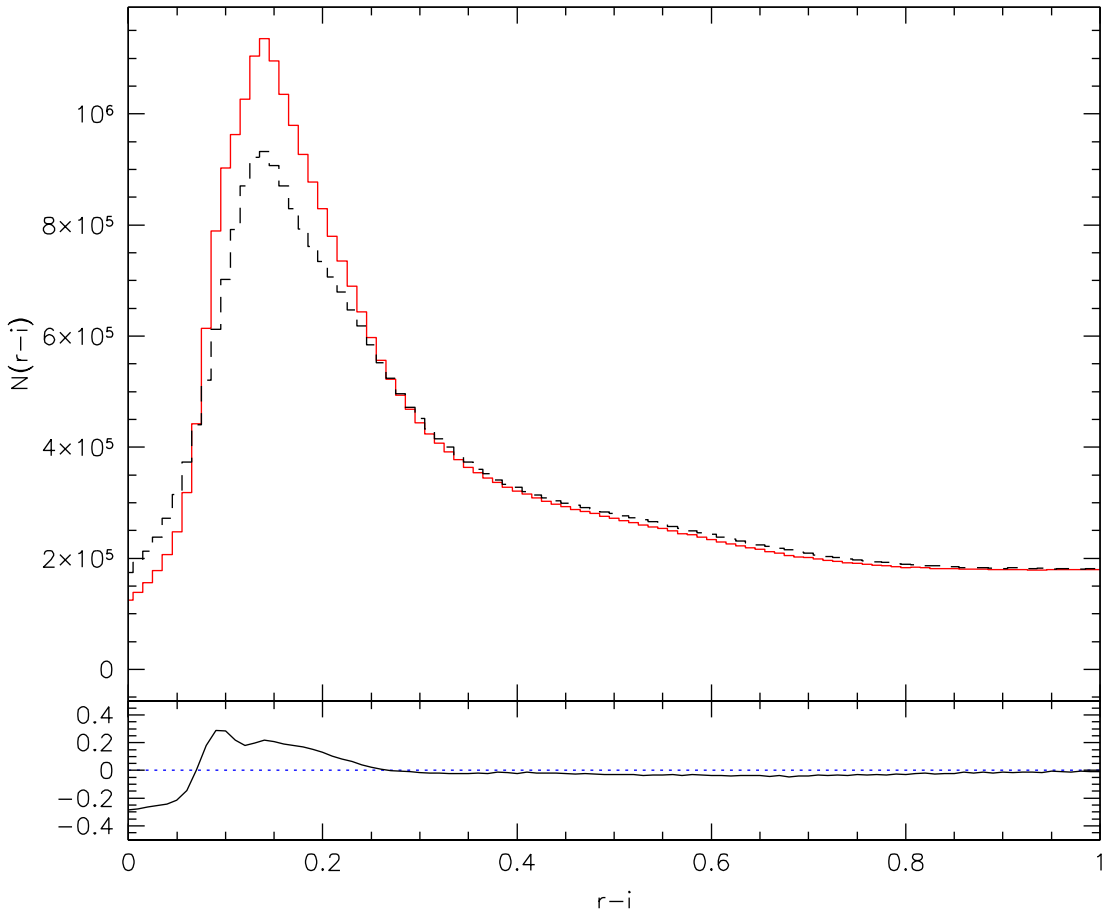

FIG. A30.— A comparison of the number of stars per $r-i$ bin for observed $r-i$ (dashed histogram) and the locus corrected $(r-i)_e$ colors (solid histogram) for the 48 million stars in our star catalog. In the regions of maximal gradients the locus projection has a $\sim 20\%$ effect on the total number of stars per $r-i$ bin. Not including this correction would similarly bias the density normalization of Galactic models.

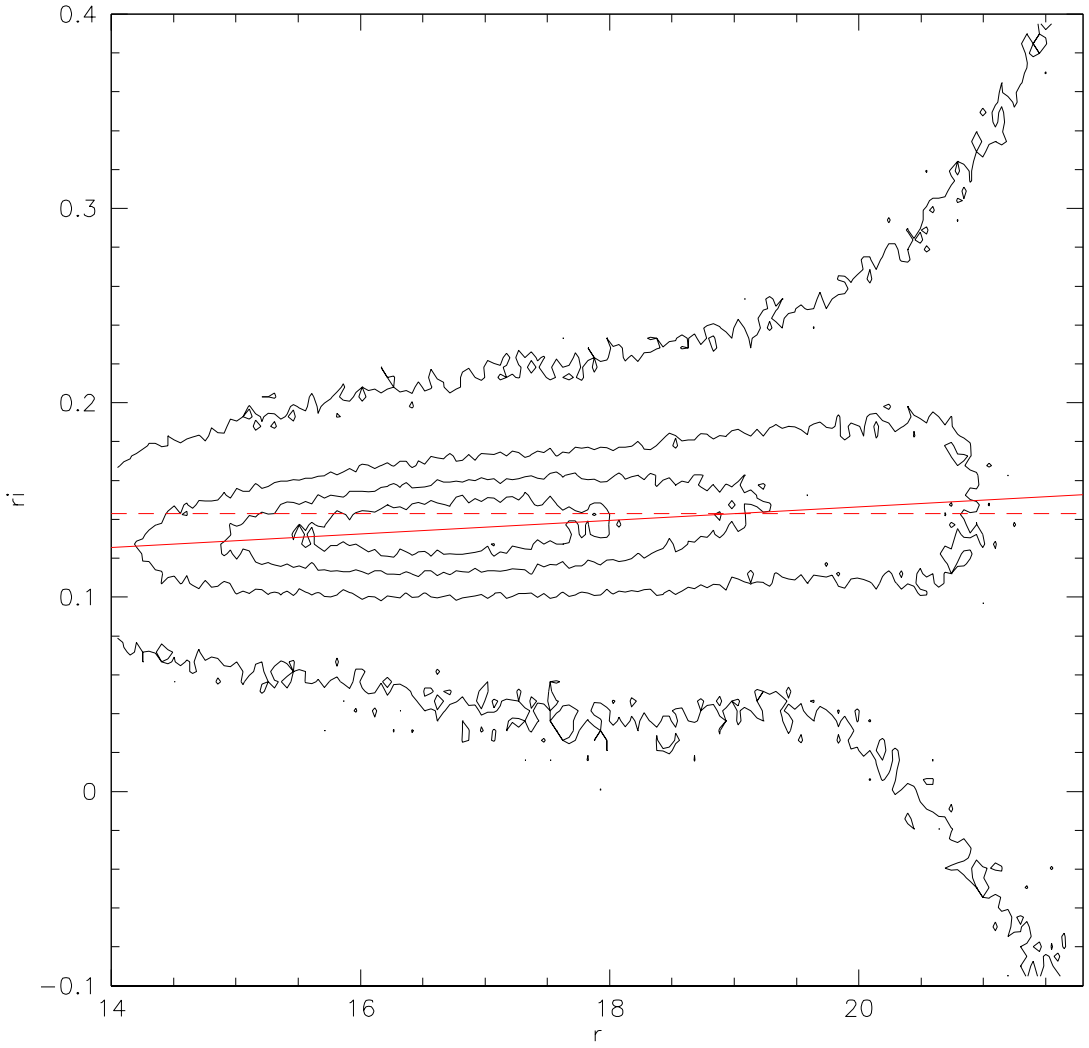

FIG. A31.— The dependence of the measured $r-i$ color on the r band magnitude for stars with $0.29 < g-r < 0.31$. An approximately linear dependence, with $d(r-i)/dr$ ∼0.007 mag/mag is observed (solid line). The horizontal dashed line shows the location of the locus for this bin as given by eq. 3. The two match for $r = 19$.

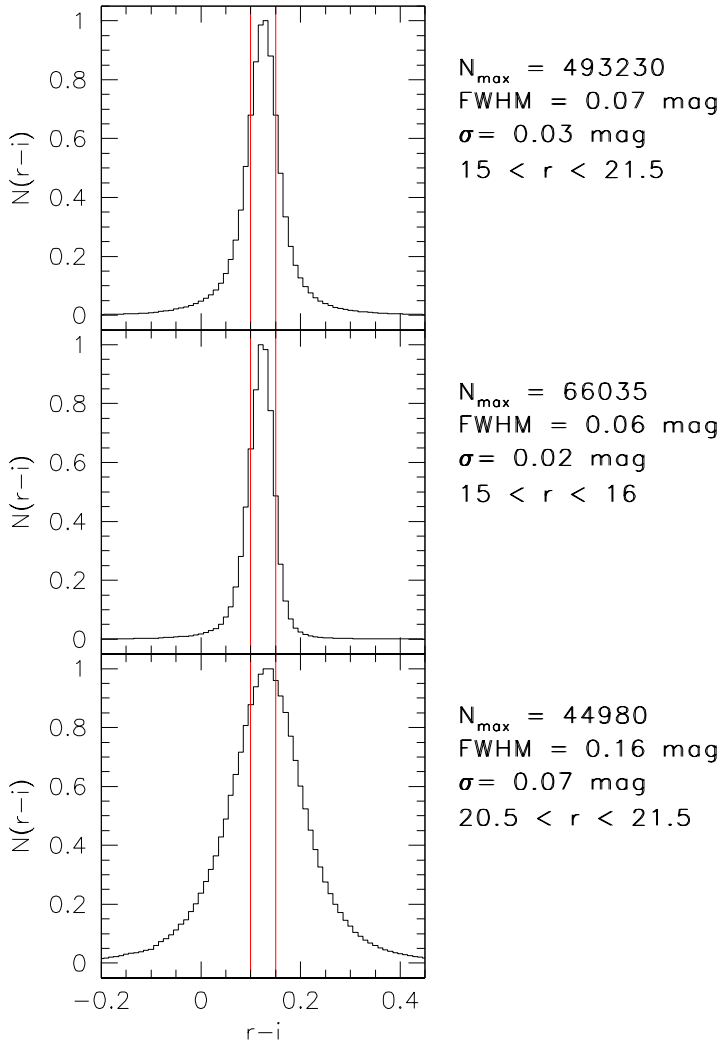

FIG. A32.— The effect of ignoring the magnitude dependence of the locus. The histograms show observed $r-i$ colors of stars having locus-corrected colors in the $0.1 < (r-i)_e < 0.15$ color range. The top panel shows the histogram for all stars in the sample. The spread of $\sigma = 0.03^{\rm mag}$ is comparable to SDSS photometric errors. The middle and bottom panels show histograms for the brightest and faintest magnitude bin, respectively. A weak magnitude dependence can be seen as a small shift of histogram median to the left (middle panel) and right (bottom panel).